Alma Mater Studiorum · University of Bologna

School of Science
Department of Physics and Astronomy
Master Degree in Physics

Microstructural changes in Alzheimer's Disease: a comparison study of models in diffusion MRI

Supervisor:
Prof. Claudia Testa

Co-supervisor:
Dr. Mattia Ricchi

Submitted by:
Irene Persoglia

Academic Year 2023/2024

Contents

Abstract

Diffusion Weighted Imaging (DWI) is an MRI technique that quantifies the random movement of water molecules within tissues, offering valuable information about tissue architecture and helping to identify various pathologies, particularly in the brain and other soft tissues. A new model called Neurite Orientation Dispersion and Density Imaging (NODDI) has been proposed for characterizing brain tissue at a microscopic level, since it is a two-level multi-compartment model in which all compartments are considered non-exchanging, distinguishing between the tissue and non-tissue components within the brain. This thesis compares two versions of it, the NODDI-Bingham and NODDI-Watson diffusion MRI models in assessing brain microstructure across Alzheimer's Disease, Mild Cognitive Impairment, and cognitively normal individuals [Alzheimer's Disease Neuroimaging Initiative (ADNI),]. Microstructural metrics (ODI, partial volumes, beta fraction) were extracted and mapped to several brain regions of white and grey matter, followed by statistical analysis, including three-way ANOVA, Tukey's HSD test, and Pearson correlation with clinical cognitive scores. Key findings indicate that both models detect significant microstructural changes linked to cognitive decline, with NODDI-Bingham showing slightly higher sensitivity. Strong correlations in regions like the cortex and hippocampus underscore their role in Alzheimer's progression. While promising as early biomarkers, NODDI metrics might be more effective when combined with other diagnostic tools (e.g. PET, genetic testing) to improve predictive accuracy. This work highlights the potential of advanced diffusion MRI models in understanding brain changes associated with Alzheimer's and their possible role in early disease diagnosis.

Chapter 1

Introduction

Alzheimer's Disease represents one of the major challenges in the neurological field, characterized by a progressive neuronal loss and by the disruption of synaptic connections, resulting in a cognitive decline [Prince et al., 2015, Association, 2020]. Although significant progress has been made in understanding the pathological mechanisms of Alzheimer's, early identification and effective therapeutic intervention remain crucial objectives, which have not yet been fully achieved [Aisen et al., 2017]. In this context, advanced imaging techniques such as diffusion magnetic resonance imaging (dMRI) have the potential to reveal microstructural changes in the brain before clinical symptoms become apparent.

Diffusion imaging exploits the movement of water molecules to infer details about the brain tissue microstructure [Mori and Zhang, 2006, Basser et al., 1994]. Traditionally, the diffusion tensor model (DTI) has been the main tool for studying brain connectivity. However, the DTI has significant limitations, as it assumes a Gaussian diffusion of water, not always accurately reflecting the complexity of neural microstructure [Jones et al., 2013, Alexander and Barker, 2005]. To overcome these limitations, multi-compartment models have been developed, offering a more detailed description of the brain microstructural properties.

Among these, the Neurite Orientation Dispersion and Density Imaging (NODDI) model stands out for its ability to separate the contributions of the density and dispersion of neurites [Zhang et al., 2012]. The NODDI-Watson model, based on the Watson distribution, is widely used to describe the unimodal distribution of neurites. This model, however, presents a huge limitation in that the unimodal distribution is overly simplistic for capturing the complex microstructure of the brain, particularly in regions with crossing fibers or multiple orientations, which can lead in inaccuracies in estimating the model metrics. To overcome these limitations, the NODDI-Bingham model has been introduced, using the Bingham distribution to represent more complex and multimodal orientations of neurites, giving a more detailed and comprehensive view of the cerebral microstructure [Tariq et al., 2016].

This thesis work aims to apply the NODDI-Watson and the NODDI-Bingham models to analyze microstructural changes in the brain of patients with Alzheimer's Disease and a Mild Cognitive Impairment, obtained from the Alzheimer's Disease Neuroimaging Initiative (ADNI) database [Colgan et al., 2016, Wang et al., 2011, Cox et al., 2016]. Through the use of advanced dMRI data, this study aims to:

- characterize the distribution and density of neurites in brain regions affected by Alzheimer's Disease;
- compare the precision and the effectiveness of NODDI-Watson and NODDI-Bingham models in detecting disease specific microstructural changes [Novikov et al., 2018, Jespersen and Kroenke, 2020];
- explore correlation between microstructural parameters derived from NODDI models and clinical biomarkers for Alzheimer's, such as the MMSE and MoCa cognitive scores.

The ultimate objective is to improve understanding of microstructural changes associated with Alzheimers' and to assess the potential of multi-compartment models as diagnostic tools and prognostic in clinical practice. This research could contribute to the development of more sensitive and specific imaging methodologies, facilitating timely and targeted therapeutic interventions for patients suffering from this devastating disease.

Chapter 2

Theory

2.1 Diffusion MRI

2.1.1 Molecular diffusion

Molecular diffusion refers to the random translational motion of molecules, also known as Brownian motion.
The first mathematical description of diffusion dates back to Fick, in 1855. He devised a system of differential equations that quantitatively described diffusion of molecules through ultra-thin membranes [Fick, 1855]. Fick's first law of diffusion describes the behavior of a flux of particles, **J** (i.e. the number of particles that moves through a 2D plane per unit of time), at spatial position **r** and time t as a function of two parameters:

$$\mathbf{J}(\mathbf{r}, t) = -D\nabla c(\mathbf{r}, t) \tag{2.1}$$

From this equation arises the proportionality between the flux and the concentration gradient ∇c, where c(**r**, **t**) is the concentration of particles, and the proportionality coefficient is called *diffusion coefficient*, D, which has dependencies only on the mass of the molecules (their size) and the temperature and nature of the medium (*viscosity*). Conservation of mass is expressed by the continuity equation:

$$\frac{\partial c(\mathbf{r}, t)}{\partial t} = -\nabla \mathbf{J}(\mathbf{r}, t) \tag{2.2}$$

The combination between Equations 2.1 and 2.2 leads to Fick's second law of diffusion:

$$\frac{\partial c(\mathbf{r}, t)}{\partial t} = D\nabla^2 c(\mathbf{r}, t) \tag{2.3}$$

where D is assumed independent from the concentration.
This formulation of the diffusion process assumes a net flux by diffusion over a concentration gradient. In the absence of internal concentration gradients, like diffusion in a

free medium, it is helpful to consider a more probabilistic (or statistical) description, considering the movement of the particles over time. In the case of isotropic diffusion, the probability of a molecule moving from position $\mathbf{r}_0$ to position $\mathbf{r}$ over time is described by a probability distribution $P(\mathbf{r}_0|\mathbf{r}, t)$ which also obeys the second law of diffusion:

$$\frac{\partial P(\mathbf{r}_0|\mathbf{r}, t)}{\partial t} = D\nabla^2 P(\mathbf{r}_0|\mathbf{r}, t) \tag{2.4}$$

Additional conditions can be applied to this formula: a starting condition $P(\mathbf{r}_0|\mathbf{r}, t) = \delta(\mathbf{r}_0 - \mathbf{r})$ and a boundary condition $P(\mathbf{r}_0|\mathbf{r}, t) \to 0$ for $\mathrm{r} \to \infty$. In this way it is possible to solve the previous equation for unbounded, isotropic diffusion:

$$P(\mathbf{r}_0|\mathbf{r}, t) = (4\pi Dt)^{-3/2} \exp[-(\mathbf{r} - \mathbf{r}_0)^2/4Dt] \tag{2.5}$$

Hence, given a free medium and a time interval, the displacements of the molecules follow a Gaussian distribution in every possible direction.
An important contribution to the physical description of this process was given by Einstein [Einstein, 1905], who characterized diffusion as resulting from the thermal energy carried by the molecules in motion. Since the distance traveled by the molecules is random, and the probability of displacement is the same along the three directions, the net displacement $\langle(\mathbf{r} - \mathbf{r}_0)\rangle$ is zero. Therefore, the statistical description of this phenomenon considers the mean-squared distance traveled by the molecules as a function of the diffusion time, T_d, and the diffusion coefficient only:

$$\langle X^2 \rangle = 6DT_d \tag{2.6}$$

where $\langle X^2 \rangle$ is the average-mean squared diffusion distance.

2.1.2 Diffusion-driven MRI

As previously said, diffusion MRI (or dMRI) is currently the only method to provide insight about molecular displacement in vivo in a non-invasive manner. There have been huge improvements over the past fifty years in terms of the way we measure diffusion in living subjects.

The foundation of this approach dates back to the spin-echo technique developed by Erwin Hahn in 1950 [Hahn, 1950]. He discovered that by applying a pair of radiofrequency pulses to a sample in a magnetic field, it was possible to generate an "echo" signal that refocused the spins of hydrogen nuclei (protons) in water molecules (Figure 2.1).
Specifically, he noticed that, by applying an initial 90° RF pulse, the magnetization of the spins is tipped from their alignment with the external magnetic field (longitudinal plane) to the transverse plane. Then, after this pulse, the spins start to dephase due

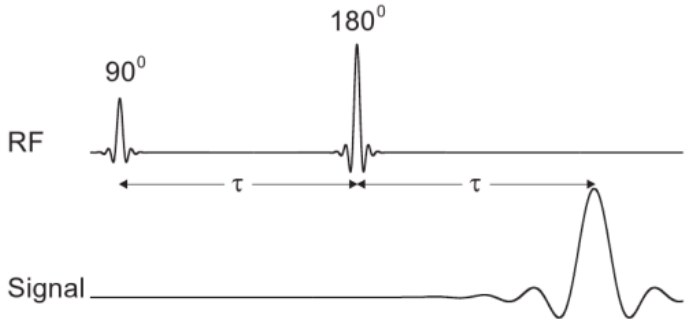

Figure 2.1: A schematic representation of the spin-echo method introduced by Hahn [Johansen-Berg and Behrens, 2013]. Here, the Echo Time is TE = 2·τ.

to inhomogeneities in the magnetic field, leading to a loss of coherence and a decrease in the transverse magnetization. At this point, after a time interval τ, by applying a 180° RF pulse, the spins are flipped again and start rephasing, ultimately leading to the formation of an echo. This echo signal reaches its maximum at time TE (Echo Time, typically equal to twice the time interval τ), where the dephased spins are refocused. This echo provided information about the local environment of the spins, particularly their interactions and motion, as the dephasing of the spins is caused by translational diffusion within an inhomogeneous magnetic field. However, Hahn's original method was limited in its ability to separate different types of molecular motion.

This approach was then modified and further developed by Carr and Purcell, who in 1954 extended Hahn's work by adding additional pulses. They proposed a measurement setting which resumed the spin-echo technique, but assuming that the echo magnitude could be sensitized solely to the effects of random molecular spreading caused by diffusion, to provide a direct measure of the latter [Carr and Purcell, 1954]. Because spin's precession frequency is determined by the local magnetic field ($\omega = \gamma B$), with the application of a magnetic field gradient (Figure 2.2) the spins will precess at different angular frequencies, since at different locations they will experience different magnetic fields. After some time, the spins will acquire different phase shifts depending on their location. Stronger gradients will lead to sharper phase changes across the sample, yielding a higher sensitivity to diffusion.

However, it was not until the development of a pulsed-gradient-spin-echo (PSGE) method by Stejskal and Tanner [Stejskal and Tanner, 1965] that NMR diffusion measurements became a routine technique for the study of self-diffusion coefficients. They replaced the single gradient proposed by Carr and Purcell with short-duration gradient pulses (Figure 2.3). When additional gradient pulses are applied, these gradients make the MRI signal

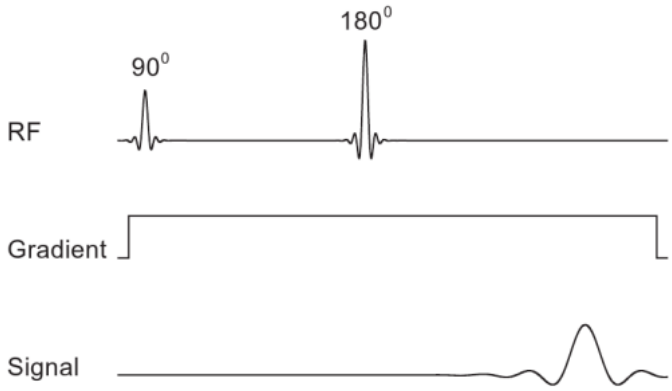

Figure 2.2: A schematic representation of the spin-echo method in the presence of a constant field gradient modified by Carr and Purcell. The decrease in signal intensity is due to diffusion occurring in the resulting inhomogeneous field [Johansen-Berg and Behrens, 2013].

more sensitive to the motion of water molecules. If a molecule diffuses during the time between the gradients, the phase shift induced by the first gradient is not fully reversed by the second gradient, resulting in signal attenuation. The amount of attenuation depends on how much diffusion occurs, which is quantified by the *b-value*. The b-value is calculated based on the gradient pulses used in the MRI sequence and is given by the formula:

$$b = \gamma^2 G^2 \delta^2 \left(\Delta - \frac{\delta}{3} \right) \tag{2.7}$$

where γ is the gyromagnetic ratio (a constant specific to the type of nucleus being imaged), G is the strength of the applied gradient, δ is the duration of each gradient pulses and Δ is the time between the two gradient pulses. The higher the b-value (achieved by stronger or longer gradients), the greater the sensitivity to diffusion, leading to more pronounced signal attenuation in regions with high diffusion.

Diffusion measurements by NMR rely on the principle of signal loss through diffusion dependent phase dispersal. When a positive gradient lobe is applied in one direction, the spins acquire a position-dependent phase $\phi_1 = \gamma r G \delta$ where r is the position of the point sample.
After a time of delay, Δ, a negative gradient of equal duration but opposite amplitude is applied, inducing a position-dependent phase ϕ_2.
In a static condition, where no diffusion is present, $\phi_1 = -\phi_2$, so that at the time of acquisition the dephasing induced by the application of the gradients cancels out. However, in a situation where diffusion is present, when the spins move during the delay Δ, the phase induced by the second field gradient no longer cancels the phase induced

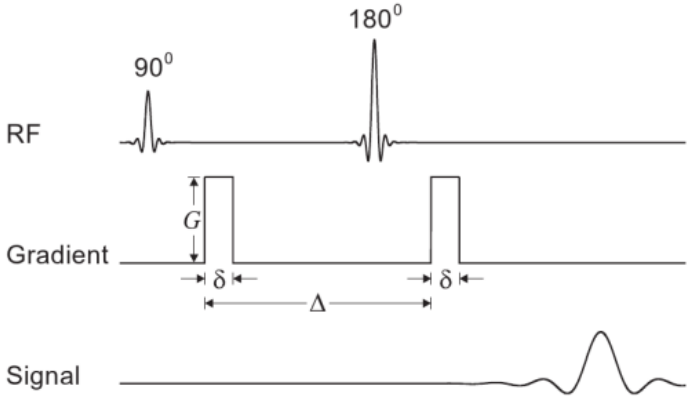

Figure 2.3: A schematic representation of the spin-echo method modified by Stejskal and Tanner. Δ indicates the time between the application of the two gradient pulses [10-100 ms]. δ indicates the pulse duration, which ranges from a few milliseconds to Δ (in this case it is the same configuration as that in figure 2.2) [Johansen-Berg and Behrens, 2013].

by the first. Therefore, application of gradients in the presence of diffusion leads to a phase dispersion across the sample, which is reflected in signal loss at the time of acquisition. It is straightforward to notice the dependence of this process on the diffusion coefficient, D, the amplitude and duration of the magnetic field gradient, and the delay. For instance, increasing the delay between gradients Δ will increase the diffusion time T_d; this, according to Equation 2.6, will in turn increase the mean square displacement. So, as the spins displacement grows, the phase reversal becomes worse, finally leading to a greater signal loss due to a greater phase cancellation.

Mathematical description

Rather then dealing with the MR signal itself, for a clear mathematical description it is convenient to introduce a new quantity, $E(q)$, called the MR signal attenuation. It is obtained by dividing the diffusion-attenuated signal, $S(q)$, by the signal in the absence of any diffusion gradients, $S_0 = S(0)$. Since relaxation-related signal attenuation is approximately independent of the applied diffusion gradients, dividing $S(q)$ by S_0 eliminates the effects of relaxation, and the q-dependence of $E(q)$ is only due to diffusion. The MR signal attenuation is then given by:

$$E(q) = \int \rho(x_1) \int P(x_1, x_2, \Delta) e^{-iq(x_2 - x_1)} dx_2 dx_1 \tag{2.8}$$

where x_1 and x_2 are the positions of the particles during the application of the first and second pulse, respectively, $\rho(x_1)$ is the spin density at the time of application of the first pulse quantifying the likelihood of finding a spin at location x_1, and $P(x_1, x_2, \Delta)$ is

the diffusion propagator (Green's function) that describes the likelihood that a particle initially located at x_1, after a time Δ, will end up at location x_2. These last two quantities are related through the expression:

$$\lim_{t\to\infty} P(x_1, x_2, \Delta) = \rho(x_1) \tag{2.9}$$

Finally, the exponential term in (2.8) can be written as:

$$e^{-iq(x_2-x_1)} = \cos(q(x_2 - x_1)) - i\sin(q(x_2 - x_1)) \tag{2.10}$$

and incorporates the phase change induced by diffusion.
In the case of free diffusion, the propagator function is a Gaussian, and the expression for the signal attenuation is itself Gaussian, $E(q) = e^{-q^2 D\Delta}$. This is a special case of the more general Stejskal-Tanner relation, which also considers the pulses duration:

$$E(q) = e^{q^2 D(\Delta-\delta/3)} = e^{-bD} \text{ , where } b = q^2(\Delta - \delta/3) = \gamma^2\delta^2 G^2\left(\Delta - \frac{\delta}{3}\right) \tag{2.11}$$

Stejskal employed this formalism in the case of free, unrestricted, anisotropic diffusion, introducing a tensor (a 3×3 matrix) representing the natural orientation of anisotropic diffusion with respect to the three axis of the laboratory reference frame, identified by the orthogonal orientations of the magnetic field gradients produced by the three gradient coils.

2.1.3 Diffusion weighted imaging (DWI)

The use of gradients to enhance the diffusion-related signal attenuation lays the foundation for a new imaging modality, based on a contrast mechanism different than the one used in relaxation-weighted MRI. Such maps of the signal intensity S are called *diffusion-weighted* images. This technique is particularly useful when it comes to neuroimaging, as medical emergencies such as ischemic stroke can be detected much earlier than by traditional T1- and T2-weighted MRI images [Moseley et al., 1990]. Since the signal only depends on the b-value and on D, the goal after each acquisition is to estimate the diffusion coefficient, possibly for each one of the voxels composing the image. To do so, a minimum of two signal measurements is needed, one with diffusion encoding gradients applied and one without (Figure 2.4).
Actually, the diffusion coefficient is not estimated directly with dMRI. Rather, it is inferred from observations of the displacements over a given period of time. For example, observing water molecules that diffuse and encounter any hindrances along their path (such as cell membranes and macromolecules), the mean squared displacement depicted

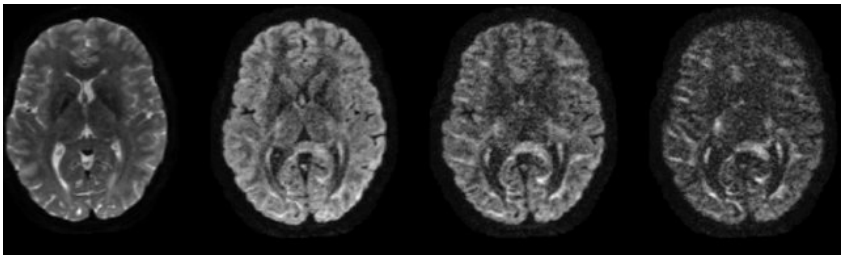

Figure 2.4: Brain DWI images in axial view, obtained using 4 different b-values (from left to right: 0, 1000, 2000, 3000 s/mm^2). The signal attenuation as a function of the b-value can be noticed [Descoteaux, 1999].

in Equation 2.6 will be lower than the one observed with free diffusion. Hence, the diffusion coefficient calculated with Equation 2.6 is lower than the actual one. For this reason it is introduced the *apparent diffusion coefficient* (ADC), which takes into account the effect of hindrances in tissues.

In biological tissues, in fact, one must consider that the actual diffusion distance is reduced - compared to free water - and the distribution, of course, is no longer Gaussian. As a matter of fact, water molecules move in a restricted way: the presence of biological elements such as cell membranes, fibers or macromolecules constitutes an obstacle to free diffusion.
The idea behind diffusion MRI is hence deeply rooted in this different behaviors of diffusion, which is a reflection of the biological architecture of the medium. While diffusion may actually reflect the viscosity of the medium in short diffusion times, as the time increases, the effects of the hidden biological structure become dominant. In particular, diffusion MRI has a significant better resolution with respect to other imaging techniques, being capable to scan tissues at a micrometer scale, instead of a millimetric one. Another advantage of this technique is its capability to perform experiments and studies on living subjects in a non-invasive manner. For this reason, diffusion MRI is one of the golden standards in the study of neural tissues, being able to reflect the fine structures and the architecture of tissues, hence the littlest changes in those features with physiological or pathological states [Le Bihan and Johansen-Berg, 2012].

2.2 Basic modeling of the diffusion signal: the diffusion tensor model

When we consider diffusion we have to make a fundamental distinction whether it is the case of *isotropic* or *anisotropic* diffusion. Isotropic diffusion occurs equally in all

directions, and a surface of constant mean-squared displacement can be represented by a diffusion sphere. In contrast, in many biological tissues including white matter, skeletal and cardiac muscle, diffusion is anisotropic, as the measured value depends on the direction. The surface of constant mean-squared displacement is then represented by a diffusion ellipsoid (Figure 2.5).

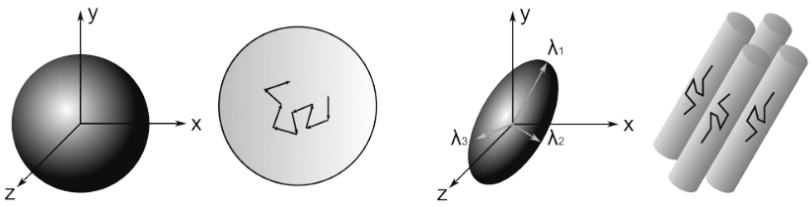

Figure 2.5: Diffusion sphere representing isotropic diffusion, hence equal in all directions (left) and diffusion ellipsoid representing anisotropic diffusion (right). The eigenvalues λ_1, λ_2, λ_3 in the diffusion ellipsoid are obtained from the diffusion tensor, while the relative eigenvectors indicate the direction of maximum and minimum diffusivity [Winston, 2012].

Mathematical description

Because anisotropic diffusion cannot be adequately represented by a single scalar ADC, there is the need to introduce a new mathematical instrument, the *diffusion tensor*, to characterize Gaussian diffusion in which the displacements per unit time are not the same in all directions:

$$\mathbf{D} = \begin{bmatrix} D_{xx} & D_{xy} & D_{xz} \\ D_{xy} & D_{yy} & D_{yz} \\ D_{xz} & D_{yz} & D_{zz} \end{bmatrix} \tag{2.12}$$

The diffusion tensor is a 3×3 symmetric matrix of variances and covariances, quantifying the diffusion along the orthogonal axes with its diagonal elements (i.e. the three logical axes of the scanner measurement frame), while the off-diagonal elements correspond to the correlation between these displacements. When the tensor is diagonalized, the three eigenvalues λ_1, λ_2 and λ_3 correspond to the three diffusivities along the principal axes of the diffusion tensor. The orientation of the principal axes is given by the three eigenvectors ε_1, ε_2 and ε_3, which are mutually orthogonal. The largest eigenvalue is associated to the principal eigenvector, ε_1, which indicates the orientation of the tensor, and hence, the orientation of the dominant fiber within the voxel.

2.2.1 Trace and Anisotropy Indices

Among the parameters that can be derived from diffusion tensor imaging (DTI), the most clinically useful is the *trace* of the tensor. It is the sum of the three diagonal elements, which is the same as the sum of its eigenvalues. This quantity is important because it is proportional to the orientationally averaged apparent diffusivity, so it removes the orientational dependence of the ADC. The trace divided by 3 yields the mean diffusivity (MD); in clinical studies, where the b-value used is around 1500 s mm^{-2}, the MD is roughly the same throughout all the brain parenchyma (the functional tissue in the brain, made by neurons and glial cells) [Pierpaoli et al., 1996].
Moreover, another information that can be derived from the diffusion tensor is the amount of anisotropy of diffusivity. In particular, two indices exist, the *fractional anisotropy* (FA) and the *relative anisotropy* (RA). Both values are derived from the variance of the three eigenvalues about their mean, after the variance is normalized to account for regional differences in the overall magnitude of diffusivity. The values for FA and RA are then given by:

$$FA = \sqrt{\frac{3}{2}} \frac{\sqrt{(\lambda_1 - \langle\lambda\rangle)^2 + (\lambda_2 - \langle\lambda\rangle)^2 + (\lambda_3 - \langle\lambda\rangle)^2}}{\sqrt{\lambda_1^2 + \lambda_2^2 + \lambda_3^2}} \tag{2.13}$$

and

$$RA = \sqrt{\frac{1}{3}} \frac{\sqrt{(\lambda_1 - \langle\lambda\rangle)^2 + (\lambda_2 - \langle\lambda\rangle)^2 + (\lambda_3 - \langle\lambda\rangle)^2}}{\langle\lambda\rangle} \tag{2.14}$$

where $\langle\lambda\rangle$ is one third of the trace of the tensor. Hence, FA is a measure of the tensor fraction that is related to anisotropic diffusion. This index is also normalized, to yield a value equal to zero when diffusion is isotropic, and equal to one for a fully anisotropic diffusion (i.e. constrained along one axis only). RA, instead, compares the "magnitudes" of the anisotropic component of diffusion with the isotropic part, by looking at the ratio of the variance of the eigenvalues to their mean (the mean diffusivity).

DTI metrics in assessing the gravity of Alzheimer's

Diffusion Tensor Imaging (DTI) is a powerful tool in neuroimaging that allows the study of white matter integrity by analyzing the diffusion of water molecules in the brain. The classical DTI metrics introduced above, MD and FA, are frequently used in research on Alzheimer's Disease.
In particular, increased MD is generally associated with neurodegeneration, reflecting tissue damage, such as loss of neurons, myelin and overall tissue integrity. On the contrary, FA typically decreases in AD patients, indicating degeneration of white matter tracts. Several studies have investigated the use of MD an FA metrics to distinguish between AD, MCI and healthy controls. In 2011, a research conducted on case-control studies of DTI in patients with AD and MCI, found out that MD tends to increase

in patients with AD compared to healthy controls. In MCI patients, MD is also elevated, but typically to a lesser extent than in AD patients. Additionally, FA decreases greatly in AD, while patients with MCI have lower values, but not as much as AD [Sexton et al., 2011]. Other studies have instead extended the analysis of DTI metrics beyond white matter to gray matter, showing that MD can be a marker of neurodegeneration in both AD and MCI, particularly in the hippocampus and other gray matter regions [Acosta-Cabronero et al., 2012].

Limitations of DTI: multiple fibers

Whilst the diffusion tensor model provides helpful quantitative parameters, its description of the brain's architecture is not so accurate, especially considering the dimensions of neural tissue. In fact, white matter axons are tiny compared to typical MRI voxels. Axon radii are in the range [0.1, 10] μm, whereas voxels typically have sizes in the range [1, 5] mm. Therefore, inside each voxel there are hundreds of thousands of axon fibers, which can assume configurations that are way more complex than the parallel (fanning, bending, crossing). Moreover, given the dimensions of a voxel, it could happen that inside a voxel there are not only axons. In fact, a mixture of white matter, gray matter and cerebrospinal fluid might be contained within it.

Towards complex methods

To overcome this limitation, more complex methods have been proposed, and those used in this thesis work are discussed in detail in the following sections. Before starting the detailed explanation, some additional information about the state-of-the-art must be addressed. Currently, there are two main approaches to extracting information from dMRI data: signal representations and biophysical models [Jelescu and Budde, 2017]. The former are briefly described in the following paragraph, while the latter (which includes most of the models used in this thesis) will be devoted a separate section.

Signal representations

Signal representations comprehend all the techniques which attempt to describe the diffusion signal without assuming any particular structure of the examined tissue. DTI is an analysis method falling in this category. Since there is no assumption about the underlying tissue, metrics derived from the diffusion tensor can be used indistinctly on both healthy and diseased subjects. This well summarizes the strength and weakness of this class of methods: while they can be used almost universally for the study of the brain in any condition, the estimated parameters lack specificity and allow only for an indirect characterization of microstructure.

2.3 Multi Compartment models: a biophysical interpretation of white matter

A first attempt to describe the diffusion signal of white matter as multi-compartmental was made in 1997 by Stanisz and was based on electron micrographs of bovine optic nerve [Stanisz et al., 1997]. Multi Compartment models focus on the description of the anisotropic intra-axonal and extra-axonal diffusivity and the isotropic diffusivity. But to proper understand the biophysical assumptions and description of those methods, a brief parenthesis on the morphology of the white matter is necessary.

2.3.1 Morphological features of white matter

The white matter is composed of several cellular components. The axonal projections leaving and entering the cortical layers are the most important part of the white matter, whereas the role of all the other cellular components is supporting this complex neuronal fiber network. In general, the cellular components of white matter can be divided into four categories: the vascular capillary bed, glial cells, axons, and extracellular/axonal space.
The axon is a long fiber that extends from the neuronal cell body. The majority of them are surrounded by a lipid-rich myelin sheath that renders the tracts white (hence the name white matter). Oligodendrocytes constitute one of the two classes of glial cells, and they produce the myelin sheath and support axonal structure and integrity throughout life. The other important class of glial cells are the atrocytes, that play numerous support roles including regulating extracellular ion concentration and providing trophic and possibly metabolic support for neurons and oligodendrocytes.
Axons can be myelinated or unmyelinated. In myelinated axons, the myelin sheath wrapping the body of the axon is not continuous, but has small gaps called nodes of Ranvier. Within the axon, microtubular fibers with the same alignment of the axon itself, strenghten the cylindrical shape and orientation of the fiber. The diameter of the axons and the myelin membrane are proportionally related to the conduction velocity along the axon, and are usually characterized by an axon diameter distribution.
Axons occupy the lowest step in the hierarchical and organized structure of the nervous system. A single axon, with all its branches taken together, can innervate multiple parts of the brain and generate thousands of synapses. A bundle of axons constitute a nerve tract in the central nervous system, and a fascicle in the peripheral nervous system. Nerve tracts can be made up by 200 million axons, as in the case of the *corpus callosum* in the human brain.

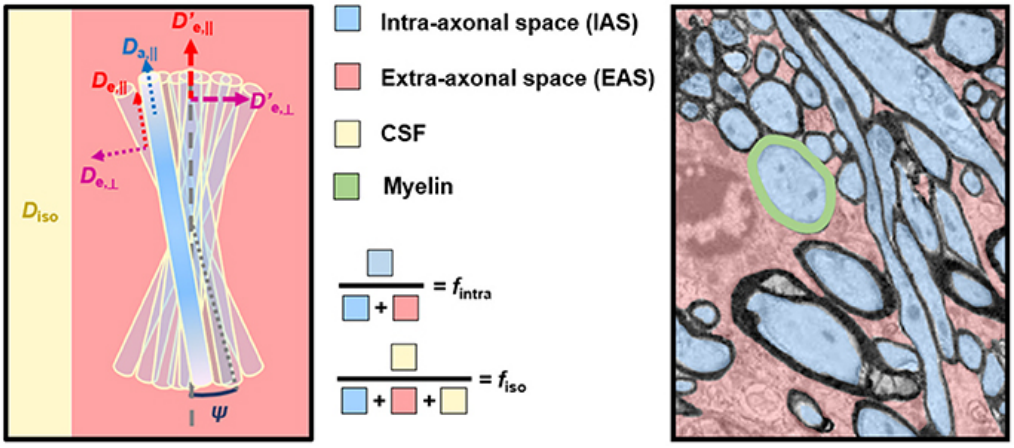

Figure 2.6: Model compartments (left) and their corresponding biological components (right). On the left, schematic description of a three-compartment model: $D_{e,\perp}$ and $D_{e,\parallel}$ are local extra-axonal diffusivities, and $D'_{e,\perp}$ and $D'_{e,\parallel}$ are apparent extra-axonal diffusivities, depending on the chosen model. On the right, a cross-sectional color-coded image of a WM bundle (notice the absence of the myelin in the model, as explained) [Jelescu and Budde, 2017].

2.3.2 Biophysical models of diffusion in white matter

The model proposed by [Stanisz et al., 1997] assumed axons as prolate ellipsoids, and glial cells as spheres, with the extracellular space constituting the third compartment. Their model also accounted for membrane permeability of both axons and glial cells. But in a dMRI experiment it can be noticed that at long diffusion times, the diffusivity across axons tends to zero. For this reason, axons can be in principle modeled as infinitely long "sticks", or cylinders with zero radius [Behrens et al., 2003]. Behrens assumed that water in and around the axons similarly diffused only in the fiber direction with a second compartment of free, isotropically diffusing water.
Most of the white matter models currently in use, rely on the same common idea, in which the water signal retrieved from dMRI is assumed to originate from two to three closed compartments, each weighted by their relative volume fractions (Figure 2.6). Although the myelin sheath is present in the WM, because of its short T_2 is it absent in the modeling.

- The first compartment is made by axons, modeled as infinitely long cylinders. The orientation of each fiber is characterized by a orientation distribution function (ODF) which changes according to the model used. The diffusivity of water in this compartment is assumed to be zero perpendicular to the axon, and $D_{a,\parallel}$ inside of it.

- The second compartment is the extra-axonal space, which comprehend the ex-

tracellular fluid, glial cells and cell somas. In this compartment the diffusion is assumed to be an anisotropic Gaussian, with axonal diffusivity $D_{e,\parallel}$ and radial diffusivity $D_{e,\perp}$. These quantities are defined locally in proximity of a coherent axon sub-bundle with the resulting signal convolved with the ODF, or as apparent diffusivities over the entire voxel.

- The third compartment is modeled as an isotropic Gaussian, and is characterized by a diffusivity D_{iso}, whose parameterization changes according to the chosen model. For example, for water diffusing freely as the cerebrospinal fluid (CSF), then $D_{iso} = D_{free} = 3\ \mu\text{m}^2/\text{ms}$ *in vivo*.

2.4 NODDI: Neurite Orientation Dispersion and Density Imaging

Many other models, such as CHARMED (Composite Hindered And Restricted ModEl of Diffusion) [Assaf and Basser, 2005], can provide sensible maps of the volume fraction intra-cellular space, the axon density, in *in vivo* human brain imaging. However, by representing axons as parallel cylinders, CHARMED (as well as other compartment models) cannot recover the effect of axonal-orientation dispersion due to bending and fanning of axon bundles widespread through the brain [Bürgel et al., 2006]. NODDI (Neurite Orientation Dispersion and Density Imaging) is then developed as a clinically feasible technique for *in vivo* neurite orientation dispersion and density imaging [Zhang et al., 2012]. The idea behind NODDI is to choose a model sufficiently simple, yet complex enough to capture the key features of neurite morphology. Specifically, NODDI is an adaptation of the orientation-dispersed cylinder model [Zhang et al., 2011], which only estimates the neurite density and orientation dispersion. For the acquisition protocol, this is determined using the experiment design optimization proposed by [Alexander, 2008].

Overview of NODDI

NODDI belongs to the family of multi-compartment models, which interpret the MRI signal in each voxel as the sum of the contributions from the individual compartments. NODDI is described as a "two-level multi-compartment model": in the first level, a distinction is made between the isotropic components (which can be characterized by the free water fraction f_w, estimating the extent of CSF contamination) and tissues. The second levels unpacks the tissues component, further dividing it into an intra-neurite and an extra-neurite compartment. The first fraction is described by the neurite density index (NDI), which quantifies the packing density of axons or dendrites. The second fraction is described by the orientation dispersion index (ODI), which assesses the orientation coherence of neurites, and ranges between 0 for perfectly aligned straight fibers and 1 for completely isotropic. Figures 2.7 and 2.8 illustrate the definition of these three key metrics and the comparison between spatial maps provided by DTI and NODDI metrics, respectively.

2.4.1 Mathematical description

As mentioned, NODDI adopts a tissue model that distinguish three types of microstructural environment, each one affecting water diffusion in a unique way. Hence, the full normalized signal A [Zhang et al., 2012] can be written as:

$$A = (1 - \nu_{iso})(\nu_{ic}A_{ic} + (1 - \nu_{ic})A_{ec}) + \nu_{iso}A_{iso} \tag{2.15}$$

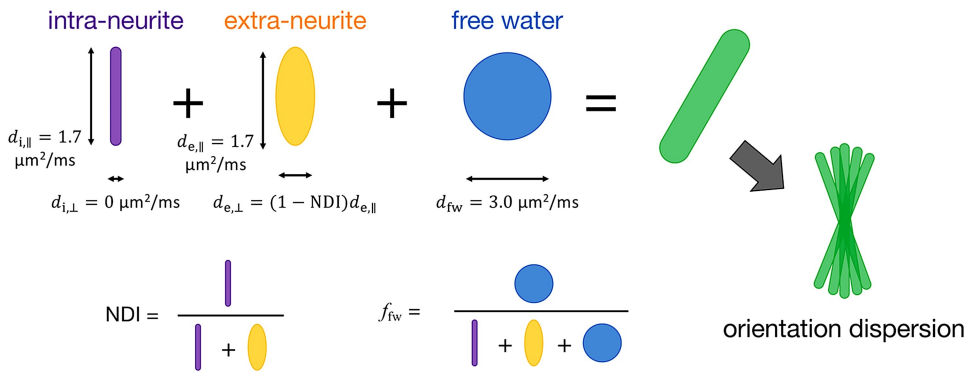

Figure 2.7: Schematic illustration of the NODDI metrics and parameter constraints [Kamiya et al., 2020].

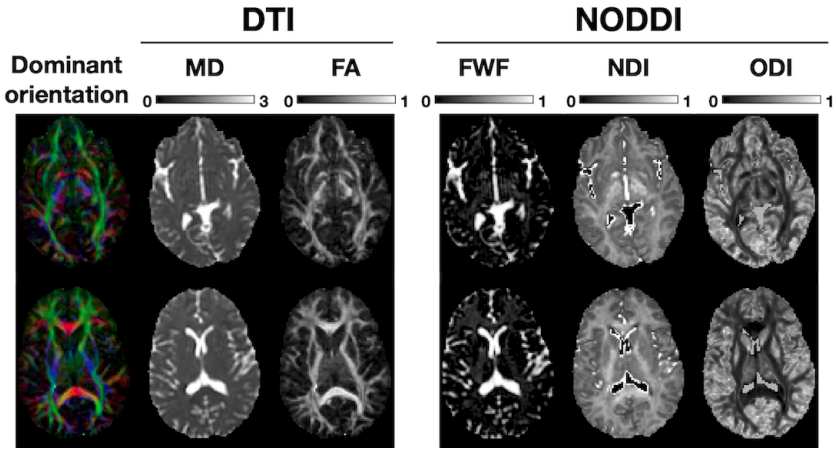

Figure 2.8: Comparison between DTI maps and NODDI maps, obtained from an example dataset provided by [Kraguljac et al., 2022].

where A_{ic} and ν_{ic} are the normalized signal and volume fraction of the intra-cellular compartment, A_{ec} is the normalized signal of the extra-cellular compartment, and A_{iso} and ν_{iso} are the normalized signal and volume fraction of the CSF compartment.

The intra-cellular compartment is modeled as a set of sticks (cylinders with zero radius), whose orientation distribution can range from highly parallel to highly dispersed. The normalized signal A_{ic} then adopts the orientation-dispersed cylinder model in [Zhang et al., 2011], but simplified for sticks:

$$A_{ic} = \int_{\mathbb{S}^2} f(\boldsymbol{n}) e^{-bd_{\parallel}(\boldsymbol{q}\cdot\boldsymbol{n})^2} d\boldsymbol{n} \tag{2.16}$$

where $\boldsymbol{q}$ and b are the gradient direction and b-value of diffusion-weighting, respectively; $f(\boldsymbol{n})d\boldsymbol{n}$ gives the probability of findings sticks along orientation $\boldsymbol{n}$; $e^{-bd_{\parallel}(\boldsymbol{q}\cdot\boldsymbol{n})^2}$ gives the signal attenuation due to unhindered diffusion along a stick with intrinsic diffusivity $d_{\parallel}$ and orientation $\boldsymbol{n}$. In particular, the orientation distribution function $f : \mathbb{S}^2 \mapsto \mathbb{R}$ is modeled with a Watson distribution:

$$f(\boldsymbol{n}) = M\left(\frac{1}{2}, \frac{3}{2}, \kappa\right)^{-1} e^{\kappa(\boldsymbol{\mu}\cdot\boldsymbol{n})^2} \tag{2.17}$$

where M is a confluent hypergeometric function, $\boldsymbol{\mu}$ is the mean orientation and κ is the concentration parameter that measures the extent of orientation dispersion about $\boldsymbol{\mu}$. The Watson distribution is chosen over the truncated spherical harmonic series, as it can better represent not only the high orientation dispersion in GM but also the low orientation dispersion in WM.

The extra-cellular compartment refers to the space around neurites, where diffusion is hindered by the presence of all the different types of glial cells and cell bodies, but not restricted, and hence is modeled with a simple (Gaussian) anisotropic diffusion. The normalized signal A_{ec} again adopts the extra-cellular signal model of orientation-dispersed cylinders in [Zhang et al., 2011]:

$$logA_{ec} = -b\boldsymbol{q}^T \left(\int_{\mathbb{S}^2} f(\boldsymbol{n}) D(\boldsymbol{n}d\boldsymbol{n})\right) \boldsymbol{q} \tag{2.18}$$

where $D(\boldsymbol{n})$ is a cylindrically symmetric tensor having $\boldsymbol{n}$ as the principal direction of diffusion, diffusion coefficients $d_{\parallel}$ parallel to $\boldsymbol{n}$ and $d_{\perp}$ perpendicular to $\boldsymbol{n}$. The parallel and perpendicular diffusivities are set as the same as the intrinsic free diffusivity of the intra-cellular compartment and with a simple tortuosity model, respectively, as $d_{\perp} = d_{\parallel}(1 - \nu_{ic})$, where ν_{ic} is the intra-cellular volume fraction. Using the Watson distribution as before, the parallel and perpendicular diffusivities of the apparent extra-cellular

diffusion tensor can be written as:

$$\begin{aligned} d'_{\parallel} &= d_{\parallel} - d_{\parallel}\nu_{ic}(1-\tau_1) \\ d'_{\perp} &= d_{\parallel} - d_{\parallel}\nu_{ic}\frac{1-\tau_1}{2} \end{aligned} \tag{2.19}$$

where τ_1 captures the effect of orientation dispersion on the apparent diffusivites, and can be written in terms of the Dawson's integral F, to give:

$$\tau_1 = -\frac{1}{2\kappa} + \frac{1}{2F(\sqrt{\kappa})\sqrt{\kappa}} \tag{2.20}$$

In particular, τ_1 ranges from 1/3 for isotropically-dispersed orientations ($\kappa = 0$) to 1 for strictly parallel orientations ($\kappa = \infty$). By looking at Equation 2.19, a significant difference between NODDI extra-cellular model and earlier models such as CHARMED can be noticed [Assaf and Basser, 2005]. Unlike models like CHARMED, which treat the apparent and perpendicular diffusivities in the extra-cellular space as independent free parameters, the NODDI model expresses them in terms of the neurite morphology and the intrinsic diffusivity, giving them a greater physical significance.

Finally, the CSF compartment models the space occupied by the cerebrospinal fluid, and is hence modeled as isotropic Gaussian diffusion with diffusivity d_{iso}.
Moreover, Zhang et al. redefine the orientation dispersion index [Zhang et al., 2012] they first proposed in their previous paper [Zhang et al., 2011] as:

$$ODI = \frac{2}{\pi}\arctan(1/\kappa) \tag{2.21}$$

With this new definition, the ODI index can range from 0 to 1, making it more straightforward to visualize, with respect to the previous definition ($OD = \kappa$) which has an upper bond that is infinity.

2.4.2 Limitations of NODDI

The Watson distribution, utilized in the NODDI model, has been instrumental in advancing our understanding of brain microstructure by estimating neurite density and orientation dispersion. However, its primary limitation lies in its assumption of a single dominant orientation with symmetrical dispersion, which simplifies the complex architecture of brain tissues.
This unimodal approach is effective in regions with well-aligned fibers, such as major white matter tracts, but falls short in areas where multiple fiber orientations intersect or where neurite dispersion is more irregular.
As a result, the Watson-based NODDI model may not fully capture the intricacies of

brain regions with complex fiber configurations, potentially leading to less accurate assessments of microstructural changes. To overcome these challenges, other models (such as the NODDI-Bingham model) were developed, offering a more sophisticated approach by accounting for anisotropic dispersion, thereby providing a more nuanced and accurate representation of brain tissue.

2.5 NODDI-Bingham

The NODDI model described in the last chapter was adapted by [Tariq et al., 2016], who proposed a similar method to estimated anistotropic orientation dispersion of neurites. This method uses NODDI, but models the function through a Bingham distribution, instead of a Watson. As a matter of fact, the Bingham distribution allows us to capture the anisotropic dispersion in a much better and comprehensive way, being the Watson a special case of the Bingham distribution itself.
The Bingham distribution [Bingham, 1974] is a parametric orientation distribution that can also be described as the spherical analogue of a Gaussian distribution in two dimensions. The probability density of an orientation along $\hat{n}$ for this distribution is defined in terms of a 3x3 symmetric matrix, $\mathbf{B}$:

$$f(\hat{n};\mathbf{B}) = \frac{1}{c_B}\exp(\hat{n}^\top \mathbf{B}\hat{n}) \tag{2.22}$$

with c_B being a constant that can be derived through normalization, and is expressed by:

$$c_B =_1 F_1\left(\frac{1}{2};\frac{3}{2}\mathbf{B}\right) \tag{2.23}$$

where ${}_1F_1$ is the confluent hypergeometric function of the first kind.
An algebraic representation for the Bingham distribution can be obtained by expressing $\mathbf{B}$ in terms of its eigendecomposition

$$\mathbf{B} = \mathbf{Q}\mathbf{D}\mathbf{Q}^{-1} = (\hat{\mu}_1\hat{\mu}_2\hat{\mu}_3)\begin{pmatrix}\kappa_1 & 0 & 0\\ 0 & \kappa_2 & 0\\ 0 & 0 & \kappa_3\end{pmatrix}\begin{pmatrix}\hat{\mu}_1^\top\\ \hat{\mu}_2^\top\\ \hat{\mu}_3^\top\end{pmatrix} \tag{2.24}$$

where the diagonal terms ($\kappa_1 \geq \kappa_2 \geq \kappa_3$) indicate the concentrations along the principal axes of diffusion. Since this distribution is invariant to addition of arbitrary constants to its eigenvalues, we can choose $-\kappa_3$ as the constant and rewrite Eq. 2.22 as:

$$f(\hat{n};\mathbf{B}) = \frac{1}{c_B}\exp\left(\kappa(\hat{\mu}_1\cdot\hat{n})^2 + \beta(\hat{\mu}_2\cdot\hat{n})^2\right) \tag{2.25}$$

where $\kappa = \kappa_1 - \kappa_3$ is the concentration parameter and $\beta = \kappa_2 + \kappa_3$ is the dispersion parameter. The degrees of freedom associated with this distribution are five, three

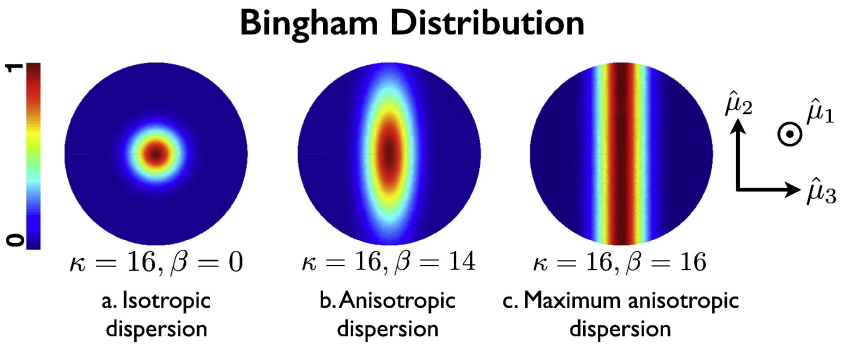

Figure 2.9: Probability density plots for the Bingham distribution [Tariq et al., 2016].

taking account for the orientations and two for the concentrations. Hence we only need two extra parameters to be determined for the orientation dispersion quantification of for NODDI-Bingham compared to NODDI-Watson, and these are the concentration parameter β and the angle, ψ.
Based on the parameters values there are different possible dispersion scenarios:

- when $\kappa > \beta > 0$ (Fig. 2.9b), anisotropic dispersion exists, and all orientations are well-defined and estimable;
- when $\kappa = \beta > 0$ (Fig. 2.9c), we have complete anistropic dispersion, leasing to indistinguishable and arbitrarily defined orientations;
- when $\kappa = \beta = 0$, the case is isotropic dispersion, where none of the orientations is uniquely defined;
- when $\kappa > 0, \beta = 0$ (Fig. 2.9a), the case is isotropic dispersion about a point, resulting in non-distinguishable orientations.

2.5.1 Mathematical description

In this implementation, the intra- and extra-neurite signals are introduced by c_B, the normalization constant associated with the Bingham distribution.
The determination of A_{ic} (we keep the same notation as NODDI-Watson for consistency) involves substituting Eq. 2.22 into Eq. 2.16 and subsequent manipulations, resulting in an expression akin to those presented by [Kaden et al., 2007] and [Sotiropoulos et al., 2012]. Here, c_Q denotes the normalization constant for the Bingham distribution, when the matrix is involved.

$$A_{ic} = \frac{c_Q}{c_B} = \frac{{}_1F_1\left(\frac{1}{2}; \frac{3}{2}; \mathbf{Q}\right)}{{}_1F_1\left(\frac{1}{2}; \frac{3}{2}; \mathbf{B}\right)} \tag{2.26}$$

For the computation of A_{ec}, we substitute Eq. 2.22 into the Diffusion Tensor expression in the extra-neurite space, $D_{ec} = \int_{\mathbb{S}} f(\hat{n})\mathbf{D}(\hat{n})\mathrm{d}\hat{n}$, to represent D_{ec} in terms of the parameters inherent in the Bingham distribution. Expressing D_{ec} in relation to its eigenvalues and eigenvectors is accomplished through

$$\mathbf{D}_{ec} = (\hat{\mu}_1\hat{\mu}_2\hat{\mu}_3)\begin{pmatrix} d_{\hat{\mu}_1} & 0 & 0 \\ 0 & d_{\hat{\mu}_2} & 0 \\ 0 & 0 & d_{\hat{\mu}_3} \end{pmatrix}\begin{pmatrix} \hat{\mu}_1^\top \\ \hat{\mu}_2^\top \\ \hat{\mu}_3^\top \end{pmatrix} \tag{2.27}$$

where $d_{\hat{\mu}_3}$ signifies the diffusivity along the n^{th} eigenvector of D_{ec}.
Notably, the diffusivities along the principal eigenvector of D_{ec} are derived by taking the partial derivative of c_B concerning the corresponding concentration parameter, as depicted in Eqs. 2.28 and 2.29.

$$d_{\hat{\mu}_1} = d_\perp + (d_\parallel - d_\perp)\frac{\partial c_B}{\partial \kappa} \tag{2.28}$$

$$d_{\hat{\mu}_2} = d_\perp + (d_\parallel - d_\perp)\frac{\partial c_B}{\partial \beta} \tag{2.29}$$

To obtain these derivatives numerically, we employ finite differences.
The diffusivity along $d_{\hat{\mu}_3}$ is then given by Eq. 2.30, leveraging the insight that $\mathrm{Tr}(\mathbf{D}_{ec}) = \mathrm{Tr}(\mathbf{D}(\hat{n}))) = d_\parallel + 2d_\perp$:

$$d_{\hat{\mu}_3} = d_\parallel + d_\perp - d_{\hat{\mu}_1} - d_{\hat{\mu}_2} \tag{2.30}$$

Dispersion parameters

We extend the application of Bingham-NODDI to assess the dispersion properties of neurites, introducing a generalized form of the orientation dispersion index (ODI) originally defined for Watson-NODDI.
The dispersion along the primary dispersion orientation, $d_{\hat{\mu}_2}$, and the one along $d_{\hat{\mu}_3}$ are respectively quantified by

$$ODI_P = \frac{2}{\pi}\arctan\left(\frac{1}{\kappa - \beta}\right) \tag{2.31}$$

$$ODI_S = \frac{2}{\pi}\arctan\left(\frac{1}{\kappa}\right) \tag{2.32}$$

Clearly, in the case of a Watson distribution where the concentration parameter $\beta = 0$, then the two expressions are equal and correspond to the already known ODI.

To gauge the comprehensive orientation dispersion, we note that the overall extent or

scattering of a multivariate normal distribution can be measured through the determinant of its covariance matrix. The total dispersion is then expressed by

$$ODI_{Tot} = \frac{2}{\pi} \arctan(|\Sigma_{Bing}|) \tag{2.33}$$

where

$$|\Sigma_{Bing}| = \sqrt{\left(\frac{1}{\kappa - \beta}\right)\left(\frac{1}{\kappa}\right)} \tag{2.34}$$

Dispersion anisotropy index

The parameter quantifying the dispersion anisotropy of neurites is set as

$$DA_B = \frac{2}{\pi} \arctan\left(\frac{\beta}{\kappa - \beta}\right) \tag{2.35}$$

and ranges between 0 (isotropic dispersion, as $\beta = 0$) and 1 (as $\kappa = \beta$).
DA_B serves as a metric that is responsive to alterations in anisotropic dispersion, capturing nuances that might not influence the overall dispersion. Consequently, DA_B proves valuable in quantifying anisotropy, even within white matter tracts as cohesive as the corpus callosum, known for its pronounced bends.
Another index that is meaningful in this context is the dispersion anisotropy proposed by [Tariq et al., 2014] that is based on the orientation tensor $\mathbf{T}$

$$DA_T = \frac{(\tau_2 - \tau_3)}{\tau_1} \tag{2.36}$$

where τ_n are the eigenvalues of the tensor T, which corresponds to the second moment of and ODF, and those eigenvalues are functions of the known parameters κ and β. As the previous parameter, DA_T also ranges from 0 to 1, and can be though of as the product between the overall dispersion, ODI_{Tot}, and DA_B.

DA_B holds significance as it stands orthogonal to the overall dispersion measure ODI_{Tot}. It uniquely quantifies the anisotropy in the orientation dispersion of neurites, setting it apart from DA_T, which is influenced by the overall dispersion through weighting.
Also, it must be noticed that both dispersion indexes change as the dispersion anisotropy changes, but a change in the parameters κ and β means an increase in DA_T only, as long as the ratio between the two parameters remains the same. Hence, while DA_B only reflects the dispersion anisotropy about $d_{\hat{\mu}_1}$, DA_T also reflects the change in dispersion. For this reason, anisotropic dispersion can be identified as the difference between ODI_P and ODI_S, but its quantity is directly related to the value of DA_B only.

2.6 Alzheimer's disease and its effects on the brain's microstructure

Alzheimer's disease (AD) represents the most common form of dementia, and as all forms of dementia, it involves a progressive decay of cognitive functions, starting from memory. According to the WHO (World Health Organization), over 55 million people live with dementia. The importance of this number is greater if one considers that it grows on a regular basis, with a prevision of 78 million affected by AD by 2030.
Nowadays, most of the current research on AD is focused on the prodromal phase of the disease: at this stage, while symptoms have not developed yet, pathological changes are occurring already. Most commonly, AD is characterized by extracellular amyloid beta (Aβ) plaques and neurofibrillary tangles, however white matter damage is also present at early stages of the disease and contributes in the pathophysiology [Hyman et al., 2012], [Sperling et al., 2011].
Another way in which AD impacts the brain microstructure is related to neuronal loss. As a matter of fact, AD leads to the gradual loss of neurons, particularly in areas crucial for memory and cognitive functions such as the hippocampus and cortex. This neuronal loss contributes to the overall shrinkage of the brain tissue ans also affects the synaptic functions. Synapses, namely the connections between neurons that make up the white matter, are in fact disrupted in patients affected by Alzheimer's: this loss impairs communication between neurons, affecting cognitive functions and memory. In particular, all these changes can be clearly noticed by looking at the WM structure and the alterations or disruptions in the nerve fibers.

2.6.1 Microstructural imaging for early detection and monitoring of Alzheimer's disease

NODDI offers significant potential for detecting Alzheimer's disease by revealing microstructural brain changes that are often invisible to conventional MRI. Through the quantification of neurite density, NODDI can detect early neuronal loss and synaptic degradation, which are hallmarks of Alzheimer's, particularly in regions like the hippocampus and entorhinal cortex. Additionally, by measuring the orientation dispersion of neurites, NODDI captures the structural complexity of the brain, highlighting areas where neural pathways may become disorganized due to disease progression. This technique is also valuable in differentiating between mild cognitive impairment (MCI) and Alzheimer's, as it can identify subtle changes in brain microstructure that precede more pronounced neurodegeneration. Moreover, NODDI's ability to assess both white and gray matter integrity makes it a powerful tool for early diagnosis, tracking disease progression, and evaluating treatment efficacy. By complementing other imaging modalities and biomarkers, NODDI contributes to a more comprehensive understanding of

Alzheimer's, ultimately aiding in the early detection and management of the disease.

2.6.2 Brain microstructure and principal observation areas

This work will focus on the analysis and comparison of the metrics extracted by the two proposed models, inside certain specific areas of the brain, whose anatomy and functions will be briefly described in the following paragraphs.

Cerebral cortex

The cerebral cortex is perhaps the most widely known structure of the brain. It is essentially composed by a Grey Matter layer, which is about 2 to 4 mm thick, and covers the whole structure of the two cerebral hemispheres. The surface is folded upon itself, with many elevated ridges of tissue called *gyri*, and grooves called *sulci*. This pattern is of great importance, since it increases the surface area of the cortex, and therefore the number of neurons within it.
The cerebral cortex is divided into six *lobes*, based on the disposition of the five major sulci. Four out of six take their names from the cranial bones underneath, and these are the frontal, parietal, temporal and occipital lobes. The remaining two are the insular and limbic lobes, the former being located deep to the lateral sulcus and the latter on the medial aspect of the hemisphere.
The intricate structure of the cerebral cortex delineates distinct functional domains tasked with processing diverse stimuli and governing specific cognitive faculties such as sensory perception, motor coordination, and higher-order thinking. Through a complex network, neurons within this cortical region receive signals from various subcortical structures relayed by the thalamus, as well as from neighboring cortical regions through association fibers. In reciprocal fashion, neuronal pathways from the cerebral cortex extend to multiple destinations within the central nervous system, encompassing other cortical zones, the thalamus, basal nuclei, brainstem nuclei, pontine nuclei, cerebellum, and spinal cord.

White Matter

White matter is primarily composed of myelinated nerve fibers, which are extensions of nerve cells, also known as neurons. Such fibers are bundled together into tracts that facilitate the communication between different regions of the brain and other parts of the nervous system.
White matter is responsible for a number of various and important functions. First and foremost, it is accountable for the transmission of signals, creating a communication network and passing along electrical signals between different areas of the brain, allowing for the integration of sensory, motor, and cognitive functions. It also integrates

the information processed in different areas of the brain, allowing for complex functions such as memory, language, and decision-making. In addition, WM plays a crucial role in learning and memory processes by facilitating the communication between different brain regions involved in memory formation and retrieval. Furthermore, WM tracts facilitate the transmission of signals necessary for coordinating voluntary movements and motor functions.
Overall, WM is essential for the efficient functioning of the brain, enabling communication between various regions and facilitating complex cognitive processes and behaviors.

Lateral Ventricle

The lateral ventricles are the largest of four interconnecting cavities within the brain that constitutes the cerebral ventricular system. These cavities are filled with cerebrospinal fluid (CSF) and provide passage to its circulation. The central part of the lateral ventricle is elongated from the anterior to the posterior part of the brain, and in this last part it reaches the splenium of the corpus callosum.

Thalamus

The thalamus is a bilateral structure located deep within the brain, situated between the cerebral cortex and the midbrain. It serves as a critical relay and integration center for sensory and motor signals traveling between various regions of the brain.
Functionally, the thalamus acts as a gateway for sensory information by receiving inputs from sensory pathways such as the optic tract (vision), auditory pathways, somatosensory pathways (touch, temperature, pain), and gustatory (taste) and olfactory (smell) systems. It then processes and relays these sensory signals to the appropriate regions of the cerebral cortex, where further processing and perception occur.
Additionally, the thalamus plays a crucial role in regulating motor functions by receiving inputs from the basal ganglia and cerebellum and relaying them to the motor cortex, contributing to the coordination and execution of voluntary movements.
Beyond sensory and motor functions, the thalamus is also involved in various cognitive processes such as attention, consciousness, and arousal, as it projects widespread connections to cortical areas involved in these functions.
Overall, the thalamus serves as a vital hub for sensory, motor, and cognitive processing, facilitating communication between different brain regions and contributing to the integration of sensory inputs and motor outputs essential for perception, action, and cognition.

Caudate nucleus

The caudate nucleus, situated adjacent to the putamen and delineated from it by the internal capsule, exhibits a distinctive C-shaped structure wrapping around the thalamus.

Functionally, the caudate nucleus is integral to a range of cognitive processes, encompassing learning, memory, and executive functions, alongside its involvement in the initiation and regulation of voluntary movements, particularly those demanding precise coordination and planning. Additionally, it is implicated in reward processing, decision-making, and emotional regulation.
Receiving input from diverse regions of the cerebral cortex, including motor, cognitive, and emotional areas, the caudate nucleus integrates these inputs and transmits output signals to other basal ganglia nuclei, as well as to cortical and limbic structures. This contributes to the coordination of both motor and cognitive functions.
Disruption of caudate nucleus function is linked with various neurological and psychiatric disorders, such as Parkinson's disease, Huntington's disease, obsessive-compulsive disorder (OCD), and addiction, underscoring its significance across both motor and cognitive domains of brain function.

Putamen

The putamen is a subcortical structure located within the basal ganglia of the brain, specifically part of the corpus striatum. It is situated adjacent to the caudate nucleus and is separated from it by a white matter tract known as the internal capsule.
Functionally, the putamen is primarily involved in the modulation and coordination of voluntary motor movements. It receives input from various regions of the cerebral cortex, particularly motor areas, and also receives indirect input from other basal ganglia nuclei, such as the substantia nigra and globus pallidus. These inputs are integrated within the putamen, which then sends output signals to the globus pallidus and thalamus, contributing to the regulation of motor functions.
The putamen is particularly implicated in the control of skilled and coordinated movements, including reaching, grasping, and walking. The putamen is also implicated in cognitive processes such as learning, memory, and reward processing, due to its connections with cortical and limbic regions involved in these functions. Its involvement in these cognitive processes underscores its role beyond motor control, highlighting its significance in broader aspects of brain function.

Pallidum

The globus pallidus, also known as pallidum, is a triangular-shaped, subcortical structure of the brain, part of the basal ganglia. It is located below the cerebral cortex, medial to the putamen. The globus pallidus can be functionally divided into two main parts, the medial (internal) segment and the lateral (external) segment. Together with the putamen, it comprises the larger lentiform (lenticular) nucleus tat lies beneath the insula. The lentiform nucleus and caudate form the corpus striatum, a critical component of the basal ganglia.

The main function of the globus pallidus is movement control. More specifically, it regulates conscious and voluntary movement. In addition, globus pallidus connects to cortical areas that support various functions, including movement and cognition.

Hippocampus

The hippocampus is a paired structure that can be found in each temporal lobe of the brain. It is part of a major structure called the hippocampal formation, which extends from the amygdala anteriorly to the splenium of the corpus callosum, posteriorly.
The hippocampus plays a number of crucial roles in regulating emotions, motivation, hormonal activity, autonomic activity and memory formation. This last one function is perhaps the most important one, with the hippocampus receiving and consolidating information, allowing for establishment of long-term memories, and it also plays an important role in spatial memory.
The hippocampus, along with the entorhinal cortex and amygdala, are early involved in the course of AD, and are typically found to be severely atrophied in the late stages of the disease.

Amygdala

The amygdala is a paired small, almond-shaped structure in the brain, and is part of the limbic system. It plays a role in handling emotions and implicit memory (or unconscious memory).

Accumbens

The nucleus accumbens is part of a large group if subcortical nuclei called the basal ganglia (basal nuclei), and it lies in th erostral cerebral hemisphere, in the ventral forebrain. This nucleus is a major component of the ventral striatum, and it is located between the putamen and the caudate nucleus.
The exact functions of the nucleus accumens are yet to be determined fully; however, it plays a crucial role in the reward system, due to its presence in the mesolimbic dopamine pathway.

Brain-Stem

The brain-stem is the posterior stalk-like part of the brain that connects the cerebrum with the spinal cord. It is composed by three main parts, the midbrain, the pons and the mdeulla oblongata.
The brain-stem is responsible for many vital functions such as breathing, blood pressure, sleeping, heart rate and consciousness.

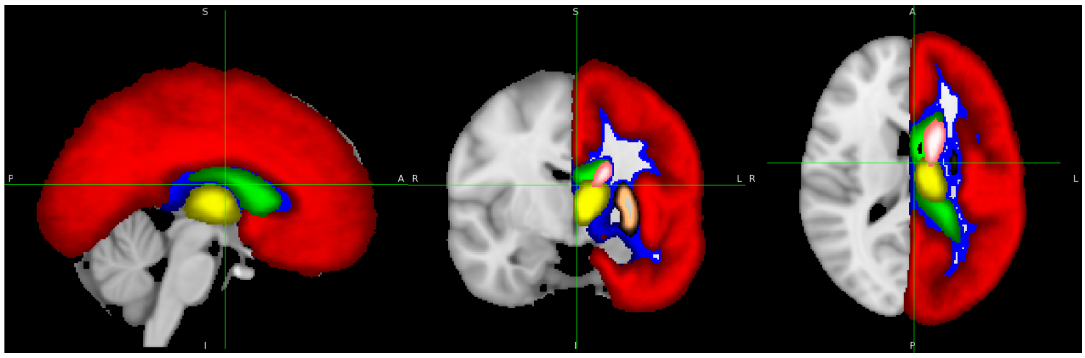

Figure 2.10: Left brain subcortical regions from the Harvard-Oxford atlas. We can distinguish the Cerebral WM (blue), the Cerebral Cortex (red), the Lateral Ventricle (green), the Thalamus (yellow), the Caudate (pink) and the Putamen (copper).

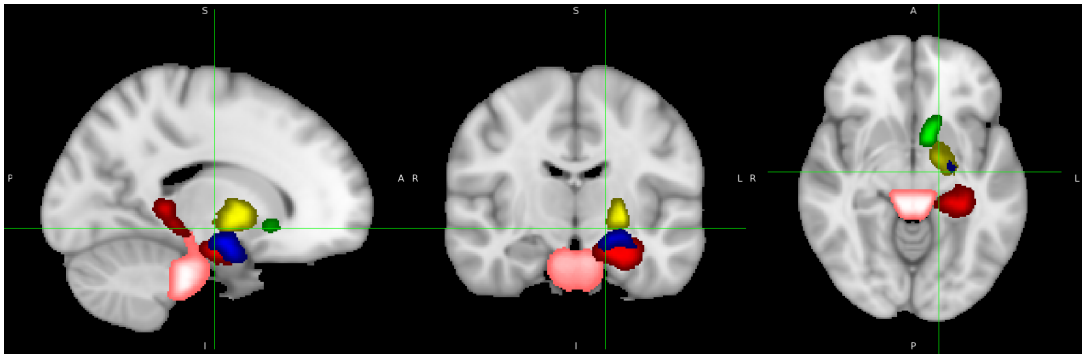

Figure 2.11: Left brain subcortical regions from the Harvard-Oxford atlas. We can distinguish the Pallidum (yellow), the Brain-Stem (pink), the Hippocampus (red), the Amygdala (blue) and the Accumbens (green).

Chapter 3

Materials and Methods

3.1 Data collection

3.1.1 ADNI: Alzheimer's Disease Neuroimaging Initiative

All the data used in this analysis has been collected from the ADNI database.
ADNI (Alzheimer's Disease Neuroimaging Initiative) is a multisite study that aims to improve clinical trials for the prevention and treatment of Alzheimer's disease. Launched in 2004 as a public-private partnership led by the National Institute on Aging (NIA), the National Institute of Biomedial Imaging and Bioengineering (NIBIB) and the FDA, it is a long-term study whose aim is to track the progression of Alzheimer's disease and other forms of cognitive decline using neuroimaging, clinical assessments, genetics and other biomarkers.

ADNI collects and analyzes data from individuals who are cognitively normal (CN), have mild cognitive impairment (MCI), or have been diagnosed with Alzheimer's disease (AD). For reference, MCI participants have reported a subjective memory concern either autonomously or via and informant or clinician; however, daily living activities are essentially preserved, there are no significant levels of impairment in other cognitive domains, and no signs of dementia exist. ADNI studies uses various neuroimaging techniques such as MRI, PET (Positron Emission Tomography) and others, to study changes in the brain structure and microstructure over time. The study started in 2004 with the ADNI-1 research, which was renewed in 2011 and 2016 with the ADNI-2 and ADNI-3 studies, respectively. Each phase of the study added new participants: each one of them is followed and reassessed over time to track the pathology of the disease as it progresses. The common strategy is based on the concept that AD can be characterized by the accumulation of $A\beta$ and phosphorylated τ, synaptic loss and neurodegeneration that leads to a decline in cognition. Results are then shared by ADNI through the USC Laboratory of Neuro Imaging's Image and Data Archive (IDA).

The phase study that will be considered for the further analysis is the ADNI-3, which began on August 1, 2016, and is a 5-year renewal of the previous study, ADNI-2. The major goal of ADNI-3 is to directly improve clinical trials, and it exploits several ways to achieve this result [Weiner et al., 2017].
Firstly, it studies the use of tau PET for subject selection, as a baseline covariate and a potential surrogate outcome measure. Moreover, it investigates other signals (e.g., change in CSF biomarkers) and functional imaging techniques (FDG-PET) and task-free functional MRI that may detect treatments effects in phase 2 trials. In addition, the initiative will confront the existing issues surrounding the inconsistent categorization of $A\beta$ and τ by standardizing various amyloid PET tracers in the "Centiloid project". Furthermore, it aims to enhance the dependability of CSF analysis for $A\beta$ and τ by introdicing novel immunoassay platforms and mass spectrometry techniques. Additionally, it seeks to evaluate the effectiveness of CSF synaptic protein biomarkers, such as neurogranin [Kang et al., 2015]. Finally, in conjunction with the Brain Health Registry (BHR) it implements web-based methods for characterization of subjects to overcome the problems of slow recruitment and high trial costs.

3.1.2 ADNI-3 study design

The participants pool is composed in the following way:

- 135-500 Normal Controls (new) + 295-330 Normal Controls (rollover from ADNI-2, approx.)
- 150-515 Mild Cognitive Impairment (new) + 275-320 Mild Cognitive Impairment (rollover from ADNI-2, approx.)
- 85-185 Mild Alzheimer's Dementia (AD) (new) + 130-150 Mild Alzherimer's Dementia (AD) (rollover from ADNI-2, approx.)

All patients are of ages between 55 and 90, and undergo a series of initial tests that are repeated at intervals over subsequent years, including a clinical evaluation, neuropsychological tests, genetic testing, lumbar puncture, and MRI and PET scans.

3.1.3 Acquisition Protocol

MRI data constitutes a fundamental aspect of the extensive dataset gathered from participants involved in ADNI. Since its inception in 2004, ADNI has undergone three distinct phases. Over the course of these phases, the MRI protocol has undergone refinement. During ADNI-1 (2004-2009), the MRI protocol primarily emphasized longitudinal structural imaging on 1.5T scanners, employing T1- and dual-echo T2-weighted sequences.

Figure 3.1: Specifics for each ADNI phase study.

Additionally, approximately one-fourth of ADNI-1 subjects underwent scanning using a nearly identical protocol on 3T scanners.
During ADNI-GO/ADNI-2 (2010-2016), imaging procedures transitioned to 3T scanners, maintaining T1-weighted imaging parameters akin to those in ADNI-1. In lieu of the dual-echo T2-weighted image utilized in ADNI-1, both 2D FLAIR and T2*-weighted imaging were introduced at all sites. Each imaging session incorporated both fully sampled and accelerated T1-weighted images. Additionally, the inclusion of advanced imaging techniques varied based on scanner manufacturer: diffusion imaging was conducted on GE scanners, resting-state functional MRI on Philips scanners, and arterial spin labeling on Siemens scanners.
In ADNI-3, imaging procedures are exclusively conducted on 3T scanners. The majority of imaging sequences utilized in ADNI-2 have been revised and incorporated into ADNI-3. Notably, each of the "advanced imaging" sequences from ADNI-2 is now part of the "basic" ADNI-3 protocol, with few exceptions across sites due to sequence license considerations.

Both images and quantitative numeric ADNI MR data are publicly available, and all data is accessible and downloadable via the Image Data Archive. In particular, for ADNI-3, the MRI Human Scan Protocol is the following:

1. 3 Plane Scout
2. Sagittal 3D Accelerated MPRAGE/IRSPGR
3. Sagittal 3D FLAIR
4. Axial T2 Star/GRE or Axial 3TE T2 Star/GRE
5. Axial 3D pCASL, Axial 3D PASL or Axial 2D PASL
6. Axial DTI or Axial MB (multi band) DTI
7. Axial Field Mapping Sequence
8. Axial fcMRI or Axial MB fcMRI
9. Accelerated High Resolution Hippocampus Scan

3.1.4 Dataset

The dataset to be analyzed is composed by a pool of subjects belonging to each one of the different categories cited above. In particular, the study group is composed by 10 AD, 18 MCI and 16 CN: for each patient, the relative MMSE and MoCa scores are provided.

A general overview about the dataset can be found in Table 3.1, while a full description of the patients parameters is listed in 6.1.

In particular, only subjects with DTI data acquired with a multi-shell High Angular Resolution Diffusion Imaging (HARDI) diffusion-weighted protocol were selected from the ADNI3 database to assess diffusion at high resolution and allow the modeling of water diffusivity in different compartments of the brain tissue. Specifically, the data was acquired at 3T (SIEMENS Magnetom Prisma Fit Scanner) using a 2D single-shot Echo Planar Imaging (EPI) sequence characterized by the following parameters: repetition time/echo time (TR/TE) = 3400/71; flip angle (a) = 90°; acquisition matrix = 256×256; with 2-mm isotropic voxel, no slice gap; 81 continuous axial oblique slices; number of averages = 1, acceleration factor = 2; total acquisition time 7min:10s. The diffusion-weighting protocol followed this design: 114 diffusion-encoding directions with b = 0 s/mm^2 (n = 13), b = 500 s/mm^2 (n = 6), b = 1000 s/mm^2 (n = 48), and b = 2000 s/mm^2 (n = 60), all with a posterior-anterior (PA) phase-encoding direction.
Accelerated sagittal T1-weighted anatomical images were acquired using a 3D Magnetization Prepared Rapid Acquisition Gradient Echo (MPRAGE) sequence: 208 continuous sagittal slices with 1-mm isotropic voxel, no slice gap; TR/TE = 2300/2.95; inversion time (IT) = 900ms; flip angle (a) = 9°; acquisition matrix = 208×208; in-plane acceleration factor = 2. [Gunter et al., 2017].

MMSE and MoCa Scores

MMSE Score and MoCa Score are two different screening tools for detecting cognitive impairment.
The Mini-Mental State Examination (MMSE) is used to screen for cognitive impairment and to estimate the impairment severity at a given point in time, and, if repeated in time, it allows to follow the course of cognitive changes in a in individual [Mitchell, 2009]. It consists of a maximum score of 30 points and evaluated different areas of cognitive functions such as time and space orientation, attention, language and memory. Based on the obtained score, an individual is categorized as follows:

- 24-30: No cognitive impairment
- 18-23: Mild cognitive impairment
- 0-17: Severe cognitive impairment

Anyway, the MMSE has some limitations, since it may not be equally valid across different cultural or educational backgrounds. Additionally, it is not sensitive enough to detect mild cognitive impairment or changes over very short periods of time, and it is not robust to detect false positive/negatives.

Group	Age range	MMSE (mean value)	MoCa (mean value)
AD	59-86	23.67	16.00
MCI	68-89	27.20	21.07
CN	53-85	28.44	25.25

Table 3.1: General overview of the study group.

To overcome such limitations, the Montreal Cognitive Assessment (MoCa) has been proposed [Nasreddine et al., 2005] as a substitute tool for evaluate different types of cognitive abilities, including attention, concentration, executive functions, memory, language, visuocontructional skills, conceptual thinking, calculations and orientation. Similar to the MMSE, it is used to detect MCI and early stages of AD, but it has been proven more sensitive than the former in detecting MCI.
It is also composed of 30 points and covers several cognitive domains, a grater range than the ones covered by MMSE. A score of 26 or above is considered normal, while scores below 26 may indicate some kind of cognitive impairment.

3.2 Analysis software

As mentioned earlier, the focus of this thesis will be on analyzing both healthy individuals and patients affected by Alzheimer's disease. To leverage and showcase the reproducibility of published works, several platforms have released application-specific toolboxes for particular MC-model implementations. Some well-known examples of these toolboxes comprehend MRtrix's works aimed at fiber tractography [Tournier et al., 2012] and Dipy's wide variety of dMRI-based signal models [Garyfallidis et al., 2014].

3.2.1 The Dmipy toolbox: Diffusion Microstructure Imaging in Python

Although these toolboxes are very good, the purpose of this thesis is the comparison between different analysis models, so it is useful to have a toolbox that allows us to manage them all. The Dmipy toolbox was proposed to solve exactly this issue [Fick et al., 2019b]. Dmipy is an open-source software solution developed to reproduce several MC-models in few lines of code. The main idea behind this toolbox is that one can view different formulations biophysical models as "building blocks", which can thus be assembled various combinations, and whose meaning changes from one application to another. Dmipy is available freely under open-source MIT license at [Fick et al., 2019a], where detailed tu-

torials and step-by-step implementations of many MC-models in literature are provided in the form of Jupyter Notebooks.

The sequence used to obtain DWIs images, and thus to probe the tissue microstructure with Dmipy, is the standard Pulsed Gradient Spin-Echo sequence (PSGE). In particular, an important remark for this study, is that measuring the PSGE signal at multiple acquisition parameter combinations allow us to gain insight on different tissue properties: in our case, with multi-shell acquisitions the signal contribution of multiple tissue compartments and axon orientation dispersion can be retrieved.
To allow Dmipy to interact with any PSGE acquisition scheme, the DmipyAcquisitionScheme module takes the raw PSGE parameters and prepares them for signal generation. It can be instantiated in three different ways, but for clinical data (as in this case), it is standard to use b-values $[s^2/m]$ and gradient directions (and optionally $\delta/\Delta/TE$ $[s]$).

To obtain information on the tissue microstructure and its properties, Dmipy relies on MC-models (Figure 3.3). This class of models represents the tissues as a linear combination of single compartment models, each one representing the diffusion signal from a specific tissue type. The different models of tissue microstructure depicted in Figure 3.3 are all based on histological observations of the various tissues. In particular, the recover of the microstructure information is done by finding the model parameters $\boldsymbol{p}$ that minimize the difference between modeled and the measured signal. The process of MC-modeling any model containing $i \geq 1$ compartments is thus given by:

$$\boldsymbol{p}^*(\boldsymbol{x}) = \text{argmin}_{\boldsymbol{p}} \int \left[E(\boldsymbol{x}, \boldsymbol{A}) - \hat{E}^{MC}(\boldsymbol{A}, \boldsymbol{p}) \right]^2 d\boldsymbol{A}, \tag{3.1}$$

with

$$\hat{E}^{MC}(\boldsymbol{A}, \boldsymbol{p}) = \sum_{i}^{N} f_i C_i(\boldsymbol{A}, \boldsymbol{p}_i) \tag{3.2}$$

where the parameters of each model $\boldsymbol{p}_i$ represent its tissue microstructure properties such as diffusivity, orientation, dispersion, axon diameter and so on, and f_i are the non-negative and normalized volume fractions that are used to weight the signal contribution of each compartment model.

3.2.2 Dmipy MC-models implementations

There is a significant distinction in the used models, depending on the microscopic or macroscopic scale.
All the different microscopic compartment models are based on the histological observations of the various tissues and structures. For example, to represent axons, cylinders of some diameter are used, while spheres are used to represent tumor cells. Dmipy allows

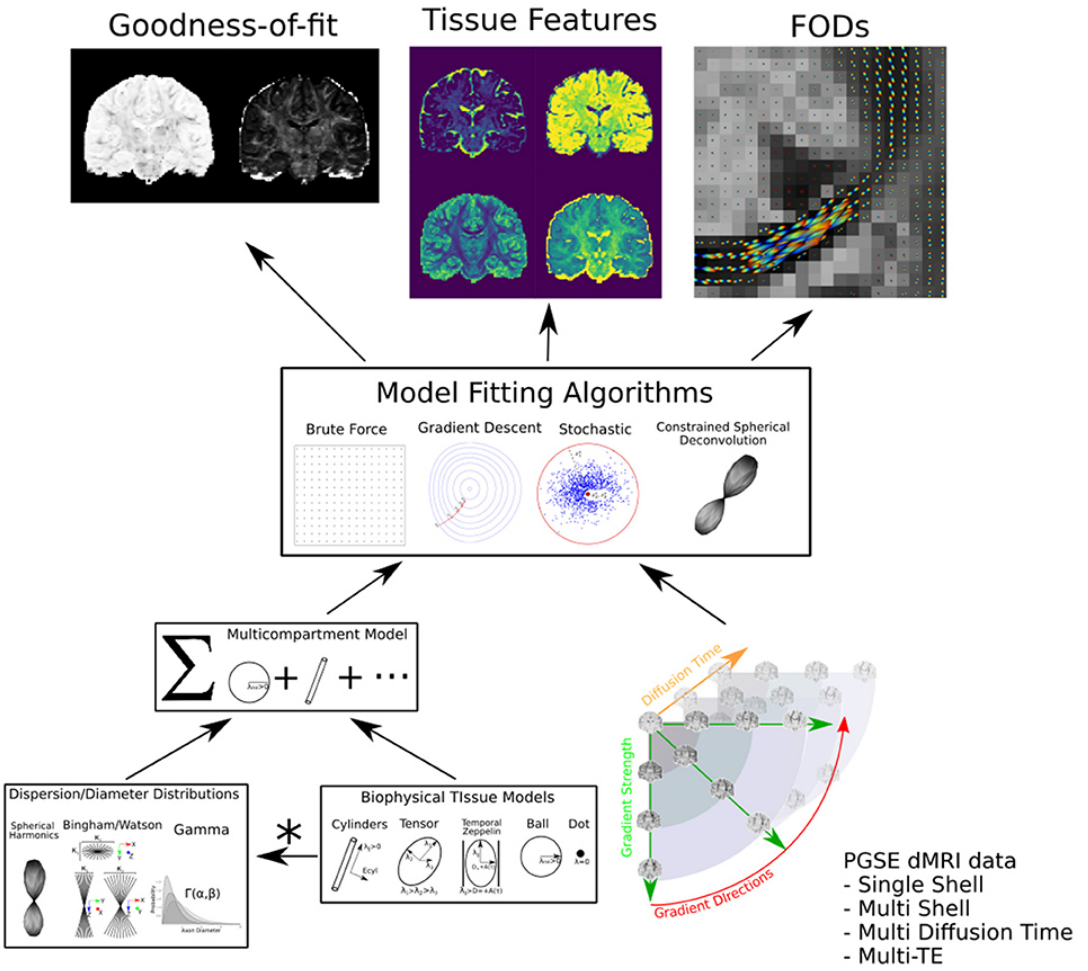

Figure 3.2: Dmipy workflow: different biophysical tissue models are dispersed and/or distributed and combined into a multi-compartment model, which is then fit to diffusion data to estimate tissue feature parameters and to reconstruct the FODs, while also quantifying the quality of fitting [Fick et al., 2019b].

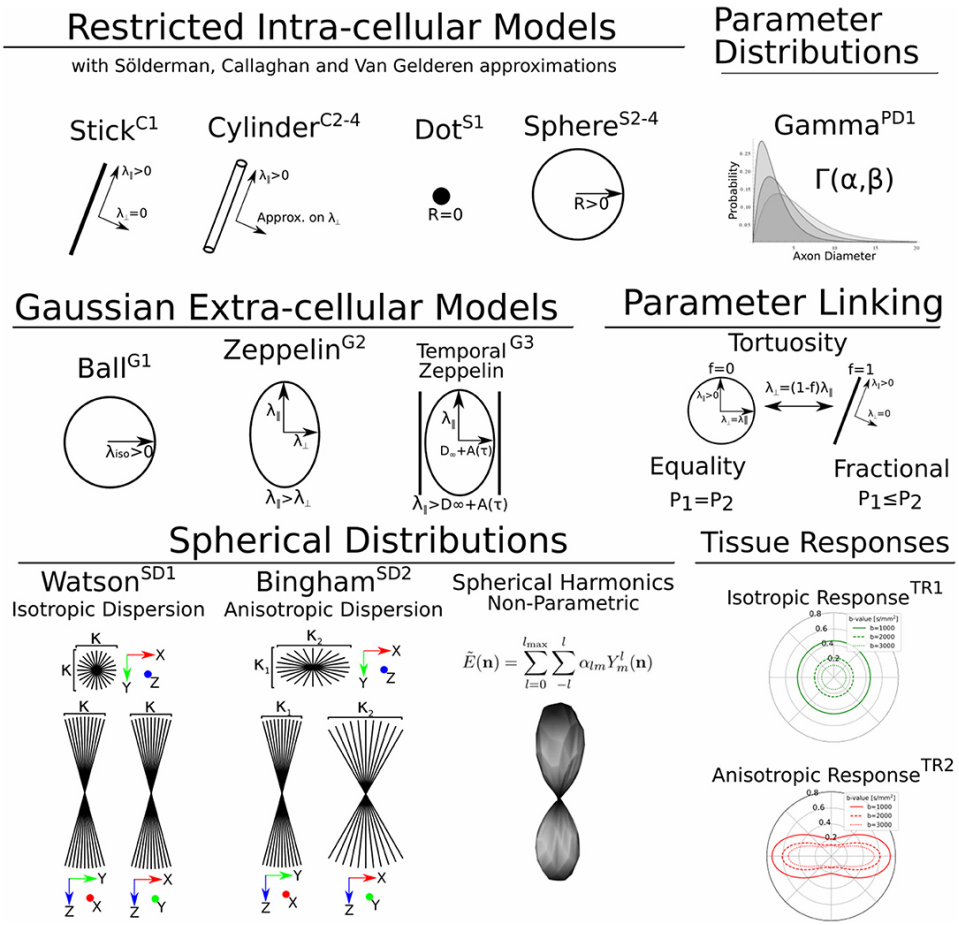

Figure 3.3: Overview of most biophysical models that are used in PSGE-based microstructure imaging. Dmipy assembles its models with different combinations of these "components" [Fick et al., 2019b].

modular signal generation for any microscopic model, and among the various ones are included the Gaussian (G) and restricted models such as Cylinders (C) and Spheres (S). The NODDI-Watson and NODDI-Bingham rely on some of these microscopic compartment models (along with additional macroscopic distributed models which will be explained later), and these are here briefly described:

- **G1**: This is the simplest Gaussian model, the Ball. It is represented by an isotropic Gaussian compartment whose signal attenuation only depends on isotropic diffusivity λ_{iso}. This model is often used to represent the diffusion signal of free water or of tissue types that on average induce an isotropic hindrance, such as gray matter.

- **G2**: This model, also known as *Zeppelin*, is an axially symmetric Gaussian distribution, aligned along orientation $\boldsymbol{\mu}$, having parallel and perpendicular diffusivity $\lambda_{\parallel} \geq \lambda_{\perp}$. Zeppelin usually represent the diffusion signal originating from the oriented, extra-axonal space.

- **C1**: The simplest Cylinder model assumes a diameter that is negligible and thus that can be set to zero: this results in the Stick model.

Apart from the microscopic compartment models discussed above, NODDI-Watson and NODDI-Bingham also rely on some macroscopic distributed models. In particular, these include features that are given by properties of groups of microstructural features, such as the distribution of axon diameter [Assaf et al., 2008] and axon orientation [Kaden et al., 2007]. Dmipy offers two different kinds of DistributedModels, the "ParameterDistributed" (PD) model for one-dimensional distribution, and the "SphericalDistributed" (SD) model for parametric distributions of models on the sphere (e.g., axon dispersion). For our purposes we are going to focus only on the latter.
Spherical distributed models (SD) apply parametric distributions of over model orientation. In this case, the signal attenuation is obtained by means of a spherical convolution of spherical distribution $F(\boldsymbol{n};\boldsymbol{\Omega}) : \mathbb{S}^2 \to [0,\infty]$ with parameters $\boldsymbol{\Omega}$, with one or more convolution kernel models $C_i^K(\boldsymbol{n},\tilde{\boldsymbol{p}}_{\boldsymbol{i}}) = C(\boldsymbol{n},\tilde{\boldsymbol{p}}_{\boldsymbol{i}}|\boldsymbol{\mu}_i = [0,0,1])$, meaning $\tilde{\boldsymbol{p}}_{\boldsymbol{i}}, \boldsymbol{\mu_i} \in \boldsymbol{p_i}$ and the orientation $\boldsymbol{\mu_i}$ is parallel to the z-axis. Thus, the mathematical expression for an SD model is given by

$$\begin{aligned} C_{SD}(\boldsymbol{A_s},\boldsymbol{n};\{\tilde{\boldsymbol{p}}_{\boldsymbol{i}}\},\boldsymbol{\Omega}) &= \int_{\mathbb{S}^2} F(\boldsymbol{n}-\boldsymbol{u};\boldsymbol{\Omega}) \cdot \sum_{i=1}^{N} f_i C_i^K(\boldsymbol{A_s},\boldsymbol{u};\tilde{\boldsymbol{p}}_{\boldsymbol{i}}) d\boldsymbol{u} \\ &= \left[F(\boldsymbol{\Omega}) *_{\mathbb{S}^2} \sum_{i=1}^{N} f_i C_i^K(\boldsymbol{A_s};\tilde{\boldsymbol{p}}_{\boldsymbol{i}})(\boldsymbol{n}) \right] \end{aligned} \tag{3.3}$$

where f_i are the normalized volume fractions weighting the signal contribution of each convolution kernel, $\boldsymbol{A_s}$ is the shell-wise acquisition parameters and $\boldsymbol{u} \in \mathbb{S}^2$ is the integrated orientation variable.

SD-models can be regarded as a subset of the MC-model framework, and they can be integrated with various other compartment models. Similar to PD models, SD models eliminate the orientation parameters of the input models while introducing parameters for the spherical distribution. Additionally, they have the flexibility to stack and apply multiple distributions to the parameters of input models. An important distinction for this analysis is given by the two different kinds of SD distributions:

- **SD1**: The Watson distribution, which is defined as an isotropic Gaussian distribution on the sphere with orientation $\boldsymbol{\mu}$ and concentration parameter κ. As depicted in [Zhang et al., 2012], Dmipy uses the orientation dispersion index (ODI) as an optimization parameter, defining $ODI = 0$ as a spike function along the principal direction $\boldsymbol{\mu}$, and $ODI = 1$ as an isotropically dispersed profile on the sphere.
- **SD2**: The Bingham distribution, which is defined as an anisotropic Gaussian distribution of the sphere with orientation $\boldsymbol{\mu}$ and primary and secondary concentration parameters κ_1 and κ_2. As described in [Tariq et al., 2016], Dmipy uses the ODI in an analogous way as the SD1, and β instead of the concentrations. The Bingham has an additional ψ parameter whose purpose is to rotate the distribution about $\boldsymbol{\mu}$.

Fitting MC models

The way to handle MC models is to treat them as non-convex optimization problems. The optimization algorithm used in this analysis is the standard "brute2fine" one: it exploits brute force optimization by sampling all optimized parameters $\mathbf{p}$ on an equi-spaced grid of N_s samples between each parameter's minimum and maximum optimization bounds.

3.2.3 NODDI-Watson

The Dmipy toolbox proposes several model to estimate important microstructural brain parameters. They provided examples of code for each fitting model, such as the NODDI-Watson.
As previously stated, NODDI-Watson models the dispersion of neurites for a single axon bundle by using a Watson distribution, $W(\kappa, \boldsymbol{\mu})$. It is important to notice that this distribution is a particular case of the Bingham distribution when $\kappa = \kappa_1 = \kappa_2$: because of this, it may not model appropriately axon bending or fanning. The mathematical model considers separately the CSF, restricted and hindered diffusion as a Gaussian Ball (**G1**), Stick (**C1**) and Zeppelin (**G2**) model. The signal for the NODDI-Watson is therefore modeled as

$$E^{\text{NODDI}}_{\text{Watson}} = \underbrace{f_{CSF}\overbrace{E_{iso}(\cdot|\lambda_{CSF})}^{\text{Ball}}}_{\text{CSF}} + \overbrace{W(\kappa, \boldsymbol{\mu})}^{\text{Watson}} *_{\mathbb{S}^2} \left[\underbrace{f_h \overbrace{E_h(\cdot|\lambda_\perp^{tort}, \lambda_\parallel)}^{\text{Zeppelin}}}_{\text{Hindered Extra-Axonal}} + \underbrace{f_r \overbrace{E_r(\cdot|\lambda_\parallel)}^{\text{Stick}}}_{\text{Intra-Axonal}} \right] \tag{3.4}$$

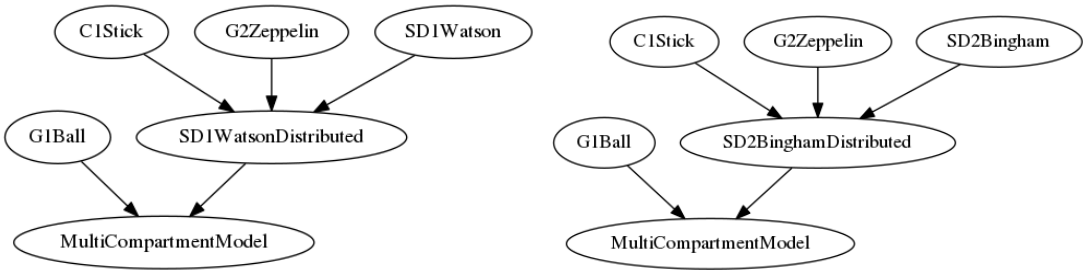

Figure 3.4: Model setup for the NODDI-Watson and NODDI-Bingham, respectively.

Some of the parameters of the previous equation are fixed or subject to constraints, in order to improve the stability of the estimated model parameters. In particular:

- the isotropic diffusivity λ_{CSF} is set equal to $3 \cdot 10^{-9}\ m^2/s$
- the parallel diffusivities $\lambda_{\parallel}$ of the Stick and Zeppelin are the same and set equal to $1.7 \cdot 10^{-9}\ m^2/s$
- the perpendicular diffusivity $\lambda_{\perp}^{tort}$, the intra- and extra- axonal volume fraction f_r, f_h and the parallel diffusivity $\lambda_{\parallel}$ are all linked via a tortuosity model.

The parameters that are extrapolated from the data are the Watson distribution parameters $\kappa, \boldsymbol{\mu}$ and the volume fractions f_{CSF}, f_h and f_r.
In particular, the code extracts the following values:

- SD1WatsonDistributed_1_partial_volume_0
- SD1WatsonDistributed_1_mu
- SD1WatsonDistributed_1_odi
- partial_volume_0
- partial_volume_1
- Watson_MSE
- Watson_NDI

These values are calculated and mapped to each voxel of the brain scan, ultimately resulting in quantitative three-dimensional map of the brain. An example of the outputs can be found in Chapter 4.1.

3.2.4 NODDI-Bingham

The Dmipy toolbox also provides an example of code for the NODDI-Bingham model: it differs from the NODDI-Watson just by the distribution incorporated inside the model. The signal is modeled as

$$E^{\text{NODDI}}_{\text{Bingham}} = \underbrace{f_{CSF}\overbrace{E_{iso}(\cdot|D_{CSF})}^{\text{Ball}}}_{\text{CSF}} + \overbrace{B(\kappa_1, \kappa_2, \boldsymbol{\mu_i})}^{\text{Bingham}} *_{\mathbb{S}^2} \left[\underbrace{f_h \overbrace{E_h(\cdot|\lambda_\perp^{tort}, \lambda_\parallel)}^{\text{Zeppelin}}}_{\text{Hindered Extra-Axonal}} + \underbrace{f_r \overbrace{E_r(\cdot|\lambda_\parallel)}^{\text{Stick}}}_{\text{Intra-Axonal}} \right] \tag{3.5}$$

This model is more suited than the NODDI-Watson for complex fiber configurations, as it is designed to better capture the anisotropy of the fiber's dispersion with respect to the principal direction. However, it does not address any of the other limitations of NODDI-Watson, as it too struggles with dealing with crossing fibers.
The setup of the model is essentially the same as the previous case, except for calling a Bingham instead of a Watson distribution.
Again, the code extracts the following parameters from the analysis:

- SD2BinghamDistributed_1_partial_volume_0
- SD2BinghamDistributed_1_beta_fraction
- SD2BinghamDistributed_1_mu
- SD2BinghamDistributed_1_odi
- SD2BinghamDistributed_1_psi
- partial_volume_0
- partial_volume_1
- Bingham_MSE
- Bingham_NDI

As for the NODDI-Watson, these values are mapped to a three-dimensional map of the brain, whose example can be found in Chapter 4.1.

3.3 Image analysis with FSL

In order to perform a meaningful statistical analysis, an intermediate step is required. The tool designed for this operation is FSL (FMRIB Software Library) [Smith et al., 2004], that is a comprehensive suite of tools used for analyzing and processing brain imaging

data, particularly functional magnetic resonance imagine (fMRI), structural MRI and diffusion tensor imaging (DTI) data. Developed by the Oxford Centre for Functional MRI of the Brain (FMRIB) at the University of Oxford, FSL in widely used in the field of neuroimaging research.
Key features of FSL include:

1. **Preprocessing tools**: Includes functions for motion correction, slice timing correction, and brain extraction;
2. **Statistical analysis**: Tools for performing statistical analysis of fMRI data, including General Linear Model (GLM) analysis;
3. **Structural analysis**: Tools for segmentation, registration and voxel-based morphometry of structural MRI data;
4. **DTI analysis**: Tools for preprocessing, fitting diffusion tensors, and performing tractography on diffusion MRI data;
5. **Connectivity analysis**: Tools for analyzing brain connectivity using resting-state fMRI data or DTI data.

FSL is available as a free, open-source software package and is compatible with various operating systems, including Linux, macOS and Windows. It includes a graphical user interface (GUI) as well as command-line tools.

3.3.1 Registration to a common space

Registration is a crucial step in neuroimaging statistical analysis for several reasons. In particular, the ones that are relevant to this study are the following:

- **Alignment Across Subjects**: In group studies, brain images from multiple subjects need to be aligned to a common reference space (such as the MNI or Talairach standard brain). This alignment allows for comparison across individuals, as it ensures that the same anatomical structures correspond to the same locations in the images of different subjects;
- **Region of Interest (ROI) Analysis**: Accurate registration ensures that regions of interest are consistently located across subjects and sessions. This consistency is vital for ROI-based analyses, where specific brain regions are the focus of the study;
- **Improved Statistical Power**: By reducing variability due to anatomical differences, registration enhances the ability to detect significant effects in the data. This improvement increases the statistical power of the analyses, making it easier to identify true brain-behavior relationships or treatment effects.

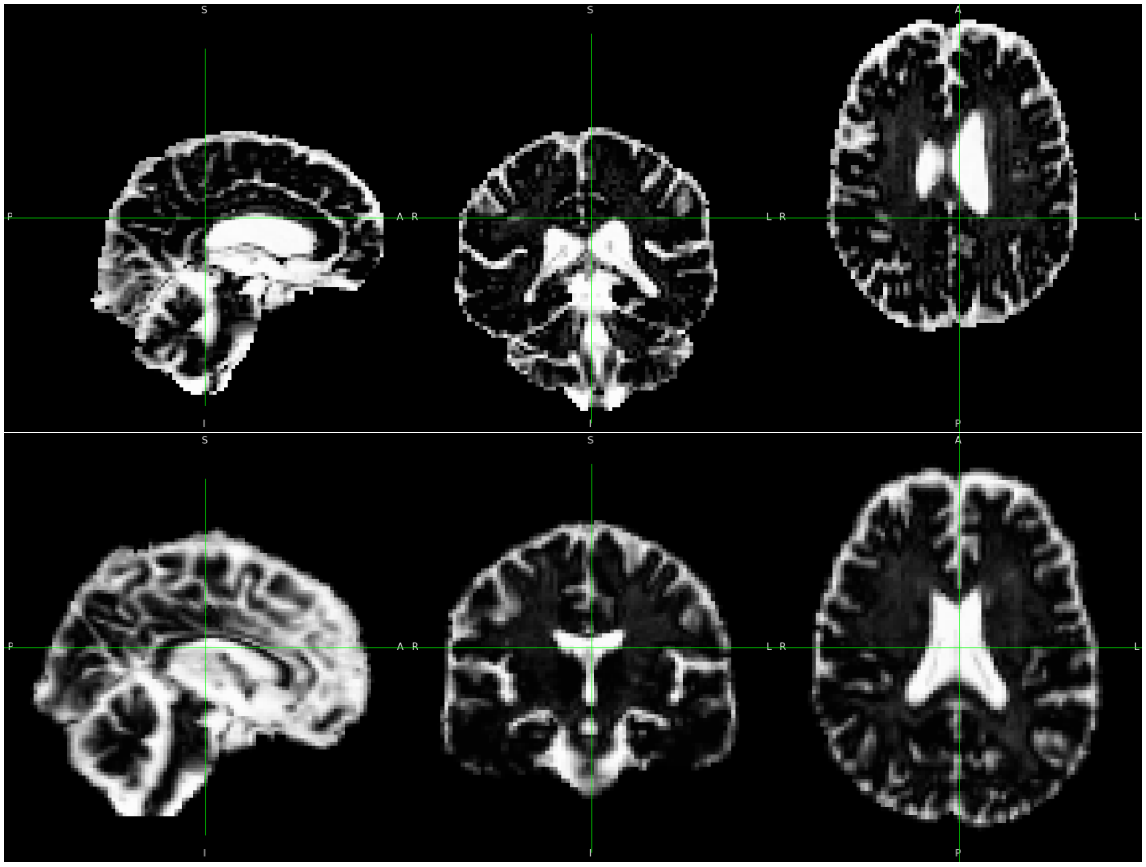

Figure 3.5: One of NODDI-Bingham metrics, partial_volume_0, before (top) and after (bottom) the registration to MNI.

The parameters extracted by NODDI must hence be registered to a reference space, and the designed one is the Montreal Neurological Institute (MNI) (see Figure 3.5). The MNI space is a standardized coordinate system obtained by averaging 152 different brain scans. In particular, it provides a standard anatomical framework that facilitates the comparison of brain images across different studies and research groups.
Additionally, registering individual brain images to the MNI template allows for comparative analysis across subjects and populations. It ensures that corresponding brain regions are aligned, which is essential for group-level analyses and studies involving multiple subjects.
Moreover, many neuroimaging atlases and brain region parcellations are defined in MNI space. Hence, registering to MNI space enables the use of these atlases for region-of-interest (ROI) analysis, labeling and interpreting the results.
Finally, it must be taken into account that the MNI template is an average brain template that represents common anatomical features. Hence, registering individual brains

to this template helps in reducing anatomical variability, leading to improved alignment and more precise localization of brain structures. In addition, using a common space for registration such as the MNI allows results to be obtained which are fully reproducible by subsequent analysis.

Steps involved in Registration to MNI Space

1. **Preprocessing**: Initial preprocessing steps such as motion correction, slice timing correction, and brain extraction are performed on the raw images.

2. **Affine Registration**: An affine transformation is applied to align the individual brain to the MNI template. This transformation includes scaling, rotation, and translation to account for differences in brain size, orientation, and position.

3. **Nonlinear Registration**: After affine registration, a nonlinear transformation is applied to further align the anatomical details of the brain to the MNI template. This step accounts for more complex differences in brain shape and structure.

4. **Resampling**: The brain image is resampled into the MNI space using the transformation parameters obtained from the registration steps. This resampling ensures that the image voxels are aligned with the MNI coordinate system.

5. **Verification**: The registered image is visually inspected to ensure accurate alignment with the MNI template. Misregistrations, if any, are corrected.

The FSL package provides tools for registration to MNI space, such as FLIRT (FMRIB's Linear Image Registration Tool) for affine registration [Jenkinson et al., 2002, Jenkinson and Smith, 2001] and FNIRT (FMRIB's Nonlinear Image Registration) for nonlinear registration [Andersson et al., 2007].

3.3.2 Definition of ROIs and results extraction

As mentioned earlier, the the analysis will concentrate on several different areas of the brain. In order to define these regions of interest (ROIs), we will exploit the Template and Atlases included with FSL. In particular, the Altas used is the Harvard-Oxford subcortical structural atlas, a probabilistic atlas covering 21 subcortical structural areas, derived from structural data and segmentations provided by the Harvard Center for Morphometric Analysis.
The brain areas listed in 2.6.2 are hence downloaded from FSL. Subsequently, a binary operation is performed in order to obtain the masks used to extract the results from our maps. Additionally, these masks are eroded by a pixel to ensure a cleaner region after the extraction operation.
The masks obtained in this way are then applied to the maps provided by the two NODDI

fits (listed in 3.2.3 and 3.2.4), and the relative ROIs are then extracted by using the -mas command on FSLMaths (a general image calculator on FSL). Finally, for each one of these ROIs, the mean value and the standard deviation are calculated via FSLStats.
A chart summarizing the FSL analysis workflow can be found in Figure 3.6.

3.4 Theoretical foundations for statistical analysis

The last step of the work pipeline is the statistical analysis of the obtained results. This section will lay the foundations of the statistical methods used later in the analysis, as explained in detail in Chapter 4.

Shapiro-Wilk test

The Shapiro-Wilk test is a statistical test used to determine whether a sample comes from a normally distributed population. Firstly, a null hypothesis H_0 is formulated (i.e., the sample comes from a normally distributed population). Then, given a sample of size n, the sample data is sorted in ascending order, $x_{(1)}, x_{(2)}, ..., x_{(n)}$, and the expected values for a standard normal distribution are calculated, $m_{(1)}, m_{(2)}, ..., m_{(n)}$.
The test statistic W is calculated according to the formula:

$$W = \frac{\left(\sum_{i=1}^{n} a_i x_{(i)}\right)^2}{\sum_{i=1}^{n}(x_i - \bar{x})^2} \tag{3.6}$$

where $x_{(i)}$ are the ordered sample values, $\bar{x}$ is the sample mean and the coefficients a_i are calculated based on the expected values m_i and the covariance matrix of these expected values.
The test statistic W measured how well the sample matches a normal distribution, hence a value close to 1 indicates that the sample data likely comes indeed from a normal distribution. Finally, the p-valued is obtained from the distribution of W under the null hypothesis. As always, having set the significance level α to 0.05, a p-value smaller than α means that the sample does not come from a normally distributed population, and that the null hypothesis must be rejected.

Levene's test

Levene's test is a statistical procedure used to assess the homogeneity of variances for a variable calculated for two or more groups. Firstly, a null hypothesis H_0 is formulated (i.e., the variances are equal across groups). Then, for each observation, the absolute deviation from the group mean is calculated:

$$Z_{ij} = |Y_{ij} - \bar{Y}_i| \tag{3.7}$$

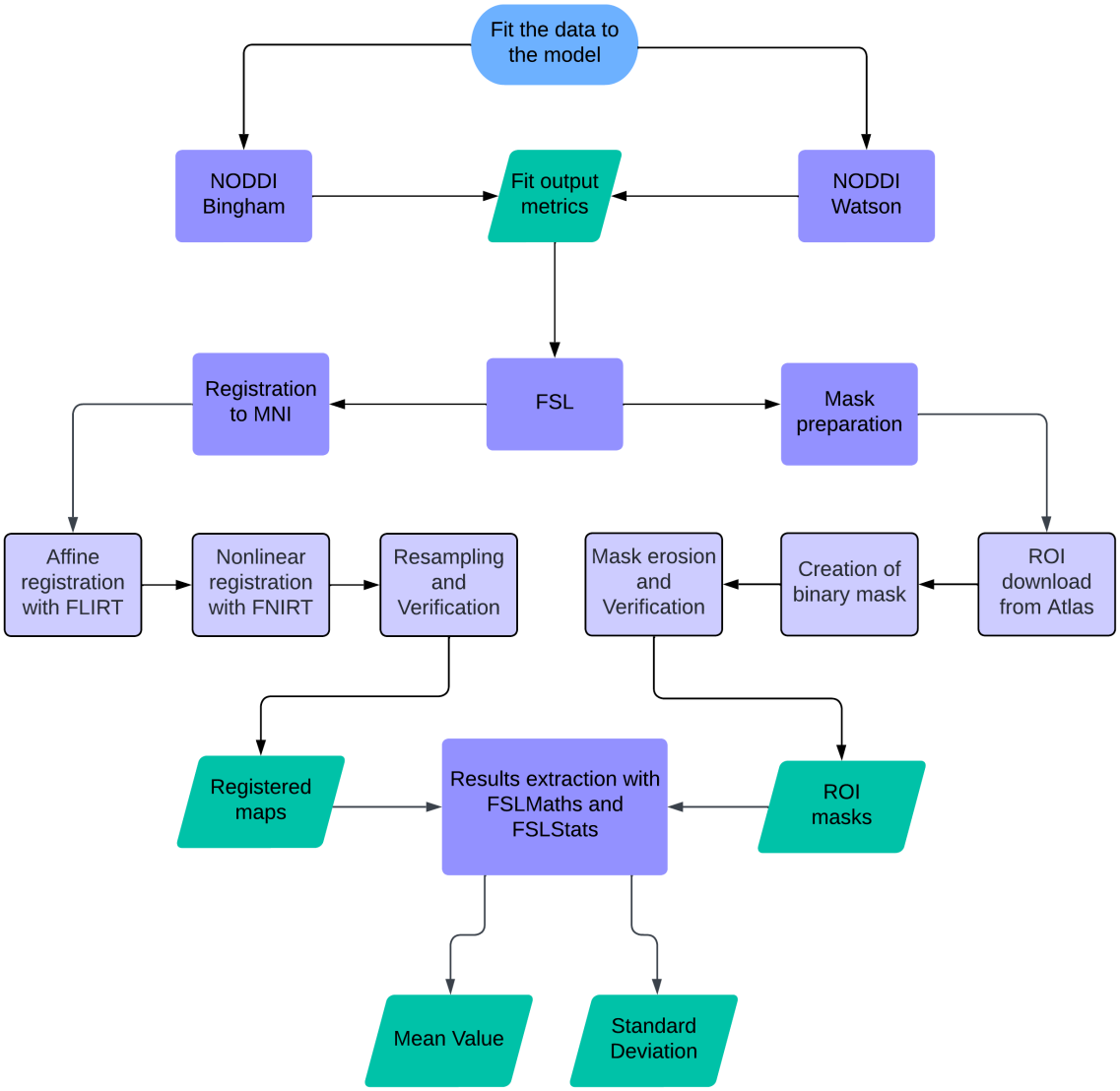

Figure 3.6: FSL image analysis workflow.

where Y_{ij} is the j-th observation in the i-th group, and $\bar{Y}_i$ is the me an (or median) of the i-th group.
To calculate the test statistic, Z_{ij} is treated as the response variable, and an analysis of variance (ANOVA) is performed on the transformed values:

$$Z_{ij} = \mu + \tau_i + \epsilon_{ij} \tag{3.8}$$

where μ is the overall mean of the transformed values, τ_i represents the effect of the i-th group and ϵ_{ij} is the error rate. Finally, the ANOVA F-statistic is calculated based on the between-group variance and the within-group variance of the transformed values Z_{ij}. The p-value of the test is obtained by comparing the computed F-statistic to the F-distribution with the appropriate DOFs. As before, having set the significance level α to 0.05, a p-value smaller than α means that there is a significant difference in the variances among groups, and that the null hypothesis must be rejected.
The Levene's test is widely used as a preliminary check before performing ANOVA or other parametric tests that assume homogeneity of variances.

Three-way factor ANOVA

A three-way ANOVA test is a statistical method used to determine the influence of three independent categorical variables (factors) on a continuous dependent variable, and at the same time studying the interactions effects between the factors. The assumptions of this kind of test are that each factor (i.e. each independent categorical variable) has different levels or categories, and that the variable (a continuous one) is influenced by the factors and their interactions. Moreover, the test assumes independence of observations, normality of residuals and homogeneity of variances (the last two can be proved with the previously described tests).
A three-way ANOVA test has three main objectives: the first is to determine whether there are significant differences in the dependent variable across the levels of each factor, independently. The second goal is to determine whether the effect of one factor depends on the levels of another factor, and finally the third goal is to investigate the interaction effect between the three factors simultaneously.
The model can be represented as:

$$Y_{ijkl} = \mu + A_i + B_j + C_k + (A \cdot B)_{ij} + (A \cdot C)_{ik} + (B \cdot C)_{jk} + (A \cdot B \cdot C)_{ijk} + \epsilon_{ijkl} \tag{3.9}$$

where Y_{ijkl} is the dependent variable, μ is the overall mean, A_i, B_j, C_k are the main effects of Factors A, B and C, respectively, $(A \cdot B)_{ij}, (A \cdot C)_{ik}, (B \cdot C)_{jk}$ are the two-way interaction effects, $(A \cdot B \cdot C)_{ijk}$ is the three-way interaction effect and ϵ_{ijkl} is the error term.
Once all the assumptions are checked, the ANOVA table is built to summarize the sources of variance, including the sum of squares, degrees of freedom, mean squares, F-values

and p-values for each main effect and interaction.
If significant main effects are found, than the associated factor has a significant effect on the dependent variable. Moreover, if significant interaction effects are found, than the effect of one factor depends on the level of another factor. Overall, if significant effects are found, post-hoc tests can be performed to assess which specific levels of the factors differ.

Post hoc test: Tukey's Honest Significant Difference (HSD)

A post hoc test is a statistical analysis that is performed subsequently to an ANOVA to determine which specific group means deviate significantly from each other. Since ANOVA can detect significant effects but does not specifies which group mean differs, post hoc tests have to be used for a better understanding of the underlying relations between groups. Moreover, post hoc tests help control the overall Type I error rate, that is the probability to reject incorrectly a true null hypothesis, while making multiple pairwise comparisons.
Tukey's HSD test is only one of the several types of post hoc tests that exists, each one of them having a different approach to controlling the error rate.
To perform Tukey's HSD test we start by calculating the mean value $\bar{X}_i$ for each group i. Then, the MSE is obtained by the ANOVA table as the ratio between the within-group sum of squares and the within-group degrees of freedom.
The critical value q is obtained from the studentized rage distribution (the q distribution) based on the number of groups (k) and the within-group degrees of freedom. The Honest Significant Difference is calculated according to the formula

$$HSD = q \cdot \sqrt{\frac{MSE}{n}} \tag{3.10}$$

where n is the number of observations per group. Finally, for each pair of groups i and j, the absolute difference between the group means is calculated; if $|\bar{X}_i - \bar{X}_j| > HSD$ then there is a statistically significant difference between the means.

Once the Tukey p-values are obtained, it is helpful to apply the Benjamini-Hochberg (BH) procedure to control the false discovery rate (FDR). The p-values are ordered in ascending order and for each of them a threshold value is calculated according to

$$\frac{i}{m} \cdot \alpha \tag{3.11}$$

where i is the position of the ordered p-value, m is the total number of comparisons and α is the significance level (usually set at 0.05). Then, the largest p-value $p_{(k)}$ is found such that

$$p_{(k)} \leq \frac{k}{m} \cdot \alpha \tag{3.12}$$

Finally, all null hypotheses corresponding to values smaller than $p_{(k)}$ are rejected.

Chapter 4

Data Analysis and Results

4.1 NODDI fit results

In this section an example of the metrics obtained from the NODDI-Bingham fit and NODDI-Watson fit is presented. To highlight the differences and the similarities between the two models, each Figure is composed by the same metric, obtained with NODDI-Bingham, on the left side, and NODDI-Watson, on the right side (except, obviously, for the beta_fraction metric of the NODDI-Bingham).

Figure 4.1 shows the normalized volume fraction of the Stick within the Bingham/Watson bundle, respectively, which essentially represents the proportion of the diffusion signal attributed to a particular fiber orientation within each voxel. The grayscale in the image reflects the degree of alignment or anisotropy of white matter fibers in the brain, with brighter areas indicating stronger, more organized fiber tracts and darker areas indicating less organized or isotropic regions. For example, the bright, central region in Figure 4.1 corresponds to the corpus callosum: this major white matter tract typically exhibits high anisotropy and is represented by an almost white region, as expected.

Figure 4.2 shows the ODI map. Regions with a lighter grayscale have a higher ODI value, meaning the fiber orientations within these voxels are more dispersed. On the contrary, regions with a darker grayscale have a lower ODI value, indicating that the fiber orientations are more tightly clustered or aligned in a single predominant direction. In fact, the peripheral areas, which are darker, likely correspond to regions where fibers are more organized, such as within more aligned white matter tracts running parallel. As one can notice, the map obtained by the NODDI-Bingham model is overall darker with respect to the one obtained by the NODDI-Watson, reflecting a higher ability to detect the fibers anisotropy.

Figures 4.3 and 4.4 show the fraction of the Ball (CSF) and the Bingham/Watson bundle, respectively. In Figure 4.3, brighter areas correspond to regions with a higher fraction of CSF: in the brain, this would typically include areas like the ventricles, which are filled with fluid (as one can notice in the two images). Darker areas, on the other hand, indicate regions with a lower CSF fraction. On the contrary, Figure 4.4 shows as white the regions with a higher fraction of WM, where the two distributions accurately model the fiber orientations. As one can expect, the maps provided by the two partial volumes are, in some way, one the negative version of the other.

Figure 4.5 represents the maps of the mean squared error. The maps are consistent across both methods and reflect the MSE values which are very low across the whole brain, except for the edge of the brain scan. This implies that the discrepancies between the models' predictions and the actual diffusion signals are minimal, possibly because the chosen models might be a particularly appropriate fit for the dataset or thanks to the high-quality of the diffusion data, which led to better models fits, reducing the overall MSE. Again, as in Figure 4.2, the map obtained by the NODDI-Bingham model is darker, hence has smaller values, compared to the NODDI-Watson one, reflecting an overall lower MSE score and a better fit performance to the data.

Figure 4.6 shows the neurite density index, which estimates the density of axons and dendrites within a voxel, as opposed to extracellular space. Brighter regions indicate higher density of neurites, while darker areas correspond to lower neurite density, possibly indicating regions with more extracellular space or less dense WM tracts.

Finally, Figure 4.7 represents the fraction of the concentration of fibers around the primary orientation over the concentration around a secondary orientation, expressed by the beta_fraction, in the NODDI-Bingham model. A high ratio, corresponding to brighter areas in the image, indicates that fibers are more tightly clustered around a single dominant orientation, suggesting a strong, coherent fiber tract with minimal dispersion. On the contrary, darker areas mean a low ratio, indicating dispersed fibers, with less dominance of a single orientation. This might occur in regions of crossing fibers or complex fiber architecture.

By comparing the two different images in each of the described Figures, it can be noticed that the two analyzed models are visually very similar in their results, as one would expect.

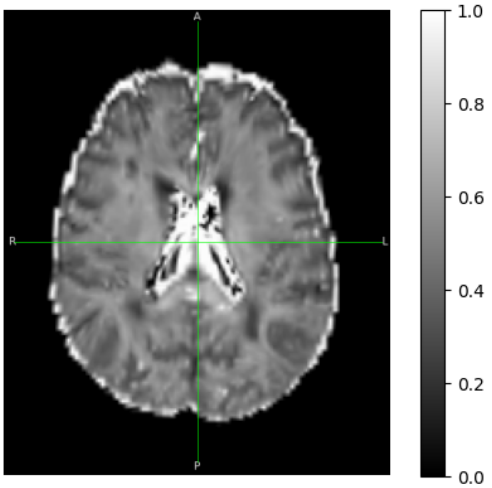

(a) SD2BinghamDistributed_1_partial_volume_0.

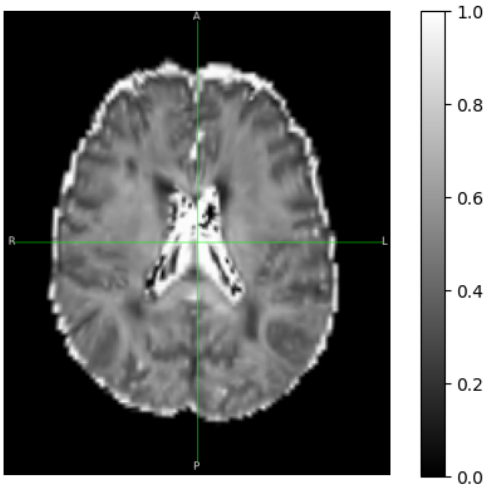

(b) SD1WatsonDistributed_1_partial_volume_0.

Figure 4.1

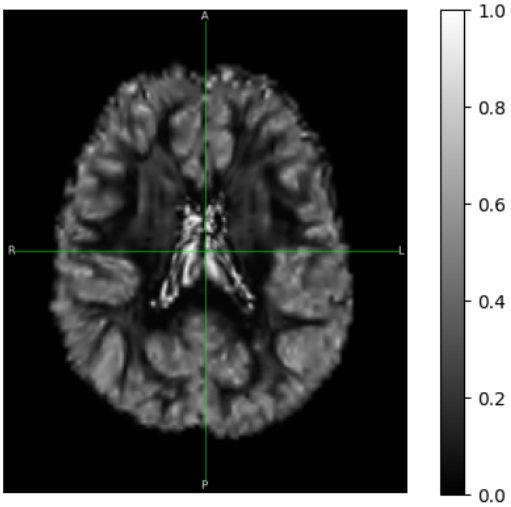

(a) SD2BinghamDistributed_1_odi.

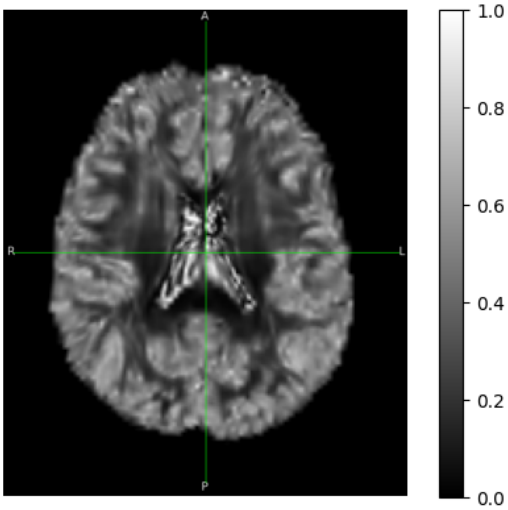

(b) SD1WatsonDistributed_1_odi.

Figure 4.2

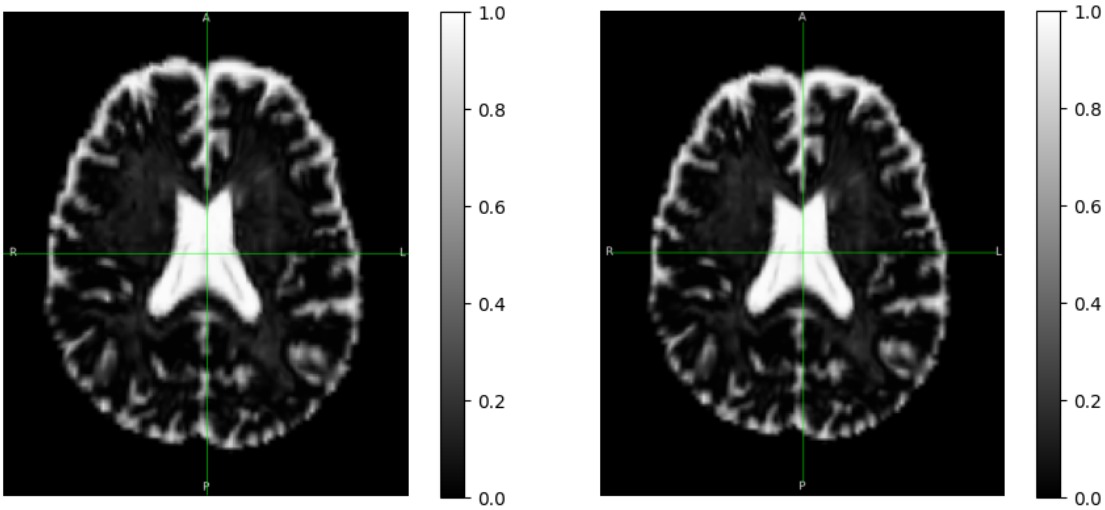

(a) Bingham: partial_volume_0. (b) Watson: partial_volume_0.

Figure 4.3

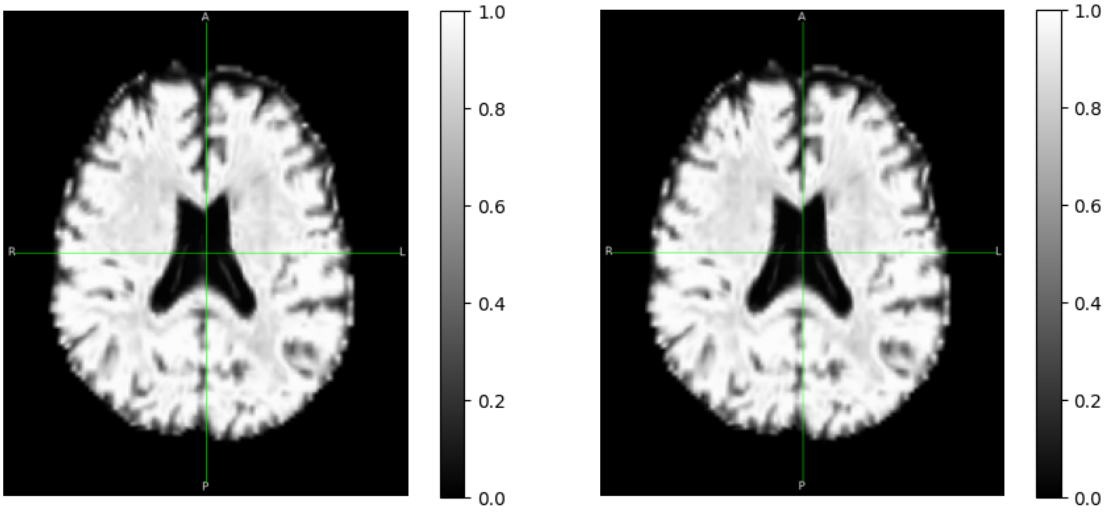

(a) Bingham: partial_volume_1. (b) Watson: partial_volume_1.

Figure 4.4

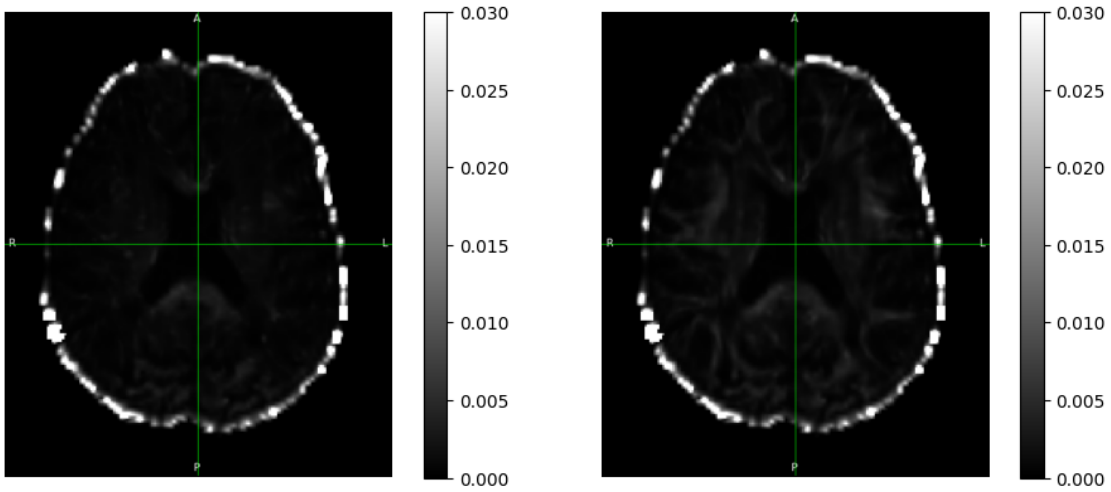

(a) Bingham_MSE. (b) Watson_MSE.

Figure 4.5

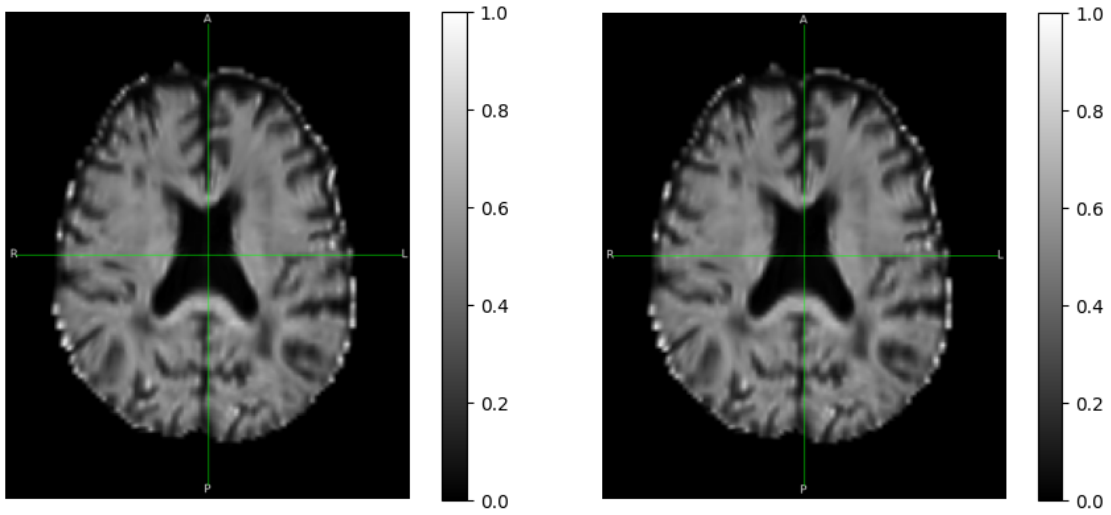

(a) Bingham_NDI. (b) Watson_NDI.

Figure 4.6

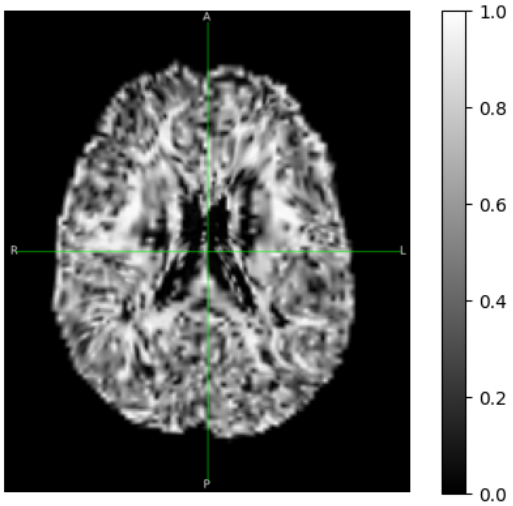

(a) SD2BinghamDistributed_1_beta_fraction.

Figure 4.7

4.2 Statistical Data Analysis

The obtained results are analyzed to find statistical information about the ability of the two different fits in underlying the brain regions in exam.

4.2.1 χ^2 test for gender distribution across groups

Firstly, the distribution of the subject's gender throughout the several study groups is checked via a χ^2 test. The subjects information about gender can be found in Chapter 6.1.
The test yielded the following result:

χ^2 statistic	0.01704
p-value	0.9915
DOF	2

Since the significance level α is set equal to 0.05, and the p-value is greater than α, we fail to reject the null hypothesis and conclude that there is no significant association between gender and group membership.

4.2.2 ANOVA test for age distribution across groups

To assert whether the age distribution is the same across all three groups, an ANOVA test is performed. The Analysis of Variance (ANOVA) test is a statistical formula that is used to compare variances across the means (or average) of different groups. In this scenario it is used to determine if there is any difference between the means of our groups. An overview of the group's age range is shown in Table 4.1, while a more detailed description of the patient's age can be found in Chapter 6.1.

Group	Age range
AD	59-86
MCI	68-89
CN	53-85

Table 4.1: Study groups age range overview.

The test yielded the following result:

F statistic	0.2232
p-value	0.8009

Since the significance level α is set equal to 0.05, and the p-value is greater than α, we fail to reject the null hypothesis and conclude that there is no significant difference in age distribution between the groups.

4.2.3 Group analysis

The subsequent step is the group analysis, in which the fit parameters are compared keeping into account the different subcortical regions and the study group. The group analysis is a fundamental step to understand how the belonging to a specific group or a particular brain region can affect the fit parameters.
Firstly, a selection of the parameters was performed. Only those meaningful to the group analysis are kept and are listed below:

- For the NODDI-Bingham:
  - partial_volume_1: the fraction of the Bingham bundle (WM)
  - SD2BinghamDistributed_1_partial_volume_0: normalized volume fraction of the Stick within the Bingham bundle

  - SD2BinghamDistributed_1_beta_fraction: the concentration parameter, κ_1/κ_2
  - SD2BinghamDistributed_1_odi: the orientation dispersion index

- For the NODDI-Watson:
  - partial_volume_1: the fraction of the Watson bundle (WM)
  - SD1WatsonDistributed_1_partial_volume_0: normalized volume fraction of the Stick within the Watson bundle
  - SD1WatsonDistributed_1_odi: the orientation dispersion index

Shapiro-Wilks and Levene's results

Shapiro-Wilks test and Levene's test are performed on the data, to ensure for normality and homogeneity of the variances of the distributions of the parameters.
Both for the NODDI-Bingham and the NODDI-Watson, the parameter distribution is tested for normality in relation to the groups and observation regions. The Shapiro-Wilks test is performed on the data, and it can be noticed that some of the obtained p-values are smaller than the significant level α. This might be related to the small size of the samples, hence it can be concluded that the samples come indeed from a normally distributed population. All the results for the Shapiro-Wilks test relative to NODDI-Bingham and NODDI-Watson are listed in Chapter 6.4.
Levene's test was performed on the data to assess the homogeneity of variances. The test results on the two datasets (Bingham and Watson) are listed in Tables 4.2 and 4.3. Since all p-values are all greater than the chosen significance level α (0.05), it can be concluded that the variances are homogeneous along the samples.

Parameter	**Statistic**	**p-value**
partial_volume_1	1.613	0.1999
beta_fraction	1.804	0.1652
partial_volume_0	0.4784	0.6199
ODI	0.3697	0.6910

Table 4.2: Levene's test results for the NODDI-Bingham data.

Three-way ANOVA results

Having assessed the normality and homogeneity of variance for the dataset, a three-way ANOVA is performed to determine how the belonging to a peculiar group, the observation region or the region's hemisphere influence the parameters. For each one of the parameter, the test was conducted considering as factors "Group", "Region" and

Parameter	Statistic	p-value
partial_volume_1	1.622	0.1981
ODI	0.8688	0.4198
partial_volume_0	0.4105	0.6634

Table 4.3: Levene's test results for the NODDI-Watson data.

"Hemisphere". By considering these factors singularly, it is possible to study the main effects on the parameters: a p-value smaller than α indicates that the factor has impact on the parameter. Additionally, the factors are combined to study the interaction effects, i.e. if the impact of one factor on the mean depends on the level of another factor. The results obtained from the test are reported in tables 4.4, 4.5, 4.6, 4.7, 4.8, 4.9 and 4.10.

	SSQ	df	F	p-value
Group	0.3473	2	17.37	**<1.0E-05**
Region	33.60	9	373.6	**<1.0E-05**
Hemisphere	1.436E-04	1	1.436E-02	0.9046
Group:Region	0.3377	18	1.877	**1.479E-02**
Group:Hemisphere	1.835E-02	2	0.9179	0.3998
Region:Hemisphere	3.501E-02	9	0.3892	0.9406
Group:Region:Hemisphere	6.701E-02	18	0.3725	0.9921
Residual	8.196	820		

Table 4.4: 3-way ANOVA results for NODDI-Bingham: partial_volume_1.

By looking at the results is is possible to make some considerations.

- the p-value associated with the "Region" factor is the lowest and consistently smaller than α across all tests: this strongly suggests a significant dependence of the mean values on the brain observation region.
- the p-value associated with the "Group" factor is also considerably lower than the significance level across all tests: this too suggests a strong dependence of the mean values on the patients group (AD, MCI and CN).
- the p-value associated with the "Hemisphere" factor is higher than the fixed significance level (0.05) across all tests: this suggests that the mean values are not influenced by the hemisphere in which the region is located.

	SSQ	df	F	p-value
Group	3.436E-02	2	5.239	**5.487E-03**
Region	9.730	9	329.7	**<1.0E-05**
Hemisphere	6.341E-03	1	1.934	0.1647
Group:Region	4.946E-02	18	0.8379	0.6558
Group:Hemisphere	4.524E-03	2	0.6898	0.5020
Region:Hemisphere	2.462E-02	9	0.8342	0.5847
Group:Region:Hemisphere	2.891E-02	18	0.4897	0.9630
Residual	2.689	820		

Table 4.5: 3-way ANOVA results for NODDI-Bingham: beta_fraction.

	SSQ	df	F	p-value
Group	5.857E-02	2	7.485	**6.007E-04**
Region	3.364	9	95.54	**<1.0E-05**
Hemisphere	1.501E-02	1	3.835	5.052E-02
Group:Region	0.2218	18	3.150	**1.128E-05**
Group:Hemisphere	9.898E-05	2	1.265E-02	0.9874
Region:Hemisphere	1.450E-02	9	0.4119	0.9292
Group:Region:Hemisphere	8.558E-03	18	0.1215	0.9999
Residual	3.208	820		

Table 4.6: 3-way ANOVA results for NODDI-Bingham: partial_volume_0.

	SSQ	df	F	p-value
Group	6.252E-02	2	14.24	**<1.0E-05**
Region	1.292	9	65.37	**<1.0E-05**
Hemisphere	2.979E-05	1	1.357E-02	0.9073
Group:Region	0.1103	18	2.791	**9.839E-05**
Group:Hemisphere	6.214E-04	2	0.1415	0.8681
Region:Hemisphere	1.918E-02	9	0.9705	0.4630
Group:Region:Hemisphere	2.843E-03	18	7.194E-02	0.9999
Residual	1.801	820		

Table 4.7: 3-way ANOVA results for NODDI-Bingham: ODI.

	SSQ	df	F	p-value
Group	0.3440	2	17.16	**<1.0E-05**
Region	33.62	9	372.7	**<1.0E-05**
Hemisphere	2.502E-04	1	2.496E-02	0.8745
Group:Region	0.3448	18	1.911	**1.248E-02**
Group:Hemisphere	1.863E-02	2	0.9292	0.3953
Region:Hemisphere	3.679E-02	9	0.4078	0.9313
Group:Region:Hemisphere	6.779E-02	18	0.3757	0.9917
Residual	8.218	820		

Table 4.8: 3-way ANOVA results for NODDI-Watson: partial_volume_1.

	SSQ	df	F	p-value
Group	6.309E-02	2	13.44	**<1.0E-05**
Region	1.555	9	73.60	**<1.0E-05**
Hemisphere	2.372E-04	1	0.1010	0.7507
Group:Region	0.1357	18	3.211	**<1.0E-05**
Group:Hemisphere	1.593E-03	2	0.3392	0.7124
Region:Hemisphere	2.577E-02	9	1.220	0.2792
Group:Region:Hemisphere	3.912E-03	18	9.258E-02	0.9999
Residual	1.925	820		

Table 4.9: 3-way ANOVA results for NODDI-Watson: ODI.

	SSQ	df	F	p-value
Group	5.973E-02	2	7.615	**5.286E-04**
Region	3.290	9	93.22	**<1.0E-05**
Hemisphere	1.247E-02	1	3.181	7.487E-02
Group:Region	0.2195	18	3.110	**1.437E-05**
Group:Hemisphere	1.243E-04	2	1.585E-02	0.9843
Region:Hemisphere	1.513E-02	9	0.4285	0.9201
Group:Region:Hemisphere	7.509E-03	18	0.1064	0.9999
Residual	3.216	820		

Table 4.10: 3-way ANOVA results for NODDI-Watson: partial_volume_0.

- the p-value associated with the "Group:Region" combined factors is also smaller than α throughout all tests except the one relative to the beta_fraction. This suggests that there is an interaction between the patient groups and the observation regions relatively to the analyzed parameters.
- all the p-values associated to the combined factors featuring the "Hemisphere" are instead higher than the significance level. This suggests that the "Hemisphere" factor plays a marginal role in influencing the behavior of the mean values in relation to the other factors.

Given all these considerations, it is useful, in order to remove the division between left and right hemisphere, to combine the relative mean and standard deviation values and perform again the analysis, to ensure a better understanding of the underlying interactions between the patients group and the observation region.

Tukey's results

The ANOVA test is then performed again after the parameter values are merged without the "Hemisphere" distinction. Since the results are significant, a Tukey's HSD test is used to compare all possible pair of means in order to find statistically significant results and understand which specific groups differ from each other. Additionally, a Benjamini-Hochberg procedure is applied to adjust the p-values from the Tukey test to control for the False Discovery Rate (FDR).
The data is hence grouped and the differences of every one of the fit parameters are studied between groups and for each region. For the sake of simplicity, here only the significant results are reported in Tables 4.11 and 4.12, while the complete results can be found in Appendix.

Parameter	**Region**	**Comparison**	**p-value**	**p-value (BH)**
beta_fraction	Cortex	CN vs MCI	0.0107	0.0321
ODI	Cortex	AD vs CN	0.0017	0.0051
ODI	Cortex	AD vs MCI	0.0147	0.0221
ODI	Putamen	AD vs CN	0.0031	0.0093
partial_volume_0	Cerebral WM	AD vs CN	0.0018	0.0054
partial_volume_0	Pallidum	AD vs CN	0.0023	0.0069
partial_volume_1	Cortex	AD vs CN	0.0091	0.0174
partial_volume_1	Cortex	CN vs MCI	0.0116	0.0174
partial_volume_1	Hippocampus	AD vs CN	0.0122	0.0366

Table 4.11: Significant results of the Tukey's test for the NODDI-Bingham (for the complete results please refer to the Appendix). The last column indicates the adjusted p-value after the Benjamini-Hochberg procedure.

Parameter	Region	Comparison	p-value	p-value (BH)
ODI	Cortex	AD vs CN	0.0037	0.0111
ODI	Putamen	AD vs CN	0.0054	0.0162
partial_volume_0	Cerebral WM	AD vs CN	0.0021	0.0063
partial_volume_0	Pallidum	AD vs CN	0.0025	0.0075
partial_volume_1	Cortex	AD vs CN	0.009	0.0174
partial_volume_1	Cortex	CN vs MCI	0.0116	0.0174
partial_volume_1	Hippocampus	AD vs CN	0.0129	0.0387

Table 4.12: Significant results of the Tukey's test for the NODDI-Watson (for the complete results please refer to the Appendix). The last column indicates the adjusted p-value after the Benjamini-Hochberg procedure.

4.2.4 Correlation analysis

Finally, for a better understanding of the underlying relations between the assessment of the disease and the significant parameters obtained by the analysis, it is useful to perform a Pearson's correlation analysis between the fit parameters and the MMSE and MoCa Scores.

Pearson's correlation analysis

The parameters which showed significant results in the previous tests (i.e. the ones reported in Tables 4.11 and 4.12) underwent a Pearson's correlation analysis to assess the relationship between the parameter values and the MMSE/MoCa scores of the study group. The primary goal of the test is to determine whether the categorization of the patient (AD, MCI or CN) is reflected in the fit parameters.
The correlation test was performed by testing each pair of significant parameter values against the MMSE/MoCa scores for the relative patients. The test results are provided in Tables 4.13 and 4.14, while the scatter plots relative to each one of the tested pairs can be found in Appendix 6.4. For a detailed analysis of the results, please refer to Chapter 5.2.

	MMSE		MoCa	
	Pearson's corr.	p-value	Pearson's corr.	p-value
beta_fraction in Cortex	-0.2129	0.1871	-0.03086	0.8561
ODI in Cortex	0.3047	0.5592	0.4531	0.004861
ODI in Putamen	0.4007	0.01041	0.4375	0.006777
partial_volume_0 in WM	0.3743	0.01733	0.3642	0.02670
partial_volume_0 in Pallidum	0.2452	0.1273	0.3756	0.02199
partial_volume_1 in Cortex	0.2117	0.1898	0.3014	0.06989
partial_volume_1 in Hippocampus	0.4857	0.00149	0.3621	0.02765

Table 4.13: Significant results of correlation analysis: Pearson's correlation coefficients and relative p-values obtained by testing the NODDI-Bingham parameters against the MMSE and MoCa Scores.

	MMSE		MoCa	
	Pearson's corr.	p-value	Pearson's corr.	p-value
ODI in Cortex	0.2506	0.1188	0.4061	0.01264
ODI in Putamen	0.3335	0.03548	0.3761	0.02180
partial_volume_0 in WM	0.3773	0.01639	0.3607	0.02832
partial_volume_0 in Pallidum	0.2373	0.1403	0.3656	0.02607
partial_volume_1 in Cortex	0.2111	0.1909	0.3013	0.06994
partial_volume_1 in Hippocampus	0.4837	0.001567	0.3604	0.02842

Table 4.14: Significant results of correlation analysis: Pearson's correlation coefficients and relative p-values obtained by testing the NODDI-Watson parameters against the MMSE and MoCa Scores.

Chapter 5

Results' discussion and Conclusions

5.1 Tukey's Significance Test

The first part of the analysis consists in comparing the results of Tukey's test for the two fit models, NODDI-Bingham and NODDI-Watson, respectively. Already from a first glance at the results in Tables 4.11 and 4.12, it is clear that the brain parameters and regions with most significance are the same, regardless of the chosen model.
A more general analysis shows how for both models, several parameters show significant differences between the groups after adjusting for multiple comparisons using the Benjamini-Hochberg procedure. Moreover, both models show that the ODI evaluated in the Cortex region and in the Putamen region are significantly different when comparing the AD to the CN groups. This finding is also true for the parameter partial_volume_0 (the normalized volume fraction of the Stick) evaluated in the Cerebral White Matter region and in the Pallidum.
In more detail, it is possible to make some more precise considerations with regard to each of the two models under analysis.
For the NODDI-Bingham model, significant differences were found for beta_fraction in the Cortex between CN and MCI. Additionally, there are significant differences in ODI between AD and CN, AD and MCI in the Cortex, and AD and CN in the Putamen. Finally, there are also significant differences in partial_volume_0 and partial_volume_1 across various regions and comparisons.
For the NODDI-Watson model, significant differences were similar to NODDI-Bingham for ODI in the Cortex and Putamen regions, and for partial_volume_0 in the Cerebral White Matter and in the Pallidum. Moreover, significant differences were found in partial_volume_1 between AD and CN, and CN and MCI in the Cortex, and between AD and the CN in the Hippocampus.
Additionally, Tukey's test results for the NODDI-Bingham model show higher sensitivity in the distinction between AD and MCI, while the results for the NODDI-Watson model

highlight almost only the discrepancies between AD and CN, except for one case which deserves further investigation.

These findings suggest that there are measurable and significant differences in ODI and partial volume metrics in specific brain regions between different cognitive groups (AD, MCI and CN). The significant differences found between AD and CN in both models for several parameters imply that these metrics could potentially serve as biomarkers for distinguishing between Alzheimer's disease and normal cognition. Additionally, the significant results in the Cortex, Putamen, Cerebral White Matter, Pallidum and Hippocampus highlight these regions as important areas of interest in studying cognitive impairment and Alzheimer's disease.

5.2 Correlation between brain metrics and cognitive scores

As explained in Chapter 4.2.4, once the metrics that show significant results in the Tukey's test are found, a Pearson's correlation analysis is conducted between these fit parameters and the brain metrics known for each patient (MMSE and MoCa scores). Each analysis gave, for each parameter of the two models, a Pearson's correlation score and the relative p-value.
In the following paragraphs the results presented in Tables 4.13 and 4.14 will be discussed.

NODDI-Bingham Model

Based on the interpretation of the correlation value and the relative p-values, the correlation analysis against the MMSE score gave statistically significant results for the following parameters:

- ODI in the Putamen (moderate positive correlation)
- partial_volume_0 in the Cerebral White Matter (moderate positive correlation)
- partial_volume_1 in the Hippocampus (moderate positive correlation)

The same analysis against the MoCa score highlighted a greater number of statistically significant correlations instead:

- ODI in the Cortex (moderate positive correlation)
- ODI in the Putamen (moderate positive correlation)
- partial_volume_0 in the Cerebral White Matter (moderate positive correlation)

- partial_volume_0 in the Pallidum (moderate positive correlation)
- partial_volume_1 in the Hippocampus (moderate positive correlation)

The NODDI-Bingham model shows several significant correlations between brain metrics and cognitive scores. Notably, the ODI evaluated in the Putamen region correlates positively with both MMSE and MoCa scores, indicating that this region's microstructural integrity might be closely linked to cognitive function. The two metrics associated to partial volumes in WM and Hippocampus also show significant positive correlation with the cognitive scores, confirming that the WM and hippocampal integrity are crucial for cognitive health. Specifically, the hippocampus is particularly noteworthy, with a moderate and statistically significant correlation with MMSE (r=0.4857, p=0.00149) and MoCa (r=0.3621, p=0.02765). Given the Hippocampus' central role in memory and learning, these results underscore the Bingham model's sensitivity in detecting early cognitive decline associated with Alzheimer's.

NODDI-Watson Model

The same considerations can be made with regard to the correlation analysis between the parameters obtained by NODDI-Watson and the MMSE metric. The ones showing statistical significance are the following:

- ODI in the Putamen (moderate positive correlation)
- partial_volume_0 in the Cerebral White Matter (moderate positive correlation)
- partial_volume_1 in the Hippocampus (moderate positive correlation)

Once again, similarly to the NODDI-Bingham case, the same analysis against the MoCa score highlighted a greater number of statistically significant correlations:

- ODI in the Cortex (moderate positive correlation)
- ODI in the Putamen (moderate positive correlation)
- partial_volume_0 in the Cerebral White Matter (moderate positive correlation)
- partial_volume_0 in the Pallidum (moderate positive correlation)
- partial_volume_1 in the Hippocampus (moderate positive correlation)

The NODDI-Watson model also reveals significant correlations, though fewer and slightly weaker compared to the Bingham model. The partial_volume_1 metric in the Hippocampus again shows a strong correlation with MMSE (r=0.4837, p=0.001567), which is

consistent with the Bingham model, reinforcing the Hippocampus' importance in cognitive assessments.
But while the Watson model demonstrates similar trends, the correlations are generally weaker, suggesting that the NODDI-Watson model might be less sensitive in detecting subtle microstructural changes linked to cognitive impairment. The moderate correlations indicate that is can still be a useful tool for understanding brain microstructure, but its potential may be somewhat limited compared to the Bingham model.
Additionally, since there are multiple different correlations, it may be useful to perform more accurate and specific tests for AD functionalities and study these correlations is a greater population.

5.3 Interpreting the results from a clinical perspective

5.3.1 Statistically significant brain regions and their role in Alzheimer's Disease

It is reasonable and expected that the brain regions identified as statistically significant in this analysis would show a relationship with cognitive function and the progression of Alzheimer's disease, based on the known roles of these regions in brain function. In particular:

1. **Cortex (specifically ODI and partial_volume metrics)**
   It is known for its role in regulating higher-order brain functions, such as memory, cognition, attention, though and, additionally, it has been demonstrated that different regions of the cortex are involved in various aspects of cognitive progressing. Since Alzheimer's disease is characterized by the degeneration of cortical neurons, leading to cortical thinning, there are particular areas such as the entorhinal cortex which are likely to develop atrophy in AD. Moreover, the presence of amyloid plaques and neurofibrillary tangles in the cortex contributes to the cognitive decline observed in subjects affected by the disease.
   The significant correlations between ODI and partial_volume metrics in the cortex and cognitive scores align with the known impact of cortical degeneration on cognitive function in AD. Changes in ODI could reflect microstructural alterations due to neuron loss or changes in fiber orientation, which are expected in the progression of AD.

2. **Putamen (ODI)**
   It is known for being part of the basal ganglia and its involvement in motor control, learning, and particularly in various cognitive processes, including reinforcement

learning and habit formation. Additionally, it is involved in regulating the information flow in relation to coordination and cognitive processing.
Although the putamen is more traditionally associated with motor control, its role in cognitive functions becomes relevant in the context of AD, particularly as the disease progresses and other brain regions, including those in the basal ganglia, become affected. Changes in the putamen have been linked to neurodegenerative processes in AD, potentially reflecting disruptions in the frontostriatal circuits.
Significant correlations in the putamen suggest an association between microstructural changes and cognitive decline, consistent with the broader impact of AD on subcortical structures as the disease progresses.

3. **White Matter (partial_volume_0)**
   It is known that WM consists of myelinated axons whose role is to facilitate communications between different brain regions. Because of that, it plays a critical role in the efficient transmission of neuronal signals, which is fundamental for cognitive functions.
   Since AD is associated with WM degradation, which contributes to the disconnection between brain regions, this primary leads to cognitive decline. WM hyperintensities and changes in WM integrity are commonly observed in AD patients, reflecting the impact of the disease on brain connectivity.
   The significant correlations between WM metrics (partial_volume_0) and cognitive scores support the understanding that WM integrity is crucial for cognitive function and is compromised in AD.

4. **Hippocampus (partial_volume_1)**
   Its importance lies in its centrality to memory formation, spatial navigation and consolidation of information (short-term and long-term memory), and because of this it is one of the most studied regions in relation to cognitive functions, especially in the context of memory.
   Consequently, the hippocampus is one of the first regions to suffer damage in AD, leading to the characteristic memory loss and disorientation associated with the disease. Indeed, hippocampal atrophy is a hallmark of AD and is strongly correlated with the severity of cognitive decline.
   Because of this, the strong correlations found between hippocampal partial volume and cognitive scores underscore the critical role of the hippocampus in the progression of AD and the manifestation of cognitive impairments.

To summarize, the regions identified as significant in the analysis are not only relevant to cognitive function, but also align with the known progression of Alzheimer's disease. It is thus possible to state that the findings are reasonable and expected, adding validity to the results.

5.4 General findings on models performance

Both the NODDI-Bingham and the NODDI-Watson models demonstrate that specific brain metrics (e.g., ODI in Putamen, partial_volume_0 in Cerebral White Matter) are significantly correlated with cognitive scores (MMSE and MoCa), reinforcing the belief that these metrics can be used as potential biomarkers for cognitive impairment. When it comes to comparing the two models, the NODDI-Bingham model shows stronger and more significant correlations for ODI in Cortex with the MoCa score (0.4531), whereas the NODDI-Watson model shows consistent significance across both MMSE and MoCa scores for the same metric, though to a lesser extent.
However, although the results obtained by the two models may suggest that they are generally equivalent, the subtle differences found between the values produced by NODDI-Bingham and NODDI-Watson show a small but substantial discrepancy between the two. In fact, it seems that the NODDI-Bingham model may be slightly more sensitive in detecting correlations with cognitive scores in certain brain areas, such as the Putamen. In this region, the ODI value showed a strong correlation with both MMSE and MoCa scores for NODDI-Bingham (correlation values 0.4007 and 0.4375, respectively) while NODDI-Watson highlighted a dependency, even if not that strong (correlation values 0.3335 and 0.3761, respectively).

5.4.1 Comparison on models sensitivity

The analysis shows that both models used in this thesis work are able to highlight and are sensitive to the various states of disease progression. Nevertheless, the mathematical premises on which they are based differ slightly in that the Bingham distribution is a more flexible and sophisticated model for representing fiber orientation distribution in diffusion MRI. It accounts for anisotropic dispersion and can represent both unimodal and bimodal fiber orientations. This flexibility might allow for more accurate representation of complex fiber arrangements and potentially more sensitive detection of microstructural changes related to cognitive impairment.
On the contrary, the Watson distribution is simpler and less flexible than the Bingham, assuming a unimodal distribution of fiber orientations and isotropic dispersion. Although less computationally intensive, it may not reflect the comprehensiveness of the fiber arrangements as effectively as the Bingham distribution.

The NODDI-Bingham model showed significant correlations in regions and metrics where the NODDI-Watson model still showed a strong correlation, though to a lesser extent, such as "ODI in Cortex" with MoCa (p=0.004861 for Bingham vs. p=0.01264 for Watson). Additionally, the Bingham model identified a significant correlation for "beta_fraction in Cortex", which is a metric that is not evaluated in the Watson model, indicating the Bingham model's potential to uncover additional relevant metrics.

The Bingham model's flexibility in representing anisotropic and complex fiber configurations should hence provide a more detailed and accurate depiction on neural tissue microstrucure. This can lead to better detection of microstructural differences associated with cognitive impairment.

Practical implications

In the case where the models under consideration were intended to be used for clinical practice, where the main objective is to identify minimal microstructural changes associated with cognitive impairment, the NODDI-Bingham model might offer an advantage despite its increased computational demands.
Similarly, for research purposes, where detecting subtle changes is crucial, the Bingham model's higher sensitivity could provide more insights into the relationship between brain microstructure and cognitive function.

In conclusion, the NODDI-Bingham model appears to be more sensitive than the NODDI-Watson model, based on the significant correlations identified in the results, which align with its theoretical advantage of representing complex fiber orientations. This increased sensitivity is expected from the premises of both models, given the Bingham distribution's flexibility in capturing detailed microstructural information compared to the simpler Watson distribution.

5.5 Potential and challenges for early detection of the disease

5.5.1 Capability of NODDI models

Both NODDI models, especially the Bingham model, have shown sensitivity to microstructural changes in brain regions that are crucial for cognitive functions, such as the cortex, hippocampus and putamen. These changes might occur before significant cognitive decline is evident, implying that NODDI could potentially detect early sign of neurodegeneration.
Moreover, significant correlations with MMSE and MoCa suggest that the microstructural metrics measured by NODDI are relevant to cognitive impairment. Since these cognitive tests are often used to diagnose the early stages of AD, this correlation implies that NODDI metrics could serve as early biomarkers. However, the correlation values, despite being statistically significant, are moderate (0.3 - 0.5), indicating that, although a relationship can be found, it is not strong enough on its own to serve as a definitive diagnostic tool. Nevertheless, it is well known that Alzheimer's disease is characterized

by a long preclinical phase, during which pathological changes occur without overt cognitive symptoms. Microsctructural changes detectable by NODDI could potentially reflect these early pathological changes, making it a candidate for early detection.
When it comes to the comparison with other biomarkers, it is acknowledged that traditional imaging techniques such as structural MRI or PET scans are already used to detect early signs of AD. NODDI could complement these tecniques by providing additional information about the brain's microstructure.

5.5.2 Challenges and considerations

The results indicate that NODDI, particularly the Bingham model, has potential as part of a toolkit for early detection of Alzheimer's disease. Its sensitivity to microstructural changes that correlate with cognitive decline suggests that it could provide valuable insights, especially when combined with other biomarkers and cognitive assessments. However, due to the moderate strength of the correlations and the need for further validation, NODDI is likely to be most effective when used in conjunction with other diagnostic methods rather than as a standalone tool.
To fully explore the potential of NODDI for early detection it might be useful to conduct larger, longitudinal studies to validate the findings and establish the temporal relationship between NODDI metrics and disease progression. In addition, it may be worth to combine NODDI with other biomarkers (e.g., amyloid PET, tau PET, genetic testing) to improve predictive accuracy. Finally, it could be helpful to develop clinical protocols that integrate NODDI into routine diagnostic workflows, possibly focusing on high-risk populations.
Overall, while promising, the use of NODDI for early detection of Alzheimer's disease requires further research and development before it can be considered a reliable clinical tool. This preliminary analysis highlights the potential value of NODDI as a diagnostic tool, indicating its promise in revealing microstructural brain changes. However, for more accurate and comprehensive results, a more detailed parcellation of the brain may be useful to enhance the accuracy and relevance of the analysis.

Chapter 6

Appendix

6.1 Subject groups

Ref ID	Image Data ID	Subject ID	Sex	Age	Visit	Modality	Description	Acq Date
AD_1	I916119	007_S_4637	F	76	init	MRI	Acc. Sag. MPRAGE	10/10/17
AD_1	I916134	007_S_4637	F	76	init	DTI	Axial MB DTI	10/10/17
AD_2	I1223044	022_S_6796	M	72	sc	DTI	Axial MB DTI	03/09/19
AD_2	I1223029	022_S_6796	M	72	sc	MRI	Acc. Sag. MPRAGE	03/09/19
AD_3	I1114881	023_S_6661	F	75	sc	MRI	Acc. Sag. MPRAGE	07/01/19
AD_3	I1114875	023_S_6661	F	75	sc	DTI	Axial MB DTI	07/01/19
AD_4	I992628	037_S_6216	M	84	sc	MRI	Acc. Sag. MPRAGE	03/05/18
AD_4	I992650	037_S_6216	M	84	sc	DTI	Axial MB DTI	03/05/18
AD_5	I1004758	037_S_6230	F	84	sc	DTI	Axial MB DTI	01/06/18
AD_5	I1004740	037_S_6230	F	84	sc	MRI	Acc. Sag. MPRAGE	01/06/18
AD_6	I1017745	037_S_6377	F	82	sc	DTI	Axial MB DTI	06/07/18
AD_6	I1017725	037_S_6377	F	82	sc	MRI	Acc. Sag. MPRAGE	06/07/18
AD_9	I1529914	067_S_7033	F	59	sc	MRI	Acc. Sag. MPRAGE	03/01/22
AD_9	I1529930	067_S_7033	F	59	sc	DTI	Axial MB DTI	03/01/22
AD_10	I1231978	341_S_6820	M	68	sc	MRI	Acc. Sag. MPRAGE	25/09/19
AD_10	I1231994	341_S_6820	M	68	sc	DTI	Axial MB DTI	25/09/19
AD_11	I1291638	941_S_6854	M	86	sc	MRI	Acc. Sag. MPRAGE	14/02/20
AD_11	I1291658	941_S_6854	M	86	sc	DTI	Axial MB DTI	14/02/20
AD_12	I1467526	941_S_6962	F	75	sc	MRI	Acc. Sag. MPRAGE	13/07/21
AD_12	I1467555	941_S_6962	F	75	sc	DTI	Axial MB DTI	13/07/21

Table 6.1: ADNI-3 AD patients acquisition and demographic specifics.

Ref ID	Image Data ID	Subject ID	Sex	Age	Visit	Modality	Description	Acq Date
MCI_1	I1118737	002_S_6652	F	86	sc	DTI	Axial MB DTI	13/12/18
MCI_1	I1118713	002_S_6652	F	86	sc	MRI	Acc. Sag. MPRAGE	13/12/18
MCI_2	I1303613	002_S_6864	F	69	sc	MRI	Acc. Sag. MPRAGE	11/03/20
MCI_2	I1303626	002_S_6864	F	69	sc	DTI	Axial MB DTI	11/03/20
MCI_3	I1325460	036_S_6878	M	75	sc	DTI	Axial MB DTI	23/07/20
MCI_3	I1325444	036_S_6878	M	75	sc	MRI	Acc. Sag. MPRAGE	23/07/20
MCI_4	I1343918	036_S_6887	F	73	sc	DTI	Axial MB DTI	25/09/20
MCI_4	I1343905	036_S_6887	F	73	sc	MRI	Acc. Sag. MPRAGE	25/09/20
MCI_5	I1422865	036_S_6916	M	77	sc	DTI	Axial MB DTI	18/03/21
MCI_5	I1422849	036_S_6916	M	77	sc	MRI	Acc. Sag. MPRAGE	18/03/21
MCI_6	I1003961	037_S_6222	F	74	sc	MRI	Acc. Sag. MPRAGE	30/05/18
MCI_6	I1003977	037_S_6222	F	74	sc	DTI	Axial MB DTI	30/05/18
MCI_7	I1080140	037_S_6627	F	68	sc	DTI	Axial MB DTI	30/11/18
MCI_7	I1080124	037_S_6627	F	68	sc	MRI	Acc. Sag. MPRAGE	30/11/18
MCI_8	I1258699	052_S_6832	M	79	sc	DTI	Axial MB DTI	15/11/19
MCI_8	I1258698	052_S_6832	M	79	sc	MRI	Acc. Sag. MPRAGE	15/11/19
MCI_9	I1272315	052_S_6844	F	76	sc	DTI	Axial MB DTI	03/01/20
MCI_9	I1272307	052_S_6844	F	76	sc	MRI	Acc. Sag. MPRAGE	03/01/20

Table 6.2: ADNI-3 MCI patients acquisition and demographic specifics.

Ref ID	Image Data ID	Subject ID	Sex	Age	Visit	Modality	Description	Acq Date
MCI_10	I1521048	052_S_7027	F	71	sc	MRI	Acc. Sag. MPRAGE	30/11/21
MCI_10	I1521052	052_S_7027	F	71	sc	DTI	Axial MB DTI	30/11/21
MCI_11	I1014602	067_S_6474	M	74	sc	MRI	Acc. Sag. MPRAGE	27/06/18
MCI_11	I1014596	067_S_6474	M	74	sc	DTI	Axial MB DTI	27/06/18
MCI_12	I1496165	067_S_6989	F	68	sc	MRI	Acc. Sag. MPRAGE	21/09/21
MCI_12	I1496181	067_S_6989	F	68	sc	DTI	Axial MB DTI	21/09/21
MCI_13	I1501139	067_S_7008	F	74	sc	MRI	Acc. Sag. MPRAGE	06/10/21
MCI_13	I1501158	067_S_7008	F	74	sc	DTI	Axial MB DTI	06/10/21
MCI_14	I1022146	128_S_0205	F	79	init	DTI	Axial MB DTI	17/07/18
MCI_14	I1022130	128_S_0205	F	79	init	MRI	Acc. Sag. MPRAGE	17/07/18
MCI_15	I1132977	341_S_6686	M	79	sc	MRI	Acc. Sag. MPRAGE	20/02/19
MCI_15	I1132994	341_S_6686	M	79	sc	DTI	Axial MB DTI	20/02/19
MCI_16	I996464	941_S_6345	M	79	sc	MRI	Acc. Sag. MPRAGE	10/05/18
MCI_16	I996480	941_S_6345	M	79	sc	DTI	Axial MB DTI	10/05/18
MCI_17	I1005030	941_S_6392	M	89	sc	MRI	Acc. Sag. MPRAGE	30/05/18
MCI_17	I1005046	941_S_6392	M	89	sc	DTI	Axial MB DTI	30/05/18
MCI_18	I1310799	941_S_6803	F	75	sc	DTI	Axial MB DTI	16/09/19
MCI_18	I1310783	941_S_6803	F	75	sc	MRI	Acc. Sag. MPRAGE	16/09/19

Table 6.3: ADNI-3 MCI patients acquisition and demographic specifics.

Ref ID	Image Data ID	Subject ID	Sex	Age	Visit	Modality	Description	Acq Date
CN_1	I973557	037_S_6187	F	74	sc	DTI	Axial MB DTI	14/03/18
CN_1	I973541	037_S_6187	F	74	sc	MRI	Acc. Sag. MPRAGE	14/03/18
CN_2	I1478795	037_S_6974	F	81	sc	DTI	Axial MB DTI	10/08/21
CN_2	I1478784	037_S_6974	F	81	sc	MRI	Acc. Sag. MPRAGE	10/08/21
CN_3	I1514347	037_S_6992	F	53	sc	DTI	Axial MB DTI	09/11/21
CN_3	I1514331	037_S_6992	F	53	sc	MRI	Acc. Sag. MPRAGE	09/11/21
CN_4	I1029901	052_S_6412	M	68	sc	DTI	Axial MB DTI	01/08/18
CN_4	I1029891	052_S_6412	M	68	sc	MRI	Acc. Sag. MPRAGE	01/08/18
CN_5	I1011199	067_S_6442	M	78	sc	DTI	Axial MB DTI	15/06/18
CN_5	I1011188	067_S_6442	M	78	sc	MRI	Acc. Sag. MPRAGE	15/06/18
CN_6	I1011210	067_S_6443	F	77	sc	DTI	Axial MB DTI	15/06/18
CN_6	I1011216	067_S_6443	F	77	sc	MRI	Acc. Sag. MPRAGE	15/06/18
CN_7	I1469940	067_S_6957	M	78	sc	MRI	Acc. Sag. MPRAGE	16/07/21
CN_7	I1469957	067_S_6957	M	78	sc	DTI	Axial MB DTI	16/07/21
CN_8	I1470151	067_S_6958	F	76	sc	MRI	Acc. Sag. MPRAGE	16/07/21
CN_8	I1470167	067_S_6958	F	76	sc	DTI	Axial MB DTI	16/07/21
CN_9	I1021968	941_S_6495	F	83	sc	MRI	Acc. Sag. MPRAGE	17/07/21
CN_9	I1021984	941_S_6495	F	83	sc	DTI	Axial MB DTI	17/07/21
CN_10	I1022057	941_S_6496	M	85	sc	MRI	Acc. Sag. MPRAGE	17/07/21
CN_10	I1022076	941_S_6496	M	85	sc	DTI	Axial MB DTI	17/07/21
CN_11	I1034868	941_S_6546	F	80	sc	DTI	Axial MB DTI	08/08/18
CN_11	I1034852	941_S_6546	F	80	sc	MRI	Acc. Sag. MPRAGE	08/08/18
CN_12	I1046901	941_S_6574	F	73	sc	MRI	Acc. Sag. MPRAGE	07/09/18
CN_12	I1046927	941_S_6574	F	73	sc	DTI	Axial MB DTI	07/09/18
CN_13	I1046000	941_S_6575	M	73	sc	DTI	Axial MB DTI	05/09/18
CN_13	I1045984	941_S_6575	M	73	sc	MRI	Acc. Sag. MPRAGE	05/09/18
CN_14	I1046756	941_S_6580	F	80	sc	DTI	Axial MB DTI	07/09/18
CN_14	I1046736	941_S_6580	F	80	sc	MRI	Acc. Sag. MPRAGE	07/09/18
CN_15	I1048378	941_S_6581	F	74	sc	MRI	Acc. Sag. MPRAGE	12/09/18
CN_15	I1048394	941_S_6581	F	74	sc	DTI	Axial MB DTI	12/09/18
CN_16	I1486337	941_S_6998	M	57	sc	DTI	Axial MB DTI	30/08/21
CN_16	I1486321	941_S_6998	M	57	sc	MRI	Acc. Sag. MPRAGE	30/08/21

Table 6.4: ADNI-3 CN patients acquisition and demographic specifics.

6.2 Shapiro-Wilks results

Table 6.5: Shapiro-Wilks results for the NODDI-Bingham.

Group	Region	Parameter	Statistic	p-value
AD	Pallidum	partial_volume_1	0.9048	0.0508
AD	Pallidum	partial_volume_1	0.9048	0.0508
AD	Pallidum	beta_fraction	0.9326	0.1733
AD	Pallidum	partial_volume_0	0.9236	0.1163
AD	Pallidum	ODI	0.9720	0.7967
AD	Thalamus	partial_volume_1	0.9405	0.2448
AD	Thalamus	beta_fraction	0.9795	0.9279
AD	Thalamus	partial_volume_0	0.9460	0.3101
AD	Thalamus	ODI	0.8840	**0.0209**
AD	LateralVentricle	partial_volume_1	0.9442	0.2878
AD	LateralVentricle	beta_fraction	0.9563	0.4728
AD	LateralVentricle	partial_volume_0	0.9148	0.0786
AD	LateralVentricle	ODI	0.9558	0.4633
AD	Cortex	partial_volume_1	0.8080	**0.0011**
AD	Cortex	beta_fraction	0.8697	**0.0116**
AD	Cortex	partial_volume_0	0.9239	0.1177
AD	Cortex	ODI	0.9379	0.2184
AD	Accumbens	partial_volume_1	0.8171	**0.0016**
AD	Accumbens	beta_fraction	0.9370	0.2106
AD	Accumbens	partial_volume_0	0.9106	0.0653
AD	Accumbens	ODI	0.9193	0.0962
AD	Cerebral_WM	partial_volume_1	0.8724	**0.0129**
AD	Cerebral_WM	beta_fraction	0.9516	0.3913
AD	Cerebral_WM	partial_volume_0	0.9364	0.2048
AD	Cerebral_WM	ODI	0.9652	0.6521
AD	Putamen	partial_volume_1	0.8975	**0.0371**
AD	Putamen	beta_fraction	0.9304	0.1575
AD	Putamen	partial_volume_0	0.9562	0.4714
AD	Putamen	ODI	0.9599	0.5427
AD	Hippocampus	partial_volume_1	0.9260	0.1292
AD	Hippocampus	beta_fraction	0.9604	0.5522
AD	Hippocampus	partial_volume_0	0.9843	0.9773
AD	Hippocampus	ODI	0.9636	0.6171

Continues in the next page

Continues from the previous page

Group	Region	Parameter	Statistic	p-value
AD	CaudateNucleus	partial_volume_1	0.9006	**0.0423**
AD	CaudateNucleus	beta_fraction	0.9395	0.2344
AD	CaudateNucleus	partial_volume_0	0.9320	0.1687
AD	CaudateNucleus	ODI	0.9349	0.1919
AD	Amygdala	partial_volume_1	0.9077	0.0577
AD	Amygdala	beta_fraction	0.9427	0.2695
AD	Amygdala	partial_volume_0	0.9261	0.1298
AD	Amygdala	ODI	0.9006	**0.0423**
MCI	Pallidum	partial_volume_1	0.7981	**0.0001**
MCI	Pallidum	beta_fraction	0.9654	0.3130
MCI	Pallidum	partial_volume_0	0.9543	0.1427
MCI	Pallidum	ODI	0.9652	0.3090
MCI	Thalamus	partial_volume_1	0.9273	**0.0208**
MCI	Thalamus	beta_fraction	0.9269	**0.0202**
MCI	Thalamus	partial_volume_0	0.9839	0.8667
MCI	Thalamus	ODI	0.9689	0.3973
MCI	LateralVentricle	partial_volume_1	0.9155	**0.0093**
MCI	LateralVentricle	beta_fraction	0.9782	0.6827
MCI	LateralVentricle	partial_volume_0	0.8610	**0.0003**
MCI	LateralVentricle	ODI	0.9483	0.0927
MCI	Cortex	partial_volume_1	0.9365	**0.0395**
MCI	Cortex	beta_fraction	0.9254	**0.0181**
MCI	Cortex	partial_volume_0	0.9540	0.1396
MCI	Cortex	ODI	0.9454	0.0748
MCI	Accumbens	partial_volume_1	0.9088	**0.0060**
MCI	Accumbens	beta_fraction	0.9414	0.0562
MCI	Accumbens	partial_volume_0	0.9856	0.9118
MCI	Accumbens	ODI	0.9731	0.5162
MCI	Cerebral_WM	partial_volume_1	0.9365	**0.0394**
MCI	Cerebral_WM	beta_fraction	0.9508	0.1109
MCI	Cerebral_WM	partial_volume_0	0.9853	0.9044
MCI	Cerebral_WM	ODI	0.9643	0.2899
MCI	Putamen	partial_volume_1	0.7175	**0.0001**
MCI	Putamen	beta_fraction	0.9631	0.2679
MCI	Putamen	partial_volume_0	0.9741	0.5488
MCI	Putamen	ODI	0.9505	0.1085
MCI	Hippocampus	partial_volume_1	0.9619	0.2463

Continues in the next page

Continues from the previous page

Group	Region	Parameter	Statistic	p-value
MCI	Hippocampus	beta_fraction	0.9613	0.2363
MCI	Hippocampus	partial_volume_0	0.9579	0.1845
MCI	Hippocampus	ODI	0.9789	0.7072
MCI	CaudateNucleus	partial_volume_1	0.9845	0.8836
MCI	CaudateNucleus	beta_fraction	0.9760	0.6092
MCI	CaudateNucleus	partial_volume_0	0.9776	0.6649
MCI	CaudateNucleus	ODI	0.9839	0.8679
MCI	Amygdala	partial_volume_1	0.9296	**0.0244**
MCI	Amygdala	beta_fraction	0.9596	0.2096
MCI	Amygdala	partial_volume_0	0.9132	**0.0080**
MCI	Amygdala	ODI	0.9502	0.1059
CN	Pallidum	partial_volume_1	0.9427	0.0892
CN	Pallidum	beta_fraction	0.9519	0.1635
CN	Pallidum	partial_volume_0	0.9520	0.1645
CN	Pallidum	ODI	0.9393	0.0714
CN	Thalamus	partial_volume_1	0.9474	0.1217
CN	Thalamus	beta_fraction	0.9742	0.6212
CN	Thalamus	partial_volume_0	0.8974	**0.0053**
CN	Thalamus	ODI	0.9769	0.7045
CN	LateralVentricle	partial_volume_1	0.9127	**0.0133**
CN	LateralVentricle	beta_fraction	0.9433	0.0926
CN	LateralVentricle	partial_volume_0	0.9449	0.1032
CN	LateralVentricle	ODI	0.9654	0.3836
CN	Cortex	partial_volume_1	0.9790	0.7690
CN	Cortex	beta_fraction	0.9834	0.8903
CN	Cortex	partial_volume_0	0.9762	0.6827
CN	Cortex	ODI	0.9776	0.7259
CN	Accumbens	partial_volume_1	0.8565	**0.0006**
CN	Accumbens	beta_fraction	0.9658	0.3922
CN	Accumbens	partial_volume_0	0.9460	0.1111
CN	Accumbens	ODI	0.9563	0.2164
CN	Cerebral_WM	partial_volume_1	0.9558	0.2098
CN	Cerebral_WM	beta_fraction	0.8885	**0.0032**
CN	Cerebral_WM	partial_volume_0	0.9674	0.4306
CN	Cerebral_WM	ODI	0.9328	**0.0468**
CN	Putamen	partial_volume_1	0.8698	**0.0011**
CN	Putamen	beta_fraction	0.9790	0.7697

Continues in the next page

Continues from the previous page

Group	Region	Parameter	Statistic	p-value
CN	Putamen	partial_volume_0	0.9795	0.7857
CN	Putamen	ODI	0.9671	0.4230
CN	Hippocampus	partial_volume_1	0.9758	0.6728
CN	Hippocampus	beta_fraction	0.9720	0.5565
CN	Hippocampus	partial_volume_0	0.9607	0.2874
CN	Hippocampus	ODI	0.9701	0.5016
CN	CaudateNucleus	partial_volume_1	0.9368	0.0608
CN	CaudateNucleus	beta_fraction	0.9722	0.5625
CN	CaudateNucleus	partial_volume_0	0.9799	0.7967
CN	CaudateNucleus	ODI	0.9804	0.8118
CN	Amygdala	partial_volume_1	0.9741	0.6191
CN	Amygdala	beta_fraction	0.9772	0.7142
CN	Amygdala	partial_volume_0	0.9843	0.9112
CN	Amygdala	ODI	0.8865	**0.0029**

Table 6.6: Shapiro-Wilks results for the NODDI-Watson.

Group	Region	Parameter	Statistic	p-value
AD	Pallidum	partial_volume_1	0.8949	**0.0331**
AD	Pallidum	ODI	0.9620	0.5854
AD	Pallidum	partial_volume_0	0.9233	0.1146
AD	Thalamus	partial_volume_1	0.9402	0.2421
AD	Thalamus	ODI	0.9636	0.6170
AD	Thalamus	partial_volume_0	0.9520	0.3979
AD	LateralVentricle	partial_volume_1	0.9442	0.2876
AD	LateralVentricle	ODI	0.9480	0.3382
AD	LateralVentricle	partial_volume_0	0.9048	0.0508
AD	Cortex	partial_volume_1	0.8071	**0.0011**
AD	Cortex	ODI	0.9419	0.2603
AD	Cortex	partial_volume_0	0.9224	0.1103
AD	Accumbens	partial_volume_1	0.8137	**0.0014**
AD	Accumbens	ODI	0.9353	0.1950
AD	Accumbens	partial_volume_0	0.9070	0.0559
AD	Cerebral_WM	partial_volume_1	0.8638	**0.0092**
AD	Cerebral_WM	ODI	0.9617	0.5787
AD	Cerebral_WM	partial_volume_0	0.9335	0.1799

Continues in the next page

Continues from the previous page

Group	Region	Parameter	Statistic	p-value
AD	Putamen	partial_volume_1	0.8817	**0.0190**
AD	Putamen	ODI	0.9455	0.3033
AD	Putamen	partial_volume_0	0.9536	0.4243
AD	Hippocampus	partial_volume_1	0.9271	0.1360
AD	Hippocampus	ODI	0.9566	0.4776
AD	Hippocampus	partial_volume_0	0.9752	0.8580
AD	CaudateNucleus	partial_volume_1	0.9017	**0.0444**
AD	CaudateNucleus	ODI	0.9457	0.3065
AD	CaudateNucleus	partial_volume_0	0.9279	0.1404
AD	Amygdala	partial_volume_1	0.9105	0.0650
AD	Amygdala	ODI	0.8764	**0.0152**
AD	Amygdala	partial_volume_0	0.9460	0.3103
MCI	Pallidum	partial_volume_1	0.8055	**0.0001**
MCI	Pallidum	ODI	0.9588	0.1974
MCI	Pallidum	partial_volume_0	0.9468	0.0829
MCI	Thalamus	partial_volume_1	0.9265	**0.0197**
MCI	Thalamus	ODI	0.9532	0.1322
MCI	Thalamus	partial_volume_0	0.9838	0.8659
MCI	LateralVentricle	partial_volume_1	0.9150	**0.0090**
MCI	LateralVentricle	ODI	0.9529	0.1292
MCI	LateralVentricle	partial_volume_0	0.8680	**0.0005**
MCI	Cortex	partial_volume_1	0.9365	**0.0397**
MCI	Cortex	ODI	0.9117	**0.0072**
MCI	Cortex	partial_volume_0	0.9527	0.1275
MCI	Accumbens	partial_volume_1	0.9088	**0.0060**
MCI	Accumbens	ODI	0.9781	0.6822
MCI	Accumbens	partial_volume_0	0.9852	0.9021
MCI	Cerebral_WM	partial_volume_1	0.9351	**0.0357**
MCI	Cerebral_WM	ODI	0.9692	0.4048
MCI	Cerebral_WM	partial_volume_0	0.9826	0.8303
MCI	Putamen	partial_volume_1	0.7169	**0.0001**
MCI	Putamen	ODI	0.9494	0.1004
MCI	Putamen	partial_volume_0	0.9733	0.5225
MCI	Hippocampus	partial_volume_1	0.9637	0.2792
MCI	Hippocampus	ODI	0.9854	0.9066
MCI	Hippocampus	partial_volume_0	0.9591	0.2016
MCI	CaudateNucleus	partial_volume_1	0.9849	0.8945

Continues in the next page

Continues from the previous page

Group	Region	Parameter	Statistic	p-value
MCI	CaudateNucleus	ODI	0.9907	0.9885
MCI	CaudateNucleus	partial_volume_0	0.9811	0.7808
MCI	Amygdala	partial_volume_1	0.9286	**0.0227**
MCI	Amygdala	ODI	0.9438	0.0668
MCI	Amygdala	partial_volume_0	0.9092	**0.0062**
CN	Pallidum	partial_volume_1	0.9470	0.1182
CN	Pallidum	ODI	0.9229	**0.0250**
CN	Pallidum	partial_volume_0	0.9503	0.1473
CN	Thalamus	partial_volume_1	0.9473	0.1204
CN	Thalamus	ODI	0.9812	0.8330
CN	Thalamus	partial_volume_0	0.8923	**0.0040**
CN	LateralVentricle	partial_volume_1	0.9135	**0.0139**
CN	LateralVentricle	ODI	0.9673	0.4294
CN	LateralVentricle	partial_volume_0	0.9450	0.1037
CN	Cortex	partial_volume_1	0.9786	0.7584
CN	Cortex	ODI	0.9788	0.7637
CN	Cortex	partial_volume_0	0.9763	0.6874
CN	Accumbens	partial_volume_1	0.8554	**0.0005**
CN	Accumbens	ODI	0.9642	0.3567
CN	Accumbens	partial_volume_0	0.9446	0.1014
CN	Cerebral_WM	partial_volume_1	0.9558	0.2100
CN	Cerebral_WM	ODI	0.9360	0.0579
CN	Cerebral_WM	partial_volume_0	0.9674	0.4297
CN	Putamen	partial_volume_1	0.8727	**0.0013**
CN	Putamen	ODI	0.9600	0.2738
CN	Putamen	partial_volume_0	0.9787	0.7625
CN	Hippocampus	partial_volume_1	0.9747	0.6363
CN	Hippocampus	ODI	0.9404	0.0771
CN	Hippocampus	partial_volume_0	0.9620	0.3103
CN	CaudateNucleus	partial_volume_1	0.9346	0.0527
CN	CaudateNucleus	ODI	0.9648	0.3701
CN	CaudateNucleus	partial_volume_0	0.9791	0.7718
CN	Amygdala	partial_volume_1	0.9748	0.6402
CN	Amygdala	ODI	0.8837	**0.0024**
CN	Amygdala	partial_volume_0	0.9827	0.8739

6.3 Tukey's HSD test results

Parameter	Region	Comparison	p-value	p-value (BH)
beta_fraction	Cortex	AD vs CN	0.793	0.793
beta_fraction	Cortex	AD vs MCI	0.1176	0.1764
beta_fraction	Cortex	CN vs MCI	**0.0107**	**0.0321**
beta_fraction	Putamen	AD vs CN	**0.0219**	0.0657
beta_fraction	Putamen	AD vs MCI	0.0943	0.14145
beta_fraction	Putamen	CN vs MCI	0.6883	0.6883
ODI	Caudate Nucleus	AD vs CN	**0.0405**	0.1215
ODI	Caudate Nucleus	AD vs MCI	0.6703	0.6703
ODI	Caudate Nucleus	CN vs MCI	0.1248	0.1872
ODI	Cortex	AD vs CN	**0.0017**	**0.0051**
ODI	Cortex	AD vs MCI	**0.0147**	**0.02205**
ODI	Cortex	CN vs MCI	0.5851	0.5851
ODI	Putamen	AD vs CN	**0.0031**	**0.0093**
ODI	Putamen	AD vs MCI	0.098	0.147
ODI	Putamen	CN vs MCI	0.2241	0.2241
ODI	Thalamus	AD vs CN	0.1569	0.23535
ODI	Thalamus	AD vs MCI	0.9	0.9
ODI	Thalamus	CN vs MCI	**0.0313**	0.0939
partial_volume_0	Cerebral WM	AD vs CN	**0.0018**	**0.0054**
partial_volume_0	Cerebral WM	AD vs MCI	0.0709	0.10635
partial_volume_0	Cerebral WM	CN vs MCI	0.2058	0.2058
partial_volume_0	Lateral Ventricle	AD vs CN	0.6036	0.6036
partial_volume_0	Lateral Ventricle	AD vs MCI	0.3891	0.58365
partial_volume_0	Lateral Ventricle	CN vs MCI	**0.0305**	0.0915
partial_volume_0	Pallidum	AD vs CN	**0.0023**	**0.0069**
partial_volume_0	Pallidum	AD vs MCI	0.1179	0.1481
partial_volume_0	Pallidum	CN vs MCI	0.1481	0.1481
partial_volume_1	Cortex	AD vs CN	**0.0091**	**0.0174**
partial_volume_1	Cortex	AD vs MCI	0.832	0.832
partial_volume_1	Cortex	CN vs MCI	**0.0116**	**0.0174**
partial_volume_1	Hippocampus	AD vs CN	**0.0122**	**0.0366**
partial_volume_1	Hippocampus	AD vs MCI	0.5803	0.5803
partial_volume_1	Hippocampus	CN vs MCI	0.0551	0.08265

Table 6.7: Tukey's test results for the NODDI-Bingham. The last column indicates the adjusted p-value after the Benjamini-Hochberg procedure.

Parameter	**Region**	**Comparison**	**p-value**	**p-value (BH)**
ODI	Caudate Nucleus	AD vs CN	**0.0496**	0.1488
ODI	Caudate Nucleus	AD vs MCI	0.7605	0.7605
ODI	Caudate Nucleus	CN vs MCI	0.1068	0.1602
ODI	Cortex	AD vs CN	**0.0037**	**0.0111**
ODI	Cortex	AD vs MCI	0.0659	0.09885
ODI	Cortex	CN vs MCI	0.3558	0.3558
ODI	Putamen	AD vs CN	**0.0054**	**0.0162**
ODI	Putamen	AD vs MCI	0.177	0.181
ODI	Putamen	CN vs MCI	0.181	0.181
partial_volume_0	Cerebral WM	AD vs CN	**0.0021**	**0.0063**
partial_volume_0	Cerebral WM	AD vs MCI	0.0742	0.1113
partial_volume_0	Cerebral WM	CN vs MCI	0.2242	0.2242
partial_volume_0	Lateral Ventricle	AD vs CN	0.5965	0.5965
partial_volume_0	Lateral Ventricle	AD vs MCI	0.3889	0.58335
partial_volume_0	Lateral Ventricle	CN vs MCI	**0.0294**	0.0882
partial_volume_0	Pallidum	AD vs CN	**0.0025**	**0.0075**
partial_volume_0	Pallidum	AD vs MCI	0.1273	0.1445
partial_volume_0	Pallidum	CN vs MCI	0.1445	0.1445
partial_volume_1	Cortex	AD vs CN	**0.009**	**0.0174**
partial_volume_1	Cortex	AD vs MCI	0.8303	0.8303
partial_volume_1	Cortex	CN vs MCI	**0.0116**	**0.0174**
partial_volume_1	Hippocampus	AD vs CN	**0.0129**	**0.0387**
partial_volume_1	Hippocampus	AD vs MCI	0.5812	0.5812
partial_volume_1	Hippocampus	CN vs MCI	0.0581	0.08715

Table 6.8: Tukey's test results for the NODDI-Watson. The last column indicates the adjusted p-value after the Benjamini-Hochberg procedure.

6.4 MMSE and MoCa correlation plots

This section contains the scatter plots obtained by the Pearson's correlation analysis described in Chapter 4.2.4, testing each pair of significant metrics against the MMSE/MoCa scores for the relative patients.
The correlation plots releal that the NODDI-Bingham model demonstrates stronger associations between microstructural brain parameters and cognitive scores, particularly in regions such as the Hippocampus and Putamen, suggesting its greater sensitivity in detecting early Alzheimer's-related changes.
The NODDI-Watson model, while still indicating significant correlations, generally shows weaker relationships, reflecting its limited precision compared to the Bingham model.

6.4.1 NODDI-Bingham metrics

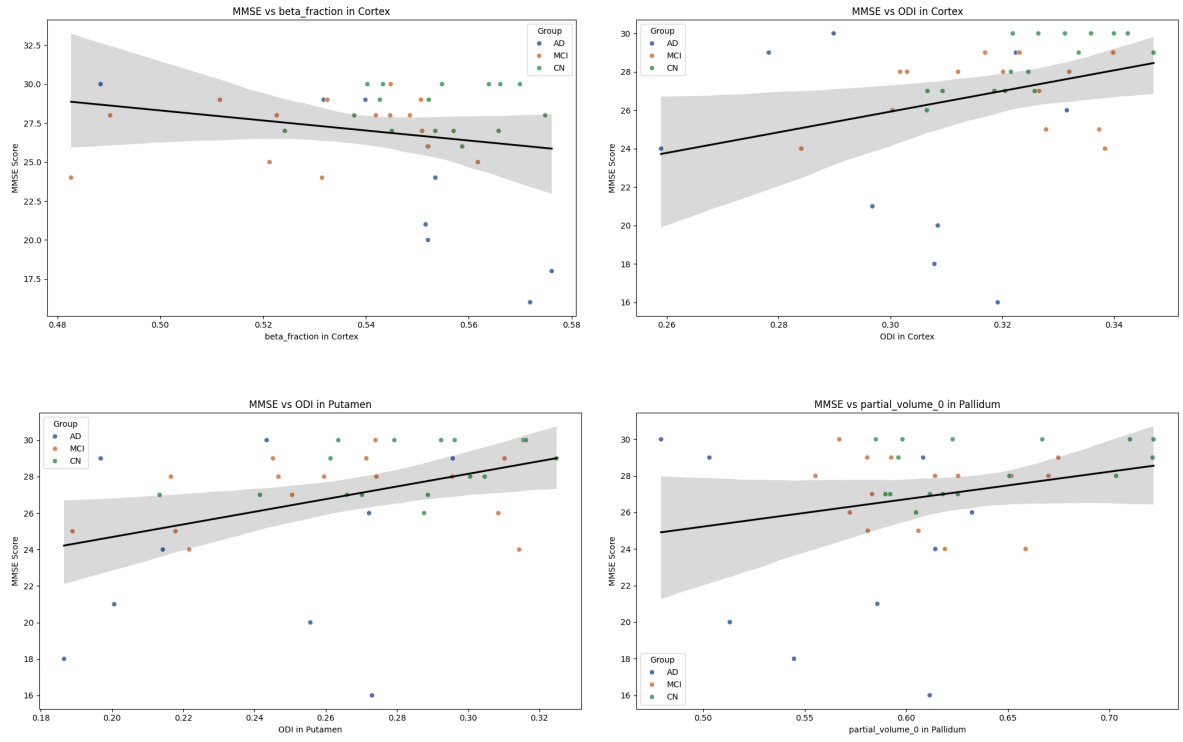

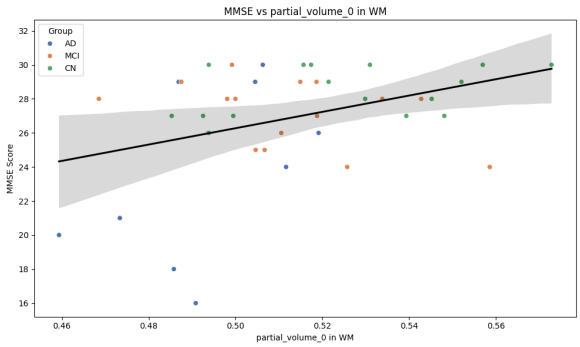
MMSE vs partial_volume_0 in WM
Group
AD
MCI
CN
MMSE Score
partial_volume_0 in WM

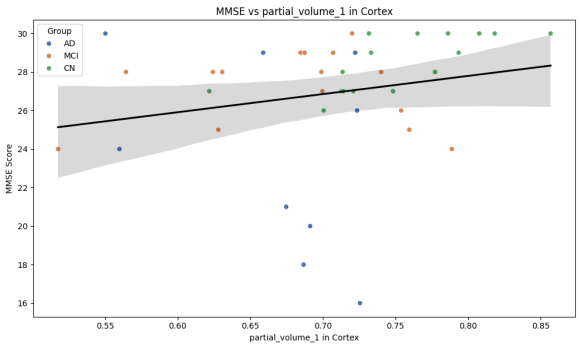
MMSE vs partial_volume_1 in Cortex
Group
AD
MCI
CN
MMSE Score
partial_volume_1 in Cortex

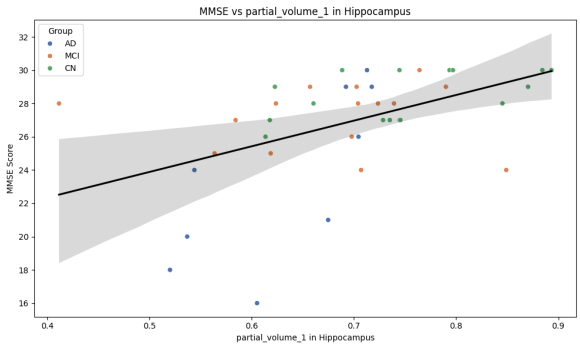
MMSE vs partial_volume_1 in Hippocampus
Group
AD
MCI
CN
MMSE Score
partial_volume_1 in Hippocampus

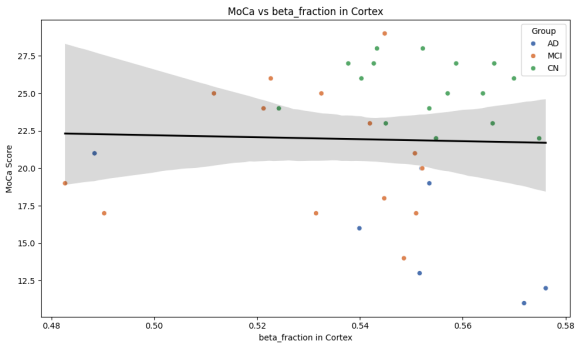
MoCa vs beta_fraction in Cortex
Group
AD
MCI
CN
MoCa Score
beta_fraction in Cortex

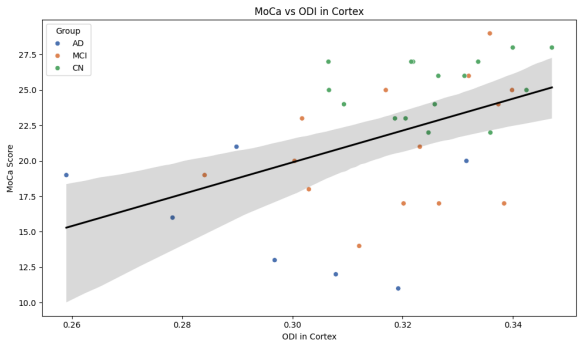
MoCa vs ODI in Cortex
Group
AD
MCI
CN
MoCa Score
ODI in Cortex

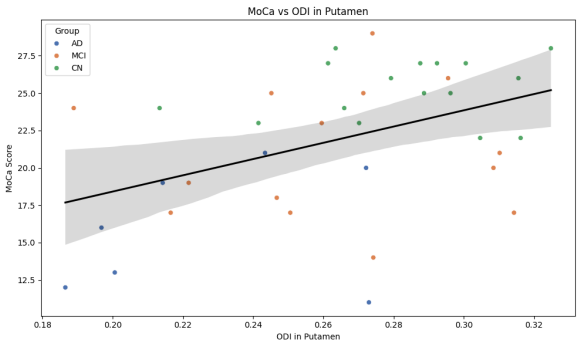
MoCa vs ODI in Putamen
Group
AD
MCI
CN
MoCa Score
ODI in Putamen

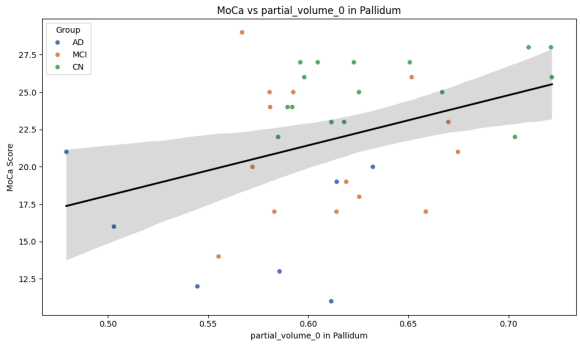
MoCa vs partial_volume_0 in Pallidum
Group
AD
MCI
CN
MoCa Score
partial_volume_0 in Pallidum

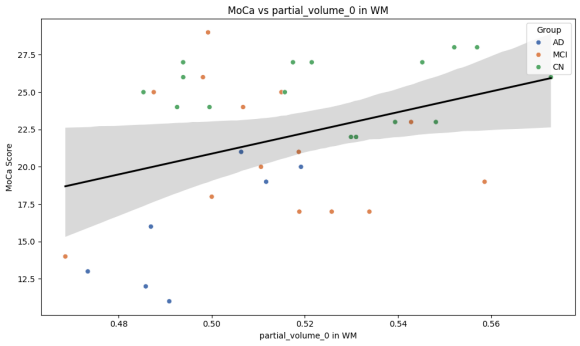
MoCa vs partial_volume_0 in WM
Group
AD
MCI
CN
MoCa Score
partial_volume_0 in WM

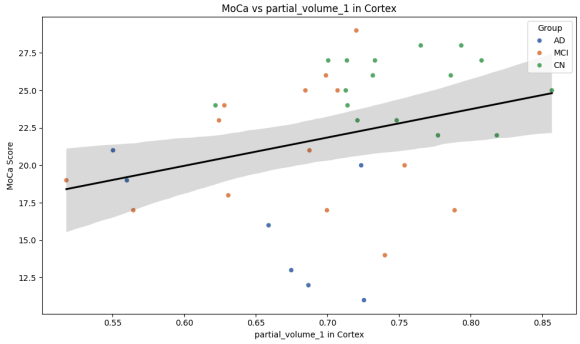
MoCa vs partial_volume_1 in Cortex
Group
AD
MCI
CN
MoCa Score
partial_volume_1 in Cortex
27.5
25.0
22.5
20.0
17.5
15.0
12.5
0.55
0.60
0.65
0.70
0.75
0.80
0.85

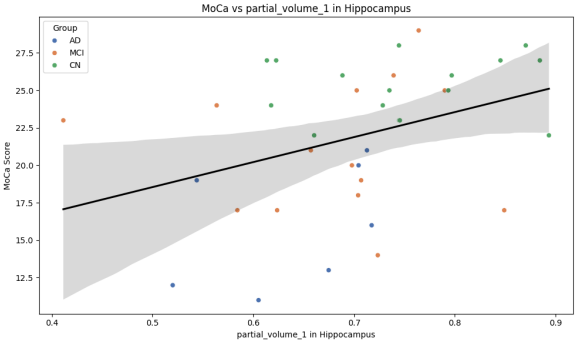
MoCa vs partial_volume_1 in Hippocampus
Group
AD
MCI
CN
MoCa Score
partial_volume_1 in Hippocampus
27.5
25.0
22.5
20.0
17.5
15.0
12.5
0.4
0.5
0.6
0.7
0.8
0.9

6.4.2 NODDI-Watson metrics

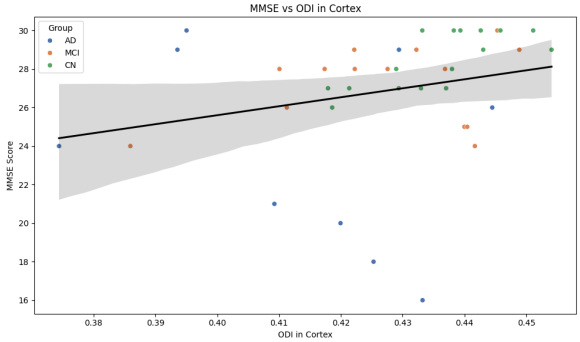

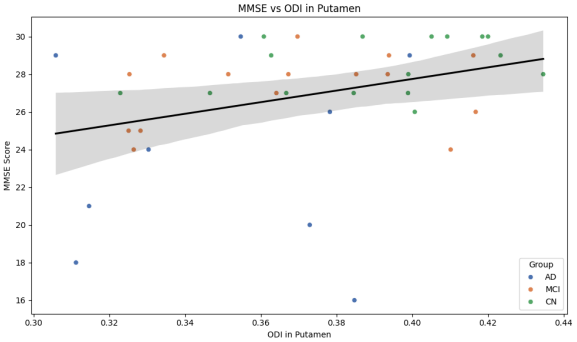

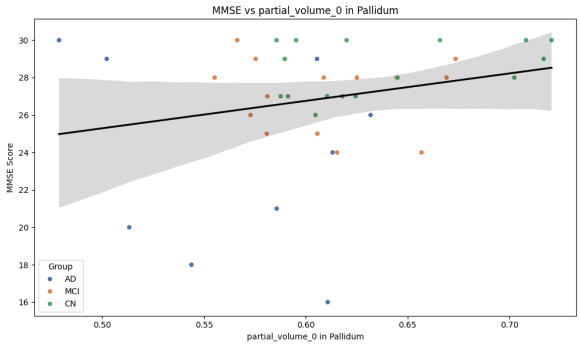

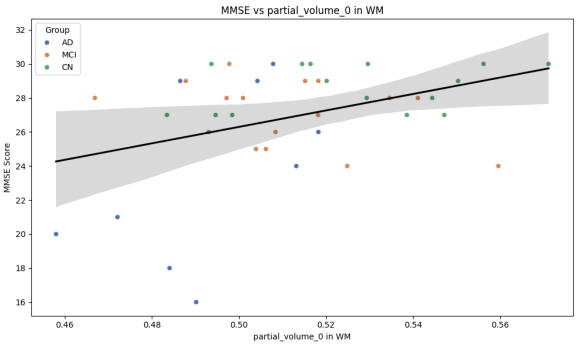

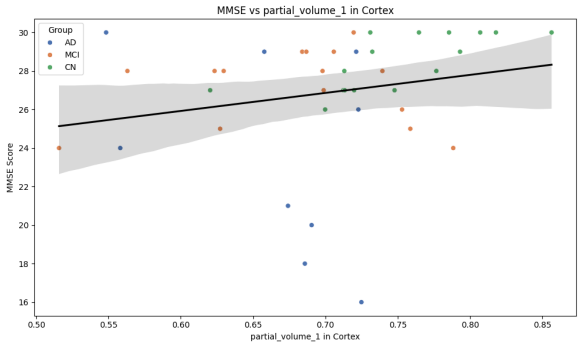

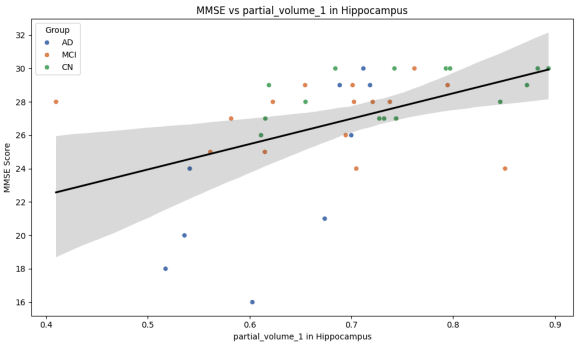

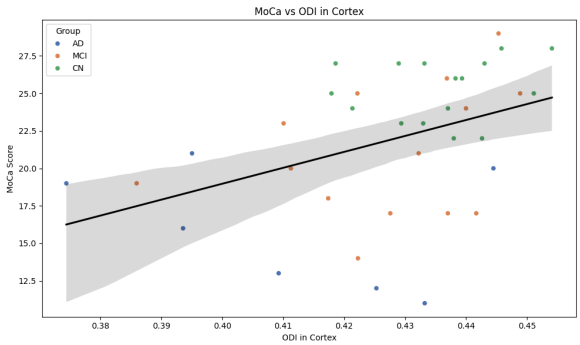
MoCa vs ODI in Cortex
Group
AD
MCI
CN
MoCa Score
ODI in Cortex

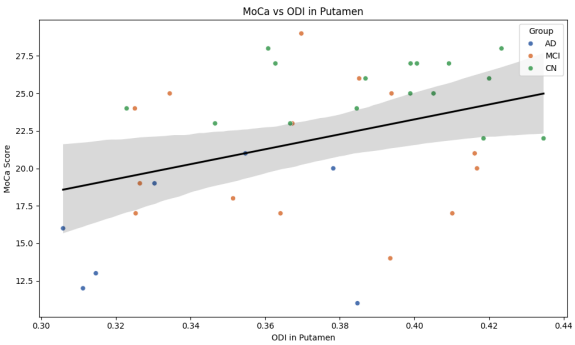
MoCa vs ODI in Putamen
Group
AD
MCI
CN
MoCa Score
ODI in Putamen

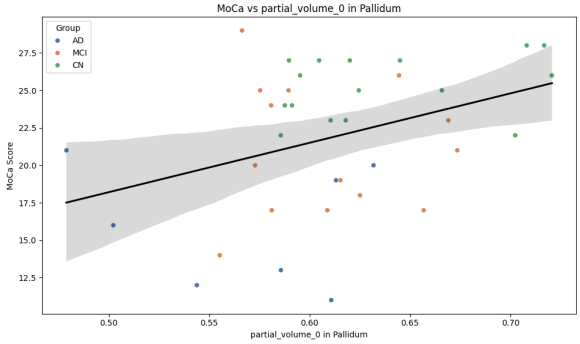
MoCa vs partial_volume_0 in Pallidum
Group
AD
MCI
CN
MoCa Score
partial_volume_0 in Pallidum

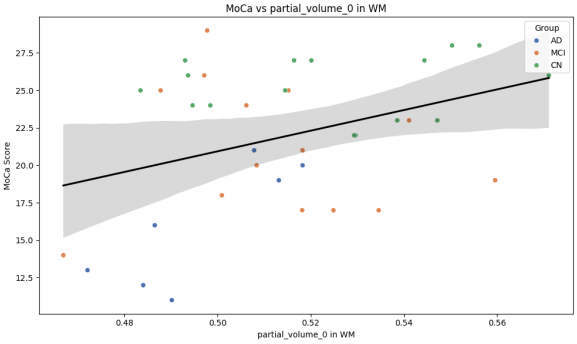
MoCa vs partial_volume_0 in WM
Group
AD
MCI
CN
MoCa Score
partial_volume_0 in WM

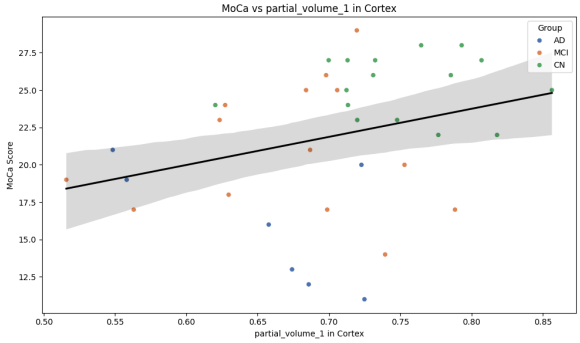
MoCa vs partial_volume_1 in Cortex
Group
AD
MCI
CN
MoCa Score
partial_volume_1 in Cortex

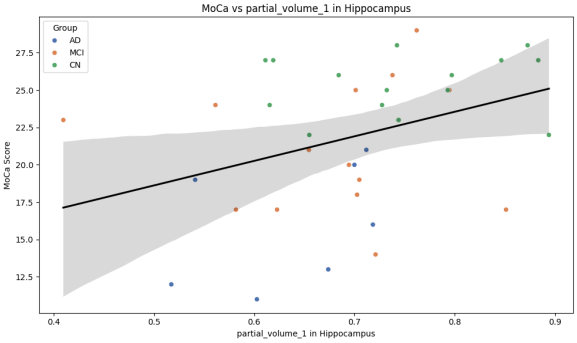
MoCa vs partial_volume_1 in Hippocampus
Group
AD
MCI
CN
MoCa Score
partial_volume_1 in Hippocampus

Bibliography

[Acosta-Cabronero et al., 2012] Acosta-Cabronero, J., Alley, S., Williams, G. B., Pengas, G., and Nestor, P. J. (2012). Diffusion tensor metrics as biomarkers in alzheimer's disease. *PloS one*, 7(11):e49072.

[Aisen et al., 2017] Aisen, P. S., Cummings, J., Jack, C. R., Morris, J. C., Sperling, R., Frölich, L., and Jones, R. W. (2017). On the path to 2025: understanding the alzheimer's disease continuum. *Alzheimer's research & therapy*, 9(1):60.

[Alexander, 2008] Alexander, D. C. (2008). A general framework for experiment design in diffusion mri and its application in measuring direct tissue-microstructure features. *Magnetic Resonance in Medicine: An Official Journal of the International Society for Magnetic Resonance in Medicine*, 60(2):439–448.

[Alexander and Barker, 2005] Alexander, D. C. and Barker, G. J. (2005). Optimal imaging parameters for fiber-orientation estimation in diffusion mri. *NeuroImage*, 27(2):357–367.

[Alzheimer's Disease Neuroimaging Initiative (ADNI),] Alzheimer's Disease Neuroimaging Initiative (ADNI). Alzheimer's disease neuroimaging initiative. http://adni.loni.usc.edu/. Accessed: 2024-08-26.

[Andersson et al., 2007] Andersson, J. L., Jenkinson, M., Smith, S., et al. (2007). Nonlinear registration, aka spatial normalisation fmrib technical report tr07ja2. *FMRIB Analysis Group of the University of Oxford*, 2(1):1–22.

[Assaf and Basser, 2005] Assaf, Y. and Basser, P. J. (2005). Composite hindered and restricted model of diffusion (charmed) mr imaging of the human brain. *Neuroimage*, 27(1):48–58.

[Assaf et al., 2008] Assaf, Y., Blumenfeld-Katzir, T., Yovel, Y., and Basser, P. J. (2008). Axcaliber: a method for measuring axon diameter distribution from diffusion mri. *Magnetic Resonance in Medicine: An Official Journal of the International Society for Magnetic Resonance in Medicine*, 59(6):1347–1354.

[Association, 2020] Association, A. (2020). 2020 alzheimer's disease facts and figures. *Alzheimer's & Dementia*, 16(3):391–460.

[Basser et al., 1994] Basser, P. J., Mattiello, J., and LeBihan, D. (1994). Mr diffusion tensor spectroscopy and imaging. *Biophysical Journal*, 66(1):259–267.

[Behrens et al., 2003] Behrens, T. E., Woolrich, M. W., Jenkinson, M., Johansen-Berg, H., Nunes, R. G., Clare, S., Matthews, P. M., Brady, J. M., and Smith, S. M. (2003). Characterization and propagation of uncertainty in diffusion-weighted mr imaging. *Magnetic Resonance in Medicine: An Official Journal of the International Society for Magnetic Resonance in Medicine*, 50(5):1077–1088.

[Bingham, 1974] Bingham, C. (1974). An antipodally symmetric distribution on the sphere. *The Annals of Statistics*, pages 1201–1225.

[Bürgel et al., 2006] Bürgel, U., Amunts, K., Hoemke, L., Mohlberg, H., Gilsbach, J. M., and Zilles, K. (2006). White matter fiber tracts of the human brain: three-dimensional mapping at microscopic resolution, topography and intersubject variability. *Neuroimage*, 29(4):1092–1105.

[Carr and Purcell, 1954] Carr, H. Y. and Purcell, E. M. (1954). Effects of diffusion on free precession in nuclear magnetic resonance experiments. *Physical review*, 94(3):630.

[Colgan et al., 2016] Colgan, N., Siow, B., O'Callaghan, J. M., Harrison, I. F., Wells, J. A., Holmes, H. E., and Johnson, M. R. (2016). Application of neurite orientation dispersion and density imaging (noddi) to a tau pathology model of alzheimer's disease. *NeuroImage*, 125:739–744.

[Cox et al., 2016] Cox, S. R., Ritchie, S. J., Tucker-Drob, E. M., Liewald, D. C., Hagenaars, S. P., Davies, G., and Deary, I. J. (2016). Ageing and brain white matter structure in 3,513 uk biobank participants. *Nature Communications*, 7:13629.

[Descoteaux, 1999] Descoteaux, M. (1999). High angular resolution diffusion imaging (hardi). *Wiley encyclopedia of electrical and electronics engineering*, pages 1–25.

[Einstein, 1905] Einstein, A. (1905). Über die von der molekularkinetischen theorie der wärme geforderte bewegung von in ruhenden flüssigkeiten suspendierten teilchen. *Annalen der physik*, 4.

[Fick, 1855] Fick, A. (1855). V. on liquid diffusion. *The London, Edinburgh, and Dublin Philosophical Magazine and Journal of Science*, 10(63):30–39.

[Fick et al., 2019a] Fick, R., Deriche, R., and Wassermann, D. (2019a). The Dmipy Toolbox: Diffusion MRI Multi-Compartment Modeling and Microstructure Recovery Made Easy.

[Fick et al., 2019b] Fick, R. H., Wassermann, D., and Deriche, R. (2019b). The dmipy toolbox: Diffusion mri multi-compartment modeling and microstructure recovery made easy. *Frontiers in neuroinformatics*, 13:64.

[Garyfallidis et al., 2014] Garyfallidis, E., Brett, M., Amirbekian, B., Rokem, A., Van Der Walt, S., Descoteaux, M., Nimmo-Smith, I., and Contributors, D. (2014). Dipy, a library for the analysis of diffusion mri data. *Frontiers in neuroinformatics*, 8:8.

[Gunter et al., 2017] Gunter, J., Thostenson, K., Borowski, B., Reid, R., Arani, A., Bernstein, M., Fox, N., Thomas, D., Decarli, C., Tosun, D., et al. (2017). Adni-3 mri protocol. *Alzheimer's Dementia*, 13(7):P104–P105.

[Hahn, 1950] Hahn, E. L. (1950). Spin echoes. *Physical review*, 80(4):580.

[Hyman et al., 2012] Hyman, B. T., Phelps, C. H., Beach, T. G., Bigio, E. H., Cairns, N. J., Carrillo, M. C., Dickson, D. W., Duyckaerts, C., Frosch, M. P., Masliah, E., et al. (2012). National institute on aging–alzheimer's association guidelines for the neuropathologic assessment of alzheimer's disease. *Alzheimer's & dementia*, 8(1):1–13.

[Jelescu and Budde, 2017] Jelescu, I. O. and Budde, M. D. (2017). Design and validation of diffusion mri models of white matter. *Frontiers in physics*, 5:61.

[Jenkinson et al., 2002] Jenkinson, M., Bannister, P., Brady, M., and Smith, S. (2002). Improved optimization for the robust and accurate linear registration and motion correction of brain images. *Neuroimage*, 17(2):825–841.

[Jenkinson and Smith, 2001] Jenkinson, M. and Smith, S. (2001). A global optimisation method for robust affine registration of brain images. *Medical image analysis*, 5(2):143–156.

[Jespersen and Kroenke, 2020] Jespersen, S. N. and Kroenke, C. D. (2020). Modeling the diffusion-time dependence of anisotropic diffusion in fixed brain tissue. *Magnetic Resonance in Medicine*, 83(3):1134–1144.

[Johansen-Berg and Behrens, 2013] Johansen-Berg, H. and Behrens, T. E. (2013). *Diffusion MRI: from quantitative measurement to in vivo neuroanatomy*. Academic Press.

[Jones et al., 2013] Jones, D. K., Knösche, T. R., and Turner, R. (2013). White matter integrity, fiber count, and other fallacies: the do's and don'ts of diffusion mri. *NeuroImage*, 73:239–254.

[Kaden et al., 2007] Kaden, E., Knösche, T. R., and Anwander, A. (2007). Parametric spherical deconvolution: inferring anatomical connectivity using diffusion mr imaging. *NeuroImage*, 37(2):474–488.

[Kamiya et al., 2020] Kamiya, K., Hori, M., and Aoki, S. (2020). Noddi in clinical research. *Journal of Neuroscience Methods*, 346:108908.

[Kang et al., 2015] Kang, J.-H., Korecka, M., Figurski, M. J., Toledo, J. B., Blennow, K., Zetterberg, H., Waligorska, T., Brylska, M., Fields, L., Shah, N., et al. (2015). The alzheimer's disease neuroimaging initiative 2 biomarker core: a review of progress and plans. *Alzheimer's & Dementia*, 11(7):772–791.

[Kraguljac et al., 2022] Kraguljac, N. V., Guerreri, M., Strickland, M. J., and Zhang, H. (2022). Neurite orientation dispersion and density imaging in psychiatric disorders: A systematic literature review and a technical note. *Biological Psychiatry: Global Open Science*.

[Le Bihan and Johansen-Berg, 2012] Le Bihan, D. and Johansen-Berg, H. (2012). Diffusion mri at 25: Exploring brain tissue structure and function. *NeuroImage*, 61(2):324–341. NEUROIMAGING: THEN, NOW AND THE FUTURE.

[Mitchell, 2009] Mitchell, A. J. (2009). A meta-analysis of the accuracy of the mini-mental state examination in the detection of dementia and mild cognitive impairment. *Journal of psychiatric research*, 43(4):411–431.

[Mori and Zhang, 2006] Mori, S. and Zhang, J. (2006). Principles of diffusion tensor imaging and its applications to basic neuroscience research. *Neuron*, 51(5):527–539.

[Moseley et al., 1990] Moseley, M. E., Cohen, Y., Mintorovitch, J., Chileuitt, L., Shimizu, H., Kucharczyk, J., Wendland, M., and Weinstein, P. (1990). Early detection of regional cerebral ischemia in cats: comparison of diffusion-and t2-weighted mri and spectroscopy. *Magnetic resonance in medicine*, 14(2):330–346.

[Nasreddine et al., 2005] Nasreddine, Z. S., Phillips, N. A., Bédirian, V., Charbonneau, S., Whitehead, V., Collin, I., Cummings, J. L., and Chertkow, H. (2005). The montreal cognitive assessment, moca: a brief screening tool for mild cognitive impairment. *Journal of the American Geriatrics Society*, 53(4):695–699.

[Novikov et al., 2018] Novikov, D. S., Kiselev, V. G., and Jespersen, S. N. (2018). On modeling. *Magnetic Resonance in Medicine*, 79(6):3172–3193.

[Pierpaoli et al., 1996] Pierpaoli, C., Jezzard, P., Basser, P. J., Barnett, A., and Di Chiro, G. (1996). Diffusion tensor mr imaging of the human brain. *Radiology*, 201(3):637–648.

[Prince et al., 2015] Prince, M., Wimo, A., Guerchet, M., Ali, G.-C., Wu, Y.-T., and Prina, M. (2015). *World Alzheimer Report 2015: The Global Impact of Dementia*. Alzheimer's Disease International.

[Sexton et al., 2011] Sexton, C. E., Kalu, U. G., Filippini, N., Mackay, C. E., and Ebmeier, K. P. (2011). A meta-analysis of diffusion tensor imaging in mild cognitive impairment and alzheimer's disease. *Neurobiology of aging*, 32(12):2322–e5.

[Smith et al., 2004] Smith, S. M., Jenkinson, M., Woolrich, M. W., Beckmann, C. F., Behrens, T. E., Johansen-Berg, H., Bannister, P. R., De Luca, M., Drobnjak, I., Flitney, D. E., et al. (2004). Advances in functional and structural mr image analysis and implementation as fsl. *Neuroimage*, 23:S208–S219.

[Sotiropoulos et al., 2012] Sotiropoulos, S. N., Behrens, T. E., and Jbabdi, S. (2012). Ball and rackets: inferring fiber fanning from diffusion-weighted mri. *Neuroimage*, 60(2):1412–1425.

[Sperling et al., 2011] Sperling, R. A., Aisen, P. S., Beckett, L. A., Bennett, D. A., Craft, S., Fagan, A. M., Iwatsubo, T., Jack Jr, C. R., Kaye, J., Montine, T. J., et al. (2011). Toward defining the preclinical stages of alzheimer's disease: Recommendations from the national institute on aging-alzheimer's association workgroups on diagnostic guidelines for alzheimer's disease. *Alzheimer's & dementia*, 7(3):280–292.

[Stanisz et al., 1997] Stanisz, G. J., Wright, G. A., Henkelman, R. M., and Szafer, A. (1997). An analytical model of restricted diffusion in bovine optic nerve. *Magnetic Resonance in Medicine*, 37(1):103–111.

[Stejskal and Tanner, 1965] Stejskal, E. O. and Tanner, J. E. (1965). Spin diffusion measurements: spin echoes in the presence of a time-dependent field gradient. *The journal of chemical physics*, 42(1):288–292.

[Tariq et al., 2016] Tariq, M., Schneider, T., Alexander, D. C., Gandini Wheeler-Kingshott, C. A., and Zhang, H. (2016). Bingham–noddi: Mapping anisotropic orientation dispersion of neurites using diffusion mri. *NeuroImage*, 133:207–223.

[Tariq et al., 2014] Tariq, M., Schneider, T., Alexander, D. C., Wheeler-Kingshott, C. A., and Zhang, H. (2014). In vivo estimation of dispersion anisotropy of neurites using diffusion mri. In *Medical Image Computing and Computer-Assisted Intervention–MICCAI 2014: 17th International Conference, Boston, MA, USA, September 14-18, 2014, Proceedings, Part III 17*, pages 241–248. Springer.

[Tournier et al., 2012] Tournier, J.-D., Calamante, F., and Connelly, A. (2012). Mrtrix: diffusion tractography in crossing fiber regions. *International journal of imaging systems and technology*, 22(1):53–66.

[Wang et al., 2011] Wang, Y., Wang, Q., Haldar, J. P., Yeh, F.-C., Xie, M., Sun, P., and Zee, D. S. (2011). Quantification of increased cellularity during inflammatory demyelination. *Brain*, 134(12):3590–3601.

[Weiner et al., 2017] Weiner, M. W., Veitch, D. P., Aisen, P. S., Beckett, L. A., Cairns, N. J., Green, R. C., Harvey, D., Jack Jr, C. R., Jagust, W., Morris, J. C., et al. (2017). The alzheimer's disease neuroimaging initiative 3: Continued innovation for clinical trial improvement. *Alzheimer's & Dementia*, 13(5):561–571.

[Winston, 2012] Winston, G. P. (2012). The physical and biological basis of quantitative parameters derived from diffusion mri. *Quantitative imaging in medicine and surgery*, 2(4):254–265.

[Zhang et al., 2011] Zhang, H., Hubbard, P. L., Parker, G. J., and Alexander, D. C. (2011). Axon diameter mapping in the presence of orientation dispersion with diffusion mri. *Neuroimage*, 56(3):1301–1315.

[Zhang et al., 2012] Zhang, H., Schneider, T., Wheeler-Kingshott, C. A., and Alexander, D. C. (2012). Noddi: practical in vivo neurite orientation dispersion and density imaging of the human brain. *Neuroimage*, 61(4):1000–1016.